Layer-Structured Zintl Phases as Novel Thermoelectric Materials

---

A Dissertation Presented to

the Faculty of the Department of Physics and T_CSUH

University of Houston

In Partial Fulfillment

of the Requirements for the Degree

Doctor of Philosophy

By

Jing Shuai

December 2016

Layer-Structured Zintl Phases as Novel Thermoelectric Materials

---

Jing Shuai

Prof. Zhifeng Ren

Department of Physics and T_CSUH

Prof. Ching-Wu Chu

Department of Physics and T_CSUH

Prof. Shuo Chen

Department of Physics

Prof. Dong Cai

Department of Physics

Prof. Jiming Bao

Department of Electrical and Computer Engineering

Dean, College of Natural Sciences and Mathematics

Acknowledgement

I would like to acknowledge the support and encouragement I received during my doctoral research. I am incredibly grateful for those of you who stood by to support me along the way. My deepest gratitude goes first to Professor Zhifeng Ren, who expertly guided me through my graduate education and even helped me explore the way of the future. His wisdom, knowledge and commitment to the highest standards motivated me, and his personal traits influenced me. I also heartily thank all the committee: Zhifeng Ren, Ching-Wu Chu, Shuo Chen, Dong Cai, and Jiming Bao. I appreciate the support during my dissertation research and general advice provided in my APE and the final defense. Their guidance, questions and comments from different perspectives motivated me for constant learning and continual improvement.

I wish to express my profound appreciation to my colleagues. Thank you all for the fantastic team I have been fortunate to work with over the years. Jiehe Sui was responsible for leading me to the path of my main research. Qian Zhang, Huaizhou Zhao, Weishu Liu, Yucheng Lan, Qing Jie and Hui Wang enlightened me in thermoelectrics. I would also like to thank Hee Seok Kim, Jun Mao, Zihang Liu, Shaowei Song, Hangtian Zhu and Hao Zhang for any kind discussion and cooperation. The calculation parts were contributed by Huiyuan Geng, Gang Chen, Jiawei Zhou, Jifeng Sun and David Singh. Here, I owe my great thanks to their generous assistance. Last but not least, I should not forget to thank my family. Their understanding potentially encouraged me to focus on what I am interested and to pursuit my passion in life.

Layer-Structured Zintl Phases as Novel Thermoelectric Materials

An Abstract of Dissertation

Presented to

the Faculty of the Department of Physics and T_CSUH

University of Houston

In Partial Fulfillment

of the Requirements for the Degree

Doctor of Philosophy

By

Jing Shuai

December 2016

Abstract

Thermoelectric materials have been fascinated extensive interest in the last two decades due to the potential applications in waste-heat recovery from industrial processes, automobiles, and renewable energy sources. In pursuit of potential thermoelectric candidates, Zintl phases have recently gained interest because of their characteristics desired for use in thermoelectric devices for power generation: complex structures, extensive opportunities to tune transport properties, narrow band gaps, and thermal and chemical stability.

In this huge pool of Zintl compounds, the two-dimensional layered $CaAl_2Si_2$-typed Zintls, especially antimony-based Zintl compounds, have been demonstrated to be promising TE materials for middle- to high-temperature applications. Here, we report the rarely studied bismuth-based Zintl phases $(Ca,Yb,Eu)Mg_2Bi_2$ with competitive thermoelectric performance. This thesis first describes the thermoelectric characterization and optimization of these phases, including eliminating the Bi impurity, Na substitution to boost power factor, as well as as understanding the band engineering and strain field fluctuation in solid solutions. In addition, since the fabrication method for synthesizing the Zintl compounds here is different from the most reported melting method, the comparison between these two methods based on the classical Sb-based $Ca_{1-x}Yb_xZn_2Sb_2$ compounds will be included, which allows us to further understand the defect-controlled p-type Zintl phases.

For application, thermoelectric generators should consist of both n- and p- type legs with equivalent performance. However, through several decades' efforts, it still remains very difficult to make competitive n-type Zintl materials until the discovery of n-type $Mg_{3+x}Sb_2$-based Zintl phase. Given the reported low electrical conductivity and low average *ZT*, it motivates us to further improve it through Nb partial substitution, resulting in enhanced average *ZT* value to about 1 across the entire measured temperature. Moreover, doping with the ideal hole dopants (Na^+) on its corresponding p-type Mg_3Sb_2 Zintls has also been investigated, allowing for effectively increasing the carrier concentration and optimization of the thermoelectric performance. Besides the Zintl phases, the final part introduces another excellent p-type thermoelectric materials MgAgSb with potential power-generation application near room temperature. The works highlight the discovery of complex bulk thermoelectric materials with intrinsically low lattice thermal conductivity, which would stimulate many of the recent advances in thermoelectrics.

Contents

List of Figures

List of Tables

Chapter 1

Introduction

The emerging global demand for energy production, conservation, and management has boosted interest in more-effective means of power generation. Considering the limited main source provided by burning fossil fuels (*e.g.*, gasoline, coal, natural gas), along with the environmental problem (*e.g.*, pollution, global-warming gases), enhancements to the existing energy supply must be considered to ensure the sustainable development. Renewable sources, including wind, hydropower, biomass, and others, have been taken into consideration and utilized. Another potential source of power is electricity from heat sources, which come from the burning of fossil fuels, from sunlight, or as a byproduct of various processes (*e.g.*, combustion, chemical reactions, nuclear decay).

Therefore, as one of the alternative green approaches for such electrical power generation, the thermoelectric effect has been discussed extensively and the study of thermoelectric materials has been accelerated currently [1-5]. Unlike the heat in conventional generators supported by burning a fuel or through radioactive decay, the thermoelectrics are environmental friendly by making use of renewable heat sources list above [2,4]. Also unlike the typical approach that uses different types of engines, thermoelectric generators have a distinct advantage by operating without moving parts as the charge carriers are directly driven by the flow of heat through the thermoelectric devices [1,6].

We've known about the thermoelectric effect for several hundred years but it wasn't until the 1960s, when semiconductor materials emerged, that meaningful thermoelectric devices could be manufactured [7]. During that time at height of Cold War and the Space Race, NASA was also engaged in exploring the TE application and designed its first radioisotope thermoelectric generator (RTG) powered spacecraft, the Transit 4A [8]. Since then, continued progress was made in power generation for deep-space probes or remote sensors, and thermal management of high power electronics [8]. Recent decades even have witnessed extended applications in other fields, such as thermic watch introduced by Seiko, thermoelectric seat coolers in Lincoln Navigator and Toyota's Lexus, E1(the first-ever thermoelectric generator for industrial waste-heat recovery), *etc.* It is hoped and expected that the TE material will play a more increasing role than it has in the past.

A hot and critical issue for discussion now is how the role for TE material is likely to be and the answer to this question depends solely on how to develop better performing thermoelectric materials and how efficient these materials are. To address those issues, in the first chapter, I will start with the background and fundamentals of thermoelectrics, following by the approaches to boost the TE performance, as well as my research direction.

1.1 Thermoelectric Effects

The thermoelectric effect refers to the phenomenon of the direct conversion of temperature differences to electric voltage and vice versa. There are three well-known major effects involved in the thermoelectric phenomenon: the Seebeck effect, the Peltier effect, and the Thomson effect. Historically the first TE effect, now known as the Seebeck effect, was observed by Thomas Johann Seebeck [9]. In the following three decades, the TE field developed extensively with more insights into the fundamentals, as well as the discovery of many new phenomena, such as the Peltier effect [10] and the Thomson effect [11].

In 1821, Seebeck discovered that an electric field appears when two dissimilar materials are connected together and their junctions are exposed to temperature gradient, known a the Seebeck effect [9](Fig. 1.1). It is later understood although the Seebeck effect is more obvious at a junction, the voltage could be induced in any individual bulk material in a temperature gradient, illustrated in the bottom of Fig. 1.1. In this open circuit, the Seebeck coefficient could be expressed as, S

$$S = -\frac{\Delta V}{\Delta T} \tag{1.1}$$

where ΔV is voltage drop along the same direction of the temperature drop, ΔT is the temperature gradient, and S is so-called Seebeck coefficient. For semiconductors, when the charge carriers are electrons, the counteracting electric field will be against temperature gradient, resulting in a negative Seebeck coefficient (n-type). If dominate carrier type is hole, the sign of S would be positive (p-type).

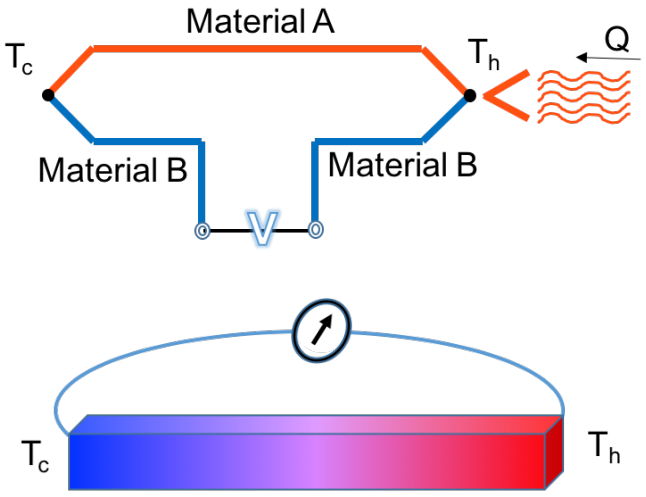

Figure 1.1 Schematic diagram of the Seebeck effect across the two dissimilar materials (top), and a single material (bottom).

The Peltier effect is the reverse of the Seebeck effect, discovered by a French physicist Jean Charles Athanase Peltier in 1834 [10]. It refers to the temperature difference introduced by voltage gradient. When an external current passes through two dissimilar materials, one junction is heated and the other is cooled, which depends on the direction of current (Fig. 1.2). The Peltier coefficient Π_{ab} of a pair of materials at a junction is defined as the ratio of heat current q to the applied current density j

$$\Pi_{ab} = \frac{q}{j} = \Pi_a - \Pi_b \tag{1.2}$$

where Π_a and Π_b are the Peltier coefficients of each material. As can be seen in this formula, the Peltier coefficients represent how much heat is carried per unit charge. Since charge current must continuous across a junction, the associated heat flow will develop a

discontinuity if Π_a and Π_b are dissimilar. However, the total heat generated is not determined by the Peltier effect alone, as it may also be influenced by Joule heating and thermal gradient effects.

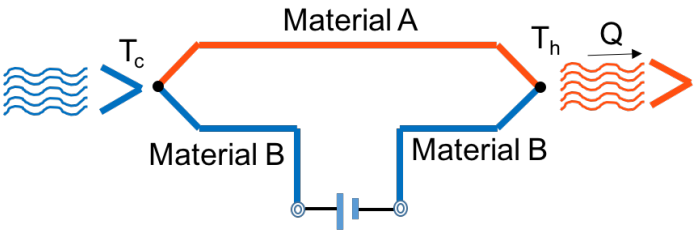

Figure 1.2 Schematic representation of the Peltier effect.

The last of the thermoelectric effects, the Thomson effect [11], describes the evolution or absorption of heat when electric current passes through a circuit composed of a single material that has a temperature difference along its length. If a current density j passes through a homogenous conductor, the rate of heat generation or absorption can be given as

$$\frac{dq}{dx} = \tau j \frac{dT}{dx} \tag{1.3}$$

Where τ is the Thomoson coefficient, dq/dx is the rate of heating or cooling per unit length, *and* dT/dx is the temperature gradient.

1.2 Thermoelectric Devices

Based on the thermoelectric effects described above, one can build a thermoelectric module for power generation (the Seebeck effect), or cooling system (the Peltier effect).

The construction of a simplest thermoelectric module is shown schematically in Fig. 1.3. Here, one thermocouple is made of a pair of n-type and p-type thermoelectric legs. For application, a large number of thermocouples should be assembled electrically in series and thermally in parallel to form a real module, as shown at right in Fig. 1.3. The general construction is very similar for both power generator and cooling applications. Ideally, the generator prefers long and thin thermoelectric legs, while short and fat legs is better for cooling system.

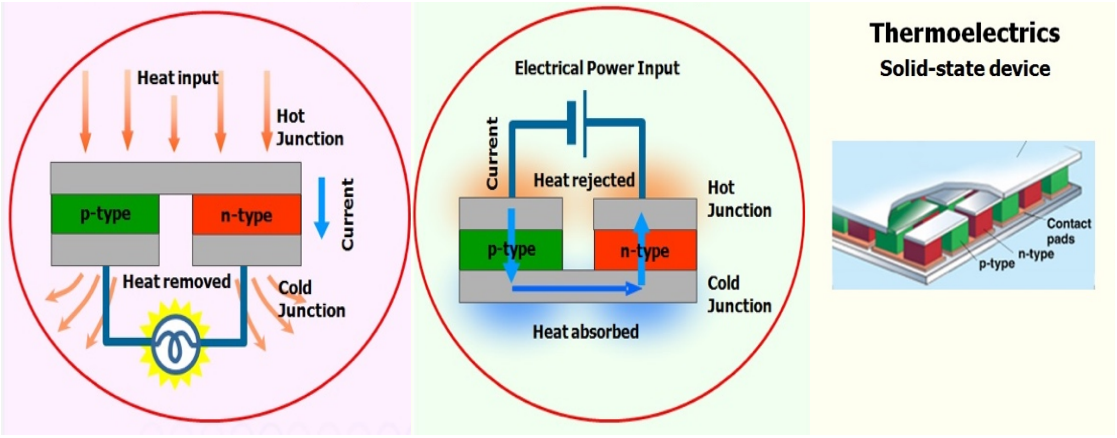

Figure 1.3 (Left) The Seebeck effect uses the temperature difference between to objects to generate an electric current. (Centre) The Peltier effect is used to cool hot objects using an electrical current. (Right) Thermoelectric devices are made up of pairs of P- and N-type material.

For a simplest generator consisting of a single thermocouple with thermoelements fabricated from n- and p-type semiconductors between hot side temperature T_h and cold side temperature T_c, assuming the converter operating as an ideal generator, the efficiency of a generation η is defined as the ratio of the electrical power delivered to the load to the heat absorbed at the hot junction. After derivation, one comes to the final expression of conversion efficiency:

$$\eta = \frac{T_h - T_c}{T_h}\left(\frac{\sqrt{1 + (ZT)_{ave}} - 1}{\sqrt{1 + (ZT)_{ave}} + T_c/T_h}\right) \tag{1.4}$$

The conversion efficiency is quantified by the average dimensionless figure of merit $(ZT)_{ave} = (S^2\sigma/\kappa)T$, S, σ, and κ are the Seebeck coefficient, electrical conductivity, and the thermal conductivity, respectively [6]. In the thermoelectric field, the dimensionless figure of merit ZT is the most used quantity to describe the performance of a TE material. Higher ZT corresponds to higher conversion efficiency. The power factor, defined as $S^2\sigma$, is also often used for describing the performance of a thermoelectric materials and governs the maximum output power density.

The energy generator of a refrigerator is measured by its coefficient of performance (COP) [8], given by the cooling power produced divided by the rate at which electrical energy is supplied. The optimized efficiency can be written as

$$\Phi = \frac{T_c}{T_h - T_c}\left(\frac{\sqrt{1 + (ZT)_{ave}} - T_h/T_c}{\sqrt{1 + (ZT)_{ave}} + 1}\right) \tag{1.5}$$

Similar as the efficiency for generator, COP also depends on the average ZT.

1.3 Thermoelectric Parameters

A good thermoelectric material requires high ZT, which is the equal of requiring a high Seebeck coefficient, a high electrical conductivity, and a low thermal conductivity. However, it is not easy to control each of these parameters separately because all of these

transport parameters are inter-related to each other. In the following section, the thermoelectric transport parameters are discussed, as well as their inter-relationships.

1.3.1 Electrical Conductivity

Based on Boltzmann's equation, as well as several approximations like (1) assuming constant relaxation time τ , (2) $\varepsilon - \varepsilon_F \gg k_B T$, and (3) considering isotropic and parabolic band with $\varepsilon = \frac{h^2 k^2}{2m}$, the electrical conductivity σ, carrier concentration n , and the relative relations can be simplified as

$$\sigma = \frac{2e^2\tau}{m^*}\left(\frac{m^* k_B T}{2\pi h^2}\right)^{\frac{3}{2}} \exp\left(-|\varepsilon_F|/k_B T\right) \tag{1.6}$$

$$n = 2\left(\frac{m^* k_B T}{2\pi h^2}\right)^{\frac{3}{2}} \exp\left(-|\varepsilon_F|/k_B T\right) \tag{1.7}$$

$$\sigma = ne\mu \tag{1.8}$$

$$\mu = \frac{e\tau}{m^*} \tag{1.9}$$

here k_B is Boltzmann constant, m^* is the density of state (DOS) effective mass, μ is carrier mobility, and ε_F is the Fermi energy of the system.

It is reasonable that high electrical conductivity reduces energy leakage by joule heating within the materials. So a good TE materials have high electrical conductivity, in other words, it requires high carrier concentration and higher carrier mobility as illustrated above.

1.3.2 Seebeck Coefficient

Following the similar arguments as in electrical conductivity, and considering for metal and heavily doped semiconductors, the Seebeck coefficient can be simplified as following [12]:

$$S = \frac{\pi^3}{3}\frac{{k_B}^2 T}{e}\frac{\partial ln\sigma}{\partial E}\Big|_{\varepsilon=\varepsilon_F} \tag{1.10}$$

Assuming that electron conduction within a single parabolic band (SPB) along with energy-independent scattering approximation [13], the Seebeck coefficient is given by

$$S = \frac{8\pi k_B^2}{3eh^2} m^* T \left(\frac{\pi}{3n}\right)^{\frac{2}{3}} \tag{1.11}$$

Here, h is the Plank constant. Obviously, the greater density of state effective mass and lower carrier concentration will lead to the higher Seebeck coefficient.

1.3.3 Thermal Conductivity

As we illustrated before, low thermal conductivity will increase energy conversion efficiency, because a high thermal conductivity would enhance heat transfer through the sample, thus the temperature difference cannot be sustained. Since both electron and phonon are heat carriers in a solid, thermal conductivity normally consists two parts

$$k = k_e + k_l \tag{1.12}$$

where k_e represents electronic contribution while k_l comes from lattice part of thermal conductivity.

The electronic thermal conductivity is related with the electric conductivity well-described by the *Weidman-Franz Law* [14]

$$k_e = L\sigma T = Lne\mu T \tag{1.13}$$

where L is the Lorenz number, which is 2.4×10^{-8} W Ω K^{-2} for metals. This term is strongly related to the electrical conductivity and high electrical conductivity will contribute to higher thermal conductivity. Some common sources of uncertainty in k_e come from reduced Lorenz factor in low-carrier-concentration materials and mixed conduction by introducing a bipolar term into the thermal conduction.

The lattice thermal conductivity can be treated as the only independent thermoelectric parameter and doesn't conflict directly with other parameters. Thus, decreasing the lattice thermal conductivity has been intensely investigated for enhancing the TE performance. The lattice part of thermal conductivity arising from phonon transport can be approximately written using the classical kinetic theory as following

$$k_l = \frac{C_v v_s l}{3} = \frac{C_v {v_s}^2 \tau}{3} \tag{1.14}$$

where C_v is specific heat at constant volume, v_s is average velocity of sound, and l is phonon mean free path. The phonon relaxation time τ is related to l by v_s.

Therefore, both low v_s and decreasing τ are favorable to achieve low lattice thermal conductivity. Traditionally, low v_s is usually found in dense materials with soft bonds ($v_s = \sqrt{B/d}$, where B is the appropriate elastic modulus and d is the density of the

material), and reduction of τ has relied on intentional introduction of points defects and nanostructures to scatter phonons.

1.3.4 Carrier Concentration and Effective Mass related TE Parameters

As discussed above, improving *ZT* by simultaneously boosting power factor and decreasing thermal conductivity is extraordinarily difficult, because all the parameters (*S*, σ, and κ) in the expression of *ZT* can't be modified without affecting others due to their intrinsic conflictions, such as carrier concentration and effective mass. The conflicting thermoelectric properties via carrier concentration are shown in Fig. 1.4. It illustrates that the balance must be achieved in order to obtain high thermoelectric efficiency: a large Seebeck coefficient is found in low carrier concentration insulators, while high electrical conductivity is observed in high carrier concentration metals. As a result, the best thermoelectric materials are always heavily doped semiconductors with carrier density in the range from 10^{18} to 10^{21} cm^{-3}.

The effective mass of the charge carrier provides another conflict as larger effective masses produce high Seebeck coefficient but low electrical conductivity. Normally, the flat, narrow bands with high density of states at Fermi surface contributes to heavier density of effective mass. The heavier effective mass m^* ($m^* = N_v^{2/3} m_b^*$, m_b^* is band-mass of a single valley) has detrimental effect on lowering carrier mobility, and therefore low electrical conductivity, while low band mass with multiple degenerate valleys is another issue. A

compromise between high effective mass and high mobility must be established to obtain good thermoelectric materials.

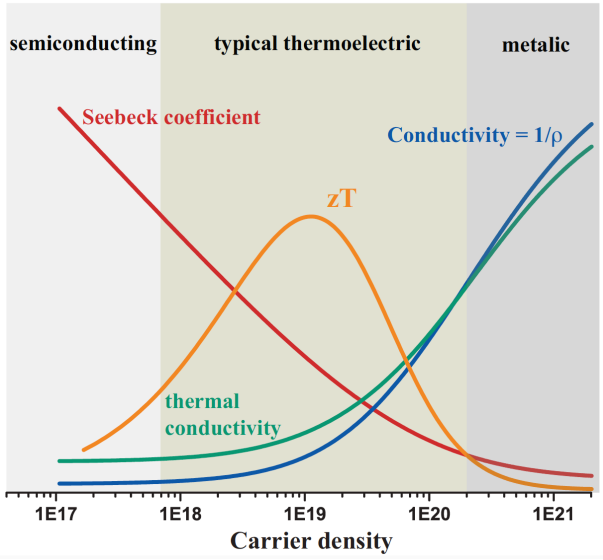

Figure 1.4 Schematic trend of transport properties versus carrier density, *ZT* is usually optimized in the heavily doped semiconductor regime.

1.4 Zintl Phases

Ideal thermoelectrics generally have a few common characteristics. Considering those commons given above, it is not surprising that semiconductors like Bi_2Te_3 [15], PbTe [16-18], SiGe [19-21] were first investigated as a promising thermeoelectric materials. Those materials held the competitive *ZT* for decades for application in low temperature, mid-to-high temperature and high temperature range. With the concept of PGEC (phonon glass electron crystal) suggested by Slack in 1990s, another breakthrough was realized with more thermoelectrics discovered with $ZT > 1$. A common feature of this kind of materials

(*e.g.,* Skutterudites [22,23], clatherates [24], and Zintl phases [25,26]) is that most have lattice thermal conductivities that are lower than the present commercial materials.

Several general strategies to reduce lattice thermal conductivity have been successfully explored, such as creating point defects, rattling structure, or increasing scattering phonons at interfaces [27-29]. It is worth noting that the discovery of complex bulk thermoelectric materials with intrinsically low lattice thermal conductivity has stimulated many of the recent advances in thermoelectrics. For example, the extremely low lattice thermal conductivity is observed in the complex Zintl phases $Yb_{14}MnSb_{11}$ [25], which contains $[MnSb_4]^{9-}$ tetrahedra, polyatomic $[Sb_3]^{7-}$ anions, as well as isolated Sb^{3-} anions and Yb^{2+} cations. Driven by this motivation, the brief introduction for the Zintl phases will be described in the next section.

1.4.1 Zintl Chemistry

German chemist Eduard Zintl [30,31] (1898–1941) discovered a subclass of intermetallic compounds, the properties of which included high melting points, high heats of formation, poor electrical conductivities notwithstanding their metallic luster, and increased brittleness. Those particular intermetallic compounds have been named "Zintl phases" by Laves in 1941 [32], advanced to one of most inventory subjects in materials science during the last century. Ionic and covalent bonds in intermetallic phases were a matter of course for Zintl, a model set forth by Eduard Zintl based on chemical valences for this special intermetallic. NaTl, a textbook example treated as a milestone to understand

Zintl phases, transfers of electrons from the more electropositive Na to polyanionic diamond Tl structure, which possesses four valence electrons and covalently bonding [31]. The guiding principle for rationalizing the number of covalent bonds here can be guided by the 8-N rule (N is the total valence electron count). N simple represents the total number of electrons available to each anion in the structure, including the electrons transferred by the cations. Klemm generalized this powerful idea and developed into a versatile and general concept [33], formulated as $A_aX_x = (A^{n+})a[X^{(an/x)-}]x$, A = active (electropositive) metal from groups 1, 2 and X = noble (electronegative) metal or semimetal from groups 13, 14 and 15. For NaTl, the four Tl-Tl bond can be rationalized by applying the 8-N rule (N = (1*1+1*3)/1) = 4).

As more compounds were discovered, the historical definition of Zintl phases was proved to be too limiting. Schafer *et al*. proposed more general definition where electron transfer is essentially completed and developed the Zintl–Klemm concept into another important valence electron counting scheme that has achieved wide usage among molecular and solid-state disciplines [34,35].

Over the last 25-30 years, the historical definition of Zintl phases has expanded from binary to ternary phases and enlarged to include transition metals and rare earth elements in some cases [35,36]. Numerous such compounds have already been synthesized and characterized, featuring new structure types and unusual bonding patterns , along with a rich variety of interesting physical properties such as nonlinear optical properties [37], superconductivity [38], colossal magnetoresistance [39] and especially thermoelectricity

[40] in recent year. Herein we will focus on the thermoelectric properties of the recent progress on Zintl phases.

1.4.2 Thermoelectric Zintl Phases

Inherent in the Zintl–Klemm formalism is a coexisting tension between anisotropic, covalent bonding interactions, and isotropic, ionic, or metallic bonding forces collected in a system, which leads to many unique, complex crystal structures. The rich chemistry of Zintl compounds attributes to many of the characteristics desired for thermoelectric applications: complex structures, extensive opportunities to tune transport properties, narrow band gaps, and thermal and chemical stability. However, Zintl compounds were not recognized as potential thermoelectric materials until high *ZT* found in $Yb_{1-x}Ca_xZn_2Sb_2$ in 2005 [41]. The past ten years has witnessed a remarkable investigation regarding the Zintl phases as thermoelectrics. Notable examples of thermoelectric intermetallic Zintl materials include clathrates [24], filled skutterudites [42,43], other typical Zintl families (*e.g.*, $Yb_{14}MnSb_{11}$) *et al*. Owing to the unique chemistry and excellent TE performance for chathrate compounds, they already comprised their own field. In addition, for skutterudite compounds, although they meet the Zintl criteria to some degree, researchers also separated them as another field for study. For other typical Zintls as thermoelectics, they include Mg_3Sb_2 [44], $EuMg_2Bi_2$ [45], Ca_3AlSb_3 [46], $Ca_5Al_2Sb_6$ [47], $Yb_9Mn_{4.2}Sb_9$ [48], $Eu_{11}Cd_6Sb_{12}$ [49], *etc.* Besides, several recently discovered Zintl phases, such as $Ba_2Cd_2Sb_3$ [50], $Ca_{10}LaCdSb_9$ [51], Eu_2ZnBi_2 [52], $Sm_2Mn_3Sb_6$ [53], $Ca_{21}Mn_4Sb_{18}$ [54], etc., could have potential transport properties but have not yet fully studied. Here, from the views of

covalently bonded "substructures" in Zintl compounds, we will show three typical Zintl thermoelectrics with competitive *ZT* values for interested readers to have a sense of structure-dependent properties.

1.4.2.1 Zero-dimensional 14-1-11 Zintls

One of the best p-type thermoelectric materials at high temperature is 0-dimensional covalent structure of $Yb_{14}MnSb_{11}$, with *ZT* ~1 at 1200 K [55] reported in the year of 2006. The general formula can be represented as $A_{14}MPn_{11}$, where A is a heavier alkaline earth or 2+ rare earth element (Ca, Sr, Ba, Eu, and Yb), M is main group element or transition metal (Al, Mn, Zn, Ga, Nb, In, and Cd), and Pn comes from group 15 (P, As, Sb, and Bi). However, not all the combinations of the elements mentioned above have been tested, especially in terms of transport properties. The unit cell of $A_{14}MPn_{11}$ contains 208 atoms and is built up from isolated covalently bonded anions of $[MPn_4]^{9-}$ tetrahedra, and $[Pn_3]^{7-}$ linear units, along with Pn^{3-} anions, and A^{2+} cations. Remarkable investigations have been done regarding the enhancement of the thermoelectric performance based on $Yb_{14}MnSb_{11}$, and this material is even under development by the Jet Propulsion Laboratory (JPL) for their next generation radioisotope thermoelectric generator [56]. The current record for the optimized $Yb_{14}MnSb_{11}$ was observed in $Yb_{14}Mn_{1-x}Al_xSb_{11}$ (x=0.6 and 0.8) with *ZT* = 1.3 at ~1223 K. Considering the flexibility of this structure and promise of more compounds, especially inspired by the recent reported higher TE performance in $Yb_{14}MgSb_{11}$ [57], it is anticipated that there are still possibilities to find more new 14-1-11 analogs for even higher *ZT*s.

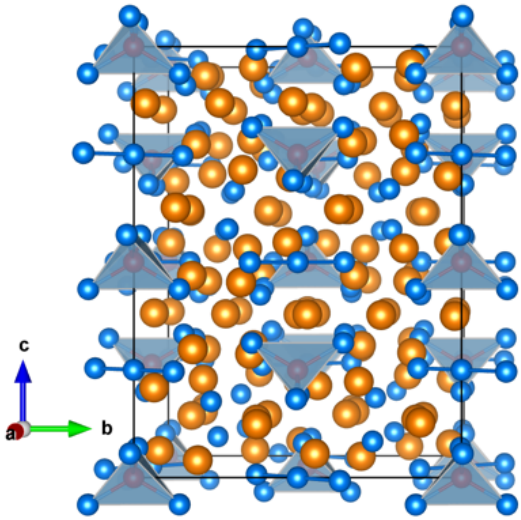

Figure 1.5 Structure of 0-dimensional $Yb_{14}MnSb_{11}$ Zintl phase.

1.4.2.2 One-dimensional 3-1-3 Zintls

A well know one-dimensional chain-forming Zintl phase with promising thermoelectric properties is compound with A_3MPn_3 stoichiometry (A= Ca, Sr, Ba; M= Al, Ga, In; Pn = P, As, Sb). Three distinct types of the structures have been discovered by Cordier *et al.* at 1980s [58-61]. Two types have shown the typical one-dimensional characteristics with higher TE performances. The first type is simple chains of corner-linked MPn_4 tetrahedra surrounded by cations, formed by the small cation (*e.g.,* Ca_3AlSb_3, Ca_3AlAs_3) or small pnictogen species (*e.g.,* Sr_3InP_3) [61], as shown in Fig. 1.6. The other one is the monoclinic structure of Sr_3GaSb_3, containing infinite, closely packed, but non-linear chains of corner sharing tetrahedral units (Fig. 1.6). The current record *ZT* value is observed in Zn-doped Sr_3GaSb_3 with *ZT* ~0.94 at 1000 K [62]. Compared with zero-

dimensional 14-1-11 family, one-dimensional tetrahedral chains structure type (*e.g.*, Ca_3AlSb_3) stands out as having better electronic transport performance and relatively lower m^* (< 1 m_e) and higher electronic mobility.

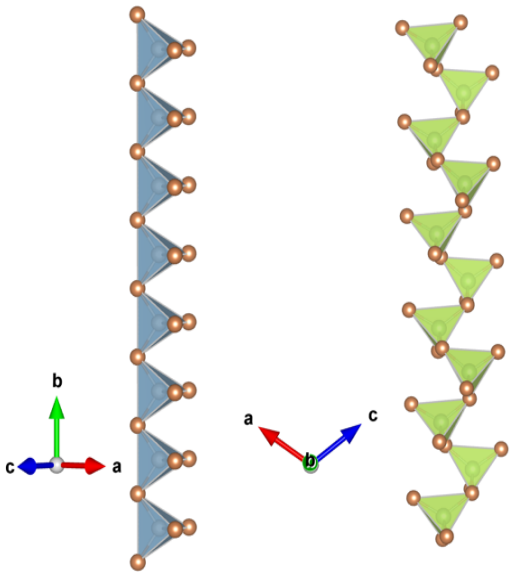

Figure 1.6 The distinct chain-like polyanions formed by the 1-dimensional Zintl antimonides Ca_3AlSb_3 (left) and Sr_3GaSb_3 (right).

1.4.2.3 Two-dimensional 1-2-2 Zintls

Two-dimensional covalent planed $CaAl_2Si_2$-type Zintl phase has accelerated tremendous explorations recently due to its excellent thermoelectric performance. More than 30 years ago, this structure has been fully understood by formulating in AB_2X_2 stoichiometry [63,64]. The A-site contains alkaline-earth or divalent rare earth element such as Ca, Ba, Sr, Yb, and Eu, B is a d^0, d^5, d^{10} transition metal (Mn, Zn, and Cd) or a main-group element like Mg, while X comes from Group 14 and 15 such as Sb and Bi.

Following Zintl-Kelmm concept, B and X form anionic sheets with covalent bonding due to the similar electronegativity, while A^{2+} cations donate electrons to the $(B_2X_2)^{2-}$ framework. The structure is often depicted as in Fig. 1.7, clearly showing the bonding within the B-X layers between planes of A^{2+}. Thermoelectric candidates $Ca_{1-x}Yb_xZn_2Sb_2$ was first synthesized by Gascoin et al. in 2005 and investigated to have a promising *ZT* values ~0.56 [41]. Inspired by this work, lots of other $CaAl_2Si_2$-type Zintl phases have been studied within past decade. Among those compounds, Zintl antimonides solutions $YbCd_{1.6}Zn_{0.4}Sb_2$ and $EuZn_{1.8}Cd_{0.2}Sb_2$ are reported to have the *ZT* above unity [26,65].

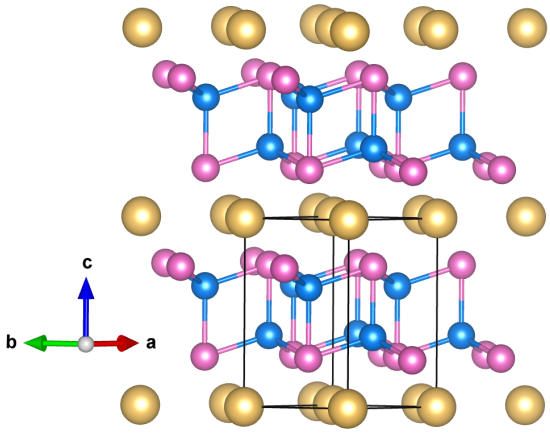

Figure 1.7 The crystal structure of 2-dimensional $CaZn_2Sb_2$ Zintl phase

1.4.2.4 Structure-dependent TE Properties

As different Zintl families described above, the dimensionality and orientation of the polyanionic structures appear to influence both electronic transport properties and thermal transport properties. To elaborate it, the thermoelectric properties of the well-characterized 0,1,2-dimensional representative Zintl phases, along with their density of

states effective mass and carrier mobility, are given in Table 1.1. It is obvious that the thermal conductivities for all those Zintl compounds are very low. The lowest value is obtained in zero-dimensional compound of $Yb_{14}MnSb_{11}$, which contains large number of atoms per unit cell.

In the table, one can also observe that the density of states effective mass presents a fluctuant reduction from 0 dimension to 2 dimension. This also explains the mobility trend with increased dimensionality to a certain extent. Here, one may conclude that perhaps not true in all cases, the nature of the covalently bonded substructure, especially ordered anionic units like 1-2-2 structure, is thought to play a major role in impacting the carrier mobility and influencing the electronic transport properties. Therefore, upon carrier concentration optimization, the relatively higher power factor is expected in 1-2-2 structure, more than three times higher than that in 0- and 1-dimensional Zintl compounds.

Table 1.1 Experimental properties of 0- to 2-dimensional Zintl phases. m^* is the effective mass, μ is the hall mobility at room temperature. N is the number of atoms per unit cell.

	m^*	μ	ZT	T	PF	κ_L	N
	m_e	$cm^2V^{-1}S^{-1}$		K	$\mu W\ cm^{-1}\ K^{-2}$	$W\ m^{-1}\ K^{-1}$	
$Yb_{14}Mn_{0.4}Al_{0.6}Sb_{11}$	3	4	1.3	1223	7	0.25	208[66]
$Sr_3Ga_{0.93}Zn_{0.07}Sb_3$	0.9	17	0.9	1000	5.5	0.42	56 [62]
$Ca_{2.97}Na_{0.03}AlSb_3$	0.8	15	0.78	1073	5.3	0.52	28 [46]
$YbCd_{1.6}Zn_{0.4}Sb_2$	0.6	150	1.2	700	20	0.5	5 [26]
$Eu_{0.2}Yb_{0.2}Ca_{0.6}Mg_2Bi_2$	0.7	171	1.3	873	14	0.6	5 [45]

1.5 Summary of Research

As discussed above, the complex bulk thermoelectric materials with intrinsically low lattice thermal conductivity exhibit precisely characteristics desired for thermoelectric application. Zintl phases have recently gained interest for use in thermoelectric devices for power generation because of their intrinsic "electron-crystal, phonon-glass" nature [40]. With general background of different dimensional Zintl structures, this thesis research primarily focuses on two-dimensional layered $CaAl_2Si_2$-type Zintl phases, because electrical transport properties of this kind of structure is outstanding when compared with other dimensional Zintls.

In the past decades, a large number of researches have been focused on Zintl antimonides, analogous Bi-based Zintl materials have received little attention, even given the competitive TE performance of this system. In Chapter 3, the thermoelectric performance of Bi-based Zintl phases, including $CaMg_2Bi_2$, $YbMg_2Bi_2$, $EuMg_2Bi_2$ and their solid solutions, would be discussed in detail. Firstly, it is found a significantly enhanced *ZT* value ~1 is obtained for the optimized samples of $Ca_{1-x}Yb_xMg_2Bi_2$ by ball milling and hot pressing, 150% higher than the reported samples by melting and solidification method. However, a small amount of free Bi is found in all the samples except $YbMg_2Bi_2$. By reducing the initial Bi concentration, we succeed in obtaining phase pure samples in all compositions, which results in a much better thermoelectric performance, especially much higher $(ZT)_{eng}$ and a conversion efficiency near 11%. Furthermore, phase-pure $EuMg_2Bi_2$ is successfully prepared with suppressed bipolar effect

to reach *ZT* ~1. Partial substitution of Eu by Ca and Yb enhances *ZT* to ~1.3 for $Eu_{0.2}Yb_{0.2}Ca_{0.6}Mg_2Bi_2$ at 873 K. With simulation for the optimized $Eu_{0.2}Yb_{0.2}Ca_{0.6}Mg_2Bi_2$ alloys, we confirm chemical disorder has no effect on valence band, but does affect the conduction band, resulting in good p-type TE properties. Those works illuminate the Bi-based Zintl phases as promising TE materials.

It has been previously shown that Zintl compounds $Ca_{1-x}Yb_xZn_2Sb_2$ and $EuZn_2Sb_2$ could be good candidates as thermoelectric materials. However, the conventional synthesis process via melting-solidification-annealing introduces impurities and vacancies, resulting in abnormal high carrier concentration and ultimately low thermoelectric properties. Chapter 4 will report the enhanced thermoelectric performance of $Ca_{1-x}Yb_xZn_2Sb_2$ prepared by ball milling and hot pressing for understanding the defect-controlled Zintl phases. Other compounds $EuZn_2Sb_2$, $Eu_{0.5}Yb_{0.5}Zn_2Sb_2$, and $Eu_{0.5}Ca_{0.5}Zn_2Sb_2$ are also prepared by ball milling and hot pressing to further illustrate it. The highest figure of merit of ~0.9 is achieved in $Ca_{0.25}Yb_{0.75}Zn_2Sb_2$, ~50% higher than the best reported *ZT* in similar materials prepared by melting-solidification-annealing method.

Motivated by the potential good thermoelectric performance in 2-dimensioanl layered Zintls, in chapter 5, we further explore the effect of doping Na into cation site on the thermoelectric transport properties in $Ca_{1-x}Na_xMg_2Bi_{1.98}$ and $Mg_{3-x}Na_xSb_2$. Generally, good thermoelectric performance is found in doped semiconductors, so it is important to be able to control the carrier concentration in Zintl compounds via doping. We select ideal hole dopant Na here, hoping to increase the carrier concentration for better electric property.

However, making competitive n-type Zintl materials has been extremely challenging even though effort has been intensive in the past decade. Very recently, extra Mg in $Mg_{3+x}Sb_2$-based Zintl phase was surprisingly reported to show n-type with a peak figure-of-merit (ZT) ~1.5 at 750 K, but the average ZT is still low. Inspired by this work, chapter 6 will describe a significant improvement on the average ZT by Nb substitution on Mg site in $Mg_{3.2-x}Nb_xSb_{1.5}Bi_{0.49}Te_{0.01}$ that not only leads to an increase in the electrical conductivity and Seebeck coefficient, but also a decrease in the thermal conductivity, resulting in a much higher engineering power factor $(PF)_{eng}$ and figure of merit $(ZT)_{eng}$, and a calculated conversion efficiency above 14% for hot and cold side temperatures at 500 °C and 50 °C, respectively. Such a conversion efficiency makes this material quite competitive among all n-type thermoelectric materials up to 500 °C.

In the last chapter, another excellent p-type thermoelectric material (not Zintl phases), MgAgSb, with low lattice thermal conductivity, will be introduced. For power-generation application with hot side below 473 K, BiSbTe-based alloys have been the only p-type thermoelectric materials for over half a century. Considering its ZT dropping at 373 K and scarce resource of Te, MgAgSb is an important finding for application near room temperature. To tackle the low carrier concentration issue, some efforts have been tried here and proven to be effective. This work highlights the potential of doped MgAgSb for waste-heat recovery applications for heat source temperature below 573 K.

1.6 Reference

[1] F. J. DiSalvo, *Science* **1999**, *285*, 703–706.

[2] L. E. Bell, *Science* **2008**, *321*, 1457–1461.

[3] T. M. Tritt, M. A. Subramanian, *MRS Bull.* **2011**, *31*, 188–198.

[4] D. Kraemer, B. Poudel, H.-P. Feng, J. C. Caylor, B. Yu, X. Yan, Y. Ma, X. Wang, D. Wang, A. Muto, et al., *Nat Mater* **2011**, *10*, 532–538.

[5] M. Zebarjadi, K. Esfarjani, M. S. Dresselhaus, Z. F. Ren, G. Chen, *Energy Environ. Sci.* **2012**, *5*, 5147–5162.

[6] G. J. Snyder, E. S. Toberer, *Nat Mater* **2008**, *7*, 105–114.

[7] A. F. A. F. Ioffe, *Semiconductor Thermoelements, and Thermoelectric Cooling*, Infosearch, Ltd, London, **1957**.

[8] R. D. Abelson, *Thermoelectrics Handbook: Macro to Nano*, CRC/Taylor & Francis, **2006**.

[9] Y. Hu, J. Wang, A. Kawamura, K. Kovnir, S. M. Kauzlarich, *Chem. Mater.* **2014**, *27*, 265–373.

[10] J. C. Peltier, *Ann. Chim.* **1834**, LV1 371.

[11] W. Thomson, *Proc. Roy. Soc. Edinburgh* **1851**, 91–98.

[12] M. Cutler, N. F. Mott, *Phys. Rev.* **1969**, *181*, 1336.

[13] M. Cutler, J. F. Leavy, R. L. Fitzpatrick, *Phys. Rev.* **1964**, *133*, A1143.

[14] R. Franz, G. Wiedemann, *Ann. Phys.* **1853**, *165*, 497–531.

[15] B. Poudel, Q. Hao, Y. Ma, Y. Lan, A. Minnich, B. Yu, X. Yan, D. Wang, A. Muto, D. Vashaee, et al., *Science* **2008**, *320*, 634–638.

[16] Y. Pei, A. D. LaLonde, N. A. Heinz, X. Shi, S. Iwanaga, H. Wang, L. Chen, G. J. Snyder, *Adv. Mater.* **2011**, *23*, 5674–5678.

[17] Y. Pei, H. Wang, G. J. Snyder, *Adv. Mater.* **2012**, *24*, 6125–6135.

[18] Q. Zhang, F. Cao, W. Liu, K. Lukas, B. Yu, S. Chen, C. Opeil, D. Broido, G. Chen, Z. Ren, *J. Am. Chem. Soc.* **2012**, *134*, 10031–10038.

[19] J. P. Dismukes, L. Ekstrom, E. F. Steigmeier, I. Kudman, D. S. Beers, *J.*

Appl. Phys. **1964**, *35*, 2899–2907.

[20] D. M. Rowe, C. M. Bhandari, *Applied Energy* **1980**, *6*, 347–351.

[21] C. B. Vining, W. Laskow, J. O. Hanson, R. R. Van der Beck, P. D. Gorsuch, *J. Appl. Phys.* **1991**, *69*, 4333–4340.

[22] G. Rogl, A. Grytsiv, P. Rogl, E. Bauer, M. Zehetbauer, *Intermetallics* **2011**, *19*, 546–555.

[23] Q. Jie, H. Wang, W. Liu, H. Wang, G. Chen, Z. Ren, *Phys. Chem. Chem. Phys.* **2013**, *15*, 6809–6816.

[24] A. F. May, E. S. Toberer, A. Saramat, G. J. Snyder, *Phys. Rev. B* **2009**, *80*, 125205.

[25] E. S. Toberer, S. R. Brown, T. Ikeda, S. M. Kauzlarich, G. Jeffrey Snyder, *Appl. Phys. Lett.* **2008**, *93*, 062110–4.

[26] X.-J. Wang, M.-B. Tang, H.-H. Chen, X.-X. Yang, J.-T. Zhao, U. Burkhardt, Y. Grin, *Appl. Phys. Lett.* **2009**, *94*, 092106–4.

[27] J. Yang, G. P. Meisner, L. Chen, *Appl. Phys. Lett.* **2004**, *85*, 1140–4.

[28] H. Xie, H. Wang, Y. Pei, C. Fu, X. Liu, G. J. Snyder, X. Zhao, T. Zhu, *Adv. Funct. Mater.* **2013**, *23*, 5123–5130.

[29] J. He, M. G. Kanatzidis, V. P. Dravid, *Materials Today* **2013**, *16*, 166–176.

[30] E. Zintl, W. Dullenkopf, *Zeitschrift für Physikalische Chemie* **1932**, *B16*, 183–194.

[31] E. Zintl, *Angew. Chem.* **1939**, *52*, 1–6.

[32] F. Laves, *Naturwissenschaften* **1941**, *29*, 244–255.

[33] W. Klemm, *Proc. Chem. Soc.* **1958**, *London*, 329–341.

[34] H. Schäfer, B. Eisenmann, W. Müller, *Angew. Chem.* **1973**, *12*, 694–712.

[35] H. Schäfer, *Annual Review of Materials Science* **1985**, *15*, 1–42.

[36] R. Nesper, *Progress in Solid State Chemistry* **1990**, *20*, 1–45.

[37] J. Wang, M. Yang, M.-Y. Pan, S.-Q. Xia, X.-T. Tao, H. He, G. Darone, S. Bobev, *Inorg. Chem.* **2011**, *50*, 8020–8027.

[38] L. Deakin, R. Lam, F. Marsiglio, A. Mar, *Journal of Alloys and Compounds* **2002**, *338*, 69–72.

[39] J. Y. Chan, S. M. Kauzlarich, *Chem. Mater.* **1997**, *9*, 3132–3135.

[40] S. M. Kauzlarich, S. R. Brown, G. Jeffrey Snyder, *Dalton Trans.* **2007**, *21*, 2099–2107.

[41] F. Gascoin, S. Ottensmann, D. Stark, S. M. Haïle, G. J. Snyder, *Adv. Funct. Mater.* **2005**, *15*, 1860–1864.

[42] B. C. Sales, D. Mandrus, R. K. Williams, *Science* **1996**, *272*, 1325.

[43] X. Shi, J. Yang, J. R. Salvador, M. Chi, J. Y. Cho, H. Wang, S. Bai, J. Yang, W. Zhang, L. Chen, *J. Am. Chem. Soc.* **2011**, *133*, 7837–7846.

[44] C. L. Condron, S. M. Kauzlarich, F. Gascoin, G. J. Snyder, *Journal of Solid State Chemistry* **2006**, *179*, 2252–2257.

[45] J. Shuai, H. Geng, Y. Lan, Z. Zhu, C. Wang, Z. Liu, J. Bao, C.-W. Chu, J. Sui, Z. Ren, *Proc Natl Acad Sci USA* **2016**, 201608794–13.

[46] A. Zevalkink, E. S. Toberer, W. G. Zeier, E. Flage-Larsen, G. J. Snyder, *Energy & Environmental Science* **2011**, *4*, 510–518.

[47] E. S. Toberer, A. Zevalkink, N. Crisosto, G. J. Snyder, *Adv. Funct. Mater.* **2010**, *20*, 4375–4380.

[48] S. Ohno, A. Zevalkink, Y. Takagiwa, S. K. Bux, G. J. Snyder, *J. Mater. Chem. A* **2014**, *2*, 7478–6.

[49] N. Kazem, W. Xie, S. Ohno, A. Zevalkink, G. J. Miller, G. J. Snyder, S. M. Kauzlarich, *Chem. Mater.* **2014**, *26*, 1393–1403.

[50] B. Saparov, H. He, X. Zhang, R. Greene, S. Bobev, *Dalton Trans.* **2010**, *39*, 1063–1070.

[51] J. Wang, S.-Q. Xia, X.-T. Tao, *Chem. Asian J.* **2012**, *8*, 251–257.

[52] D. K. Wilson, B. Saparov, S. Bobev, *Z. Elektrochem.* **2011**, *637*, 2018–2025.

[53] O. Y. Zelinska, A. Mar, *Inorg. Chem.* **2008**, *47*, 297–305.

[54] A. P. Holm, M. M. Olmstead, S. M. Kauzlarich, *Inorg. Chem.* **2003**, *42*, 1973–1981.

[55] S. R. Brown, S. M. Kauzlarich, F. Gascoin, G. J. Snyder, *Chem. Mater.* **2006**, *18*, 1873–1877.

[56] J.-A. Paik, E. Brandon, T. Caillat, R. Ewell, J.-P. Fleurial, *Life Testing of*

$Yb_{14}MnSb_{11}$ For High Performance Thermoelectric Couples, **2011**.

[57] Y. Hu, J. Wang, A. Kawamura, K. Kovnir, S. M. Kauzlarich, *Chem. Mater.* **2015**, *27*, 343–351.

[58] G. Cordier, G. Savelsberg, H. Schäfer, *Zeitschrift für Naturforschung B* **1982**, *37*, 975–980.

[59] G. Cordier, H. Schäfer, M. Stelter, *Zeitschrift für Naturforschung B* **1984**, *39*, 727–732.

[60] G. Cordier, H. Schäfer, M. Stelter, **1985**, *40*, 1100–1104.

[61] G. Cordier, H. Schäfer, M. Stelter, **1987**, *42*, 1268–1272.

[62] A. Zevalkink, W. G. Zeier, G. Pomrehn, E. Schechtel, W. Tremel, G. J. Snyder, *Energy Environ. Sci.* **2012**, *5*, 9121.

[63] C. Zheng, R. Hoffmann, R. Nesper, H. G. Von Schnering, *J. Am. Chem. Soc.* **1986**, *108*, 1876–1884.

[64] J. K. Burdett, G. J. Miller, *Chem. Mater.* **1990**, *2*, 12–26.

[65] H. Zhang, M. Baitinger, M.-B. Tang, Z.-Y. Man, H.-H. Chen, X.-X. Yang, Y. Liu, L. Chen, Y. Grin, J.-T. Zhao, *Dalton Trans.* **2010**, *39*, 1101–1104.

[66] E. S. Toberer, C. A. Cox, S. R. Brown, T. Ikeda, A. F. May, S. M. Kauzlarich, G. J. Snyder, *Adv. Funct. Mater.* **2008**, *18*, 2795–2800.

Chapter 2

Characterization of Thermoelectric Materials

2.1 Introduction

With the general background of thermoelectric principles, it is known that electrical conductivity, Seebeck coefficient, and thermal conductivity are the fundamental transport properties and give more insight into the evaluation and prediction of the potential of a thermoelectric material. Experimentally, those material characterization methods, as well as the measurement of carrier concentration and mobility, have became more mature and convenient.

However, it seems inevitable to avoid the experiment errors, including random error and systematic error [1]. Random errors come from the fluctuation from one measurement to the other. Practically, this kind of error could be minimized by averaging the results from multiple measurements. More important aspects of reliable and accurate characterization might result from the systematic errors, which would shift all the measurement in a systematic way. Measurement of a standard sample helps to calibrate the experimental setups, which could be one way to reduce this error. Another effective method is to develop independent characterization technique to compare and double-check the measurement. Be aware of those, the minimization of experimental errors could be achieved.

In this chapter, the measurement techniques and the basics of how they work would be introduced. The electrical resistivity (ρ) and Seebeck coefficient (S) were simultaneously measured on a commercial system (ZEM-3, ULVAC) using the four-point direct current switching method and the static temperature difference method. The thermal conductivity was measured by measuring the thermal diffusivity (D) on a laser-flash apparatus (LFA 457, NETZSCH), specific heat (C_P) on a DSC (404 C, NETZSCH), and volumetric density (ρ_D) by the Archimedes method.

2.2 Seebeck Coefficient Measurement

Compared with other thermoelectric properties measurements, the Seebeck coefficient measurement is much simple, because it is not related to the geometric parameters and not sensitive to the heat loss problem. A simple schematic of a Seebeck measurement system is shown in Fig. 2.1. The sample is laid between a heater and sink and no current is applied through the sample during the measurement. The electric heater mounted on the top creates a temperature gradient. During the process, several small temperature gradients are applied by changing the power goes through the electric heater, then a set of data points are collected and plotted in the ΔV-ΔT curve. The Seebeck coefficient is acquired by the slop of the ΔV-ΔT curve, shown in the Fig. 2.2.

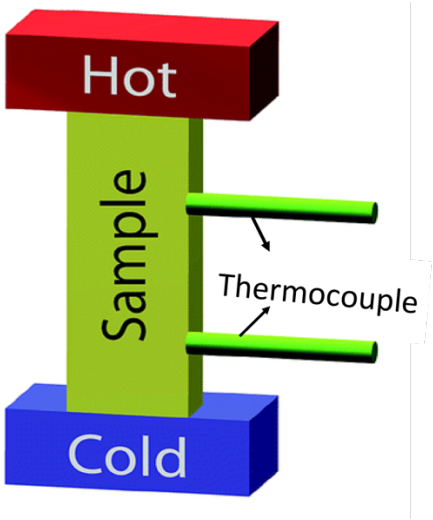

Figure 2.1 Schematic of the Seebeck coefficient measurement.

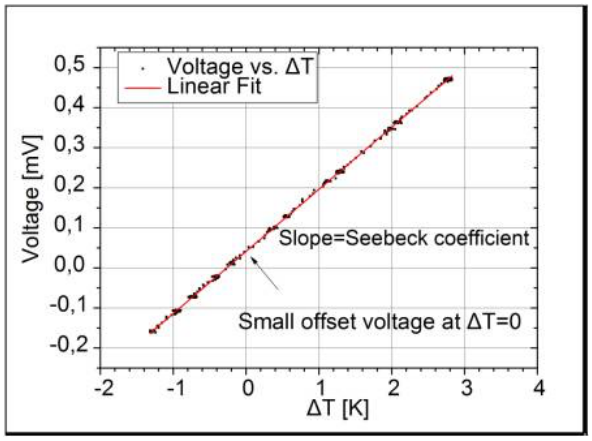

Figure 2.2 Computation of Seebeck coefficient from the slop of the ΔV-ΔT curve.

As can be seen from Fig. 2.1, thermocouples are used for voltage measurement, so Seebeck coefficient obtained above is compensated by the Seebeck coefficient of the thermocouples. Therefore, we should add the Seebeck coefficient of the thermocouples to the value of the slop ($S = S_S + S_T$). Another effect, which should be taken into consideration, is non-zero intercepts, since the ideal ΔV-ΔT line should pass through zero when there is no ΔT. This phenomenon (called dark emf) might be attributed to non equilibrium heat

transport between the sample, thermocouples and accusation system, or other unknown factors. Generally, the Seebeck coefficient measurement is considered reliable when the dark emf does not exceed 10% of the total Seebeck voltage signal.

2.3 Electrical Conductivity Measurement

Electrical conductivity is usually obtained from the electrical resistivity. The four-point probe is the apparatus typically used to determine bulk resistivity. The Fig. 2.3 below shows a schematic of an electrical resistivity measurement system. Current I is made to flow between the outer probes, and voltage V is measured between the two inner probes, ideally without drawing any current. Similar as the Seebeck coefficient measurement, a set of electrical currents are applied, then the voltages are collect. The resistivity is calculated from the relation $\rho = \frac{A\left(\frac{\Delta V}{\Delta I}\right)}{L}$, where A is the cross-sectional area and L is the distance between the inner probes.

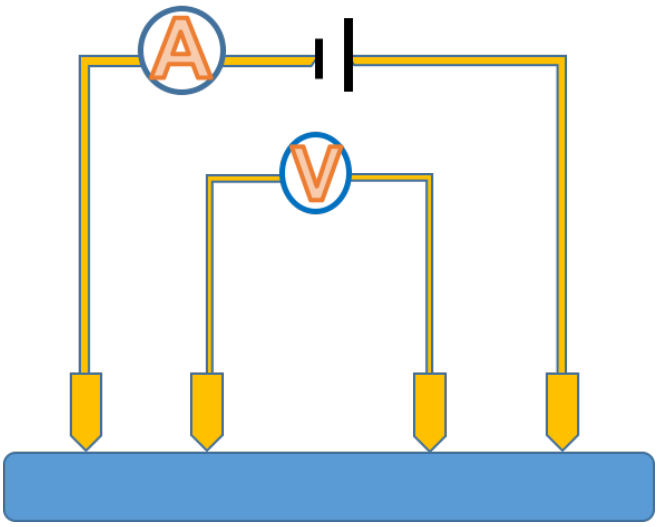

Figure 2.3 Schematic of a four-probe electrical resistivity measurement.

Although the four-point probe method is very convenient and widely used technique, challenges have emerged when it is applied to measure the thermoelectrical materials. The major problem comes from the thermoelectric voltage produced by Peltier effect [2]. When the current is passing the sample, the produced temperature gradient will generate electrical potential difference and thermoelectric voltage. The side-effect voltage will significantly effect the accuracy of real voltage especially for good thermoelectric materials with low resistivity and high Seebeck coefficient. To reduce this effect, it is better to use the high-speed, high-resolution switching DC [3] or an AC current source [4], which would alter direction periodically, to minimize the temperature difference caused by Peltier effect.

2.4 ZEM-3 for Electrical Resistivity and Seebeck Coefficient Measurement

The ZEM-3 is a popular instrument in the filed of thermoelectrics. In our laboratory, we also use this automatic and reliable system to perform the Seebeck coefficient and electrical resistivity measurement simultaneously. The Fig. 2.4 shows the commercial ZEM-3, while the Fig. 2.5 shows a picture of the actual sample mounted on the sample holder. The holder is surrounded by an isothermal nickel radiation shield in order to provide uniform temperature environment across the sample. The measurement is conducted in a helium atmosphere at approximately 0.01 MPa absolute pressure. The lower and upper electrodes with spring force hold the sample firmly in the upright position, ensuring the

good thermal and electrical contact. During the measurement, the lower end of the sample is heated by the electrical resistance heater, producing the temperature gradient across the sample. The formal measurement will be performed when the temperature fluctuation is within a threshold value (0.1 K/10 s). As discussed above, the electrical resistivity is measured by the four-point probe method with alternating DC power supply to ensure the accuracy. The two probe thermocouples also hold against the sample by light spring force. During the Seebeck coefficient measurement, the DC power source are turned off and no current flows through the sample. A set of temperature drops are applied through the sample, the corresponding voltages will be detected. For accuracy, the ZEM-3 usually measures the voltages at 4 different temperature gradients. The Seebeck coefficient of the sample is computed after compensating the contributions from thermocouples as talked before.

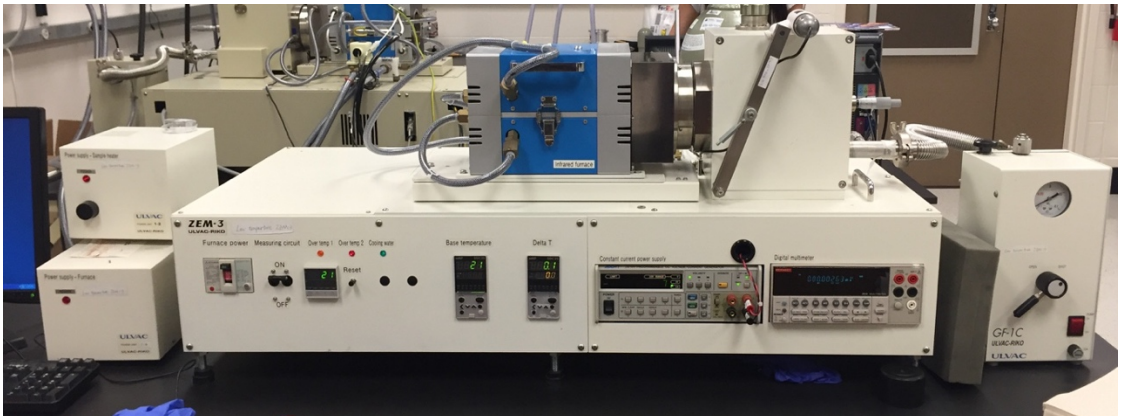

Figure 2.4 Commercial ZEM-3 machine (Ulvac Inc.).

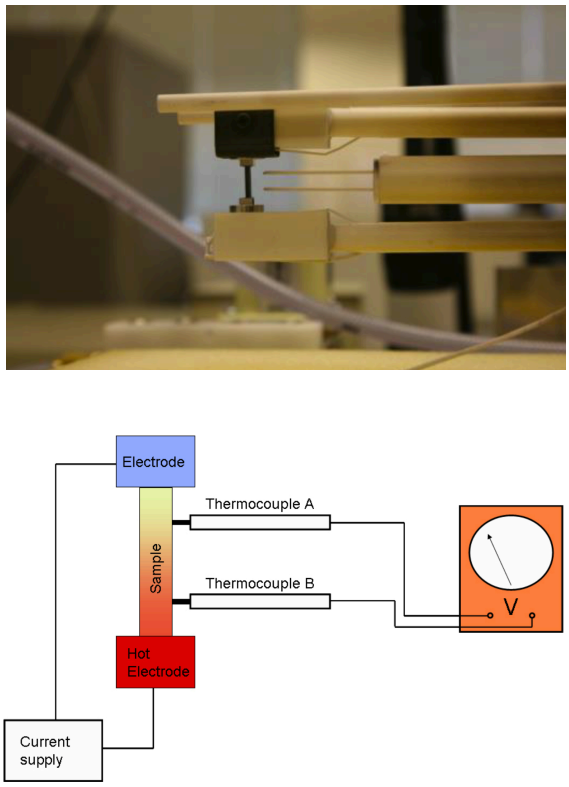

Figure 2.5 Picture (left) and schematic (right) showing the holder with a mounted sample.

2.5 Hall Measurement

If an electric current flows through a conductor in a magnetic field, the magnetic field exerts a transverse force (Lorentz force) on the moving charge carriers which tends to push them to one side of the conductor, creating a potential difference (V_H) across two sides of the conductor. This is called Hall effect [5], most evident in a thin flat conductor as illustrated in the Fig. 2.6. For good thermoelectric materials, the majority carriers (electrons or holes) carry the most of the current. It is noted that the direction of the current

I in the diagram is in the opposite direction for motion of electrons but same direction for holes.

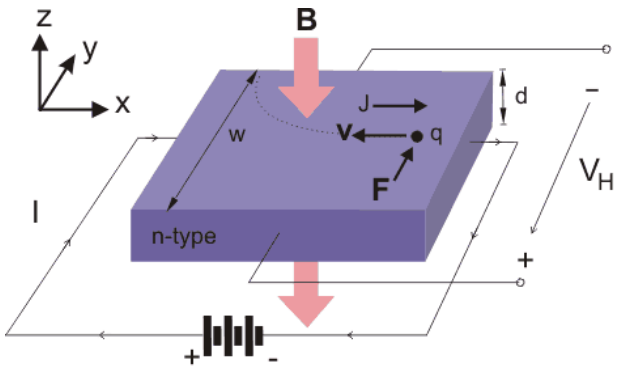

Figure 2.6 Schematic of the Hall Effect in a flat rectangular-shaped semiconductor.

The Hall measurements are performed to determine the fundamental transport properties, such as Hall carrier concentration and Hall mobility. For an *n*-type, flat rectangular-shaped semiconductor such as that shown in Fig. 2.6, the carriers are predominately electrons of bulk density *n*. We assume that a constant current *I* flows along the x-axis from left to right in the presence of a z-directed magnetic field. Electrons subject to the Lorentz force initially drift away from the current direction toward the y-axis, resulting in an excess negative surface electrical charge on this side of the sample. This charge results in the Hall voltage, a potential drop across the two sides of the sample. The Hall voltage is given by

$$V_H = \frac{IB}{qnd} \tag{2.1}$$

where B is the magnetic field, d is the sample thickness, and q (1.602 x 10^{-19} C) is the elementary charge. Thus, the Hall carrier concentration for layer or sheet density ($n_s = nd$) can be obtained as

$$n = \frac{IB}{qdV_H} \tag{2.2}$$

Then one can obtain the equation of hall mobility

$$\mu = 1/Rqn \tag{2.3}$$

where R is the electrical resistance.

In order to determine both the carrier concentration and mobility, here we discuss the van der Pauw technique [6], which is widely used in the semiconductor study due to its convenience. As originally devised by van der Pauw, one can use an arbitrarily shaped thin-plate sample containing four very small contacts placed on the corners of the plate. In experiment, this measurement is performed by using a physical property measurement system (PPMS, Quantum Design, Fig. 2.7).

Figure 2.7 Physical property measurement system for Hall measurement.

The main direction of the Hall measurement through the van der Pauw techniques is to get the Hall voltage to determine the carrier concentration. The Hall voltage

measurement consists of a series of voltage measurements with a constant current *I* and a constant magnetic field *B* (usually 3 T) applied perpendicular to the plane of the sample. For example, when a constant current *I* is forced through the different contacts 1 and 3 and the positive magnetic field *B* is applied, the Hall voltage $V_{24,+}$ (+ for positive B) across the remaining pair of contacts 2 and 4 is measured. Then the current *I* is forced through other different contacts to obtain other three Hall voltages ($V_{42,+}$, $V_{13,+}$,$V_{31,+}$). Next, the negative magnetic *B* is applied, another four Hall voltages are measured as described before. Once the eight Hall voltages are acquired, the average voltage is given by

$$V_H = \frac{\left(V_{13,+}+V_{31,+} + V_{24,+} + V_{42,+}\right) - \left(V_{13,-} + V_{31,-} + V_{42,-} + V_{24,-}\right)}{8} \tag{2.4}$$

Then based on the equation 2.2 and the measured thickness of the sample, the carrier concentration can be obtained.

It must be noted there are practical aspects which must be considered when carrying out Hall measurement. Primary concerns are samples preparation. It is preferable to fabricate samples from thin plates of the semiconductor material and to adopt a suitable geometry, as shown in Fig. 2.8. The average diameters (*D*) of the contacts, and sample thickness (*d*) must be much smaller than the distance between the contacts (*L*). Relative errors caused by non-zero values of *D* are of the order of *D*/*L*. Besides, one must also concern the thermomagnetic effects due to non-uniform temperature, and photoconductive and photovoltaic effects which can be minimized by measuring in a dark environment.

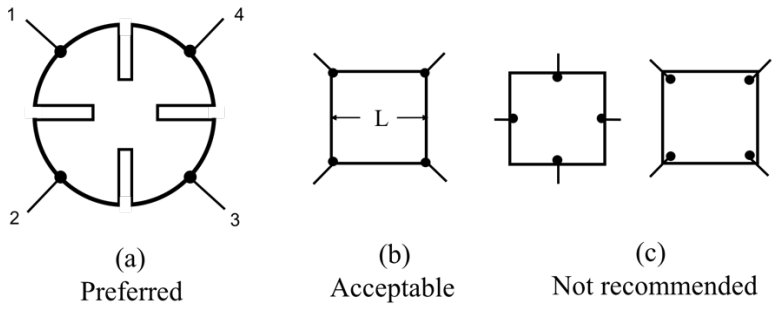

Figure 2.8 Thin plates of the semiconductor material adopting a suitable geometry.

2.6 Thermal Conductivity Measurement

Thermal conductivity is usually defined as the property of a material to conduct heat. It can be evaluated by Fourier's law and written as

$$\tilde{q} = -k\nabla T \tag{2.5}$$

where $\tilde{q}$ is the local heat flux density and k is thermal conductivity. The heat flux density is the amount of energy that flows through a unit area per unit time. The reliable thermal conductivity values are essential in a selection of a thermoelectric material.

However, it can be treated as one of the thermoelectric properties whose measurement is very difficult and it prefers high precision in the determination of the parameters involved in its calculation. This challenging mainly comes from the heat losses through conduction, convention, radiation, and thermal contact resistance at junctions.

In thermoelectric research, the laser-flash method is the most used technique nowadays in determining the thermal conductivity of a thermoelectric material. It was

developed by Parker *et al.* in 1961 [7] and has been improved subsequently later [8-12]. This technique relies on a laser power source to eliminate the problem of thermal contact resistance, while the heat loss is minimized by keeping the measurement in short enough time.

In our experiment, usually the thermal conductivity is not measured directly, it is calculated as a product of the thermal diffusivity (D) on a laser-flash apparatus (LFA 457, NETZSCH), specific heat (C_P) on a DSC (404 C, NETZSCH), and volumetric density (ρ_D).

2.6.1 LFA 457

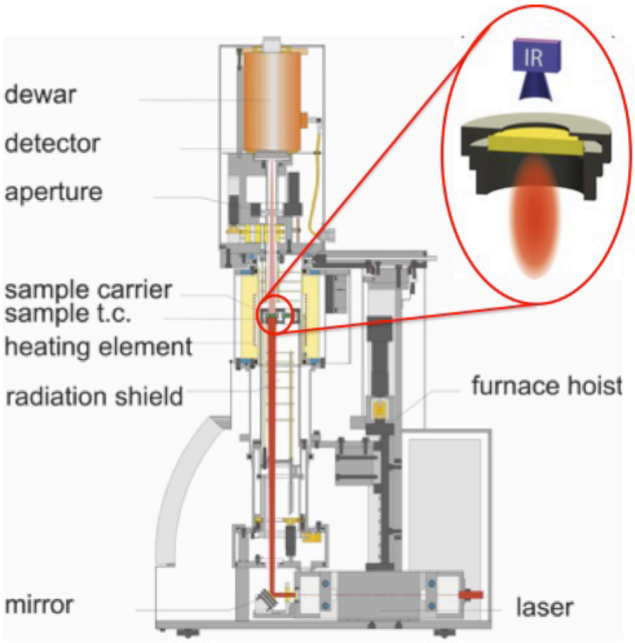

Figure 2.9 A sketch of the laser-flash system for thermal conductivity measurement.

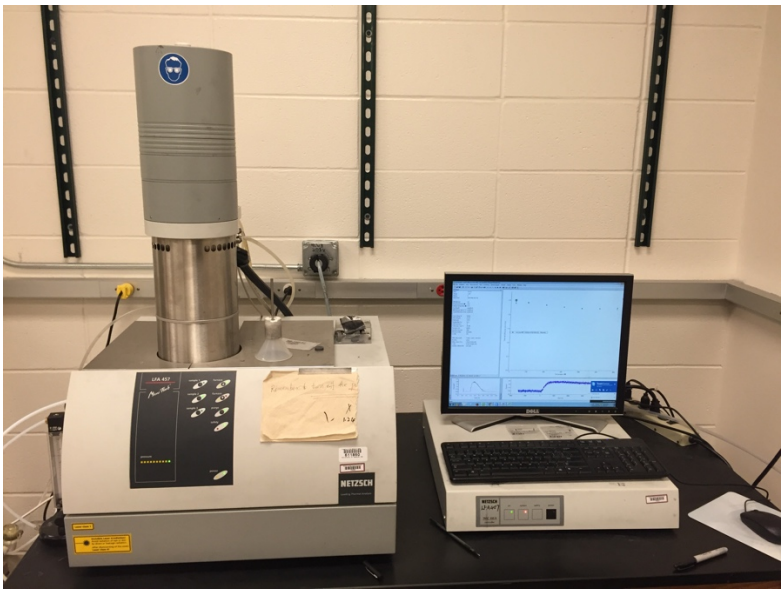

Figure 2.10 The laser-flash equipment (LFA 457, NETZSCH) for thermal conductivity measurement.

Thermal diffusivity (a with the unit mm^2/s) is a material-specific property for characterizing unsteady heat conduction. This value describes how quickly a material reacts to a change in temperature. A sketch of the laser-flash system is shown Fig. 2.9 and picture of the equipment is shown in Fig. 2.10. In a typical LFA 457 system, three samples can be loaded at the same time in the middle small furnace. A sample usually has 12.7 mm diameter and the thickness is ranging from 1-2 mm. The sample disc is placed between the laser beam and an InSb IR detector. The temperature of samples is controlled by the thermocouple placed close to the sample holders (inset of Fig. 2.9). In carrying out a measurement, the lower surface of a plane parallel sample is first heated by a short energy pulse. Usually the samples are coated with graphite to ensure better light absorption. Once the heat pulse travels through the sample, the resulting temperature change on the rear face of the sample is then measured with an infrared detector.

Considering ideal one-dimensional thermal diffusion transport case [13], and assuming no heat losses occur, the normalized temperature increase on the rear face is given by

$$V = 1 + 2\sum_{n=1}^{\infty}(-1)^n \exp(-n^2 w) \tag{2.6}$$

where: $w = \pi^2 D\, t/L^2$, V=T/T_m is dimensionless temperature increase of the rear face, T is instantaneous temperature increase of the rear face of the specimen; $T_m = Q/\rho c_P L$ is maximum temperature increase of the rear face, Q is input energy on the front face, L is the specimen length and D is thermal diffusivity.

A common practice way is to use the half time ($t_{1/2}$, time value at half signal height) for which w is equal to 1.38, then the thermal diffusivity can be given by

$$D = 0.138\frac{l^2}{\pi^2 t_{1/2}} \tag{2.7}$$

Once the thermal conductivity is determined, the thermal conductivity could be obtained with the knowledge of the specific heat and the density.

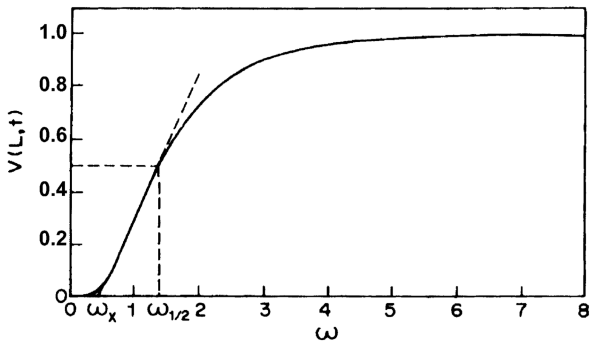

Figure 2.11 Temperature rise curve plotted against dimensionless time ω.

2.6.2 Differential Scanning Calorimeter for Specific Heat Capacity

Specific heat capacity (C_p) is a physical quantity describing the energy required to result a certain change in the temperature of a unit mass of the material. To measure this property, a differential scanning calorimeter is employed to measure specific heat capacity by comparing the temperature difference between the sample and a reference upon heating.

The measurement setup is shown in Fig. 2.12. Sample and reference crucibles are placed on a sample carrier, and temperature is detected by thermocouples in contact with each crucible. The cylindrical furnace, as shown in Fig. 2.13, is performed to generate heat radially towards the center. It is needed to carry out three major measurements for determining the specific heat. First is the baseline measurement. In this process, both crucibles are left empty and heated to the desired temperature. This test has to be measured at least twice until the yielded baseline curves overlap, ensuring the system is running consistently. After a repeatable baseline has been recorded, next step is testing a reference. The reference with a well defined specific heat is measured for later comparison to the experimental sample. Finally, a thermoelectric sample is tested in the same way as the reference. The final C_p could be determined by using the ratio method.

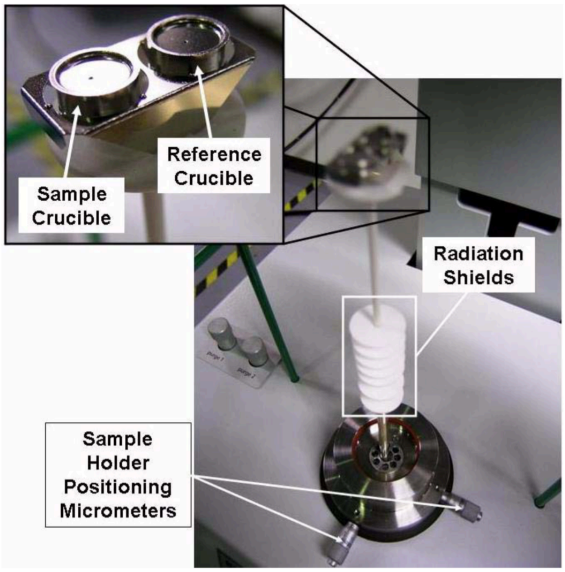

Figure 2.12 Crucibles and sample carrier adjustment micrometers.

Figure 2.13 DSC 404C for specific heat measurement.

2.7 References

[1] J. R. Taylor, *Mill Valley, CA: Anonymous University Science Books* **1982**, 71.

[2] J. C. Peltier, *Ann. Chim.* **1834**, LV1 371.

[3] T. M. Dauphinee, S. B. Woods, *Review of Scientific Instruments* **1955**, *26*, 693–695.

[4] W. Klemm, *Proc. Chem. Soc.* **1958**, *London*, 329–341.

[5] E. H. Hall, *American Journal of Mathematics* **1879**, *2*, 287–292.

[6] L. van der PAUYV, *Philips Res. Rep.* **1958**, *13*, 1–9.

[7] W. J. Parker, R. J. Jenkins, C. P. Butler, G. L. Abbott, *J. Appl. Phys.* **1961**, *32*, 1679–1684.

[8] R. D. Cowan, *J. Appl. Phys.* **1963**, *34*, 926–927.

[9] J. Cape, G. W. Lehman, *J. Appl. Phys.* **1963**, *34*, 1909–1913.

[10] F. Righini, A. Cezairliyan, *High Temperature—High Pressures* **1973**, *5*, 481–501.

[11] R. A. Langley, J. Bohdansky, W. Eckstein, P. Mioduszewski, J. Roth, E. Taglauer, E. W. Thomas, H. Verbeek, K. L. Wilson, *Nuclear Fusion* **1984**, *24*, S9.

[12] J. Blumm, J. Opfermann, *High Temperatures. High Pressures* **2002**, *34*, 515–521.

[13] H. S. Carslaw, J. C. Jaeger, *Conduction of Heat in Solids*, Oxford University Press**,** New York **1959.**

Chapter 3

Thermoelectric Properties of AMg_2Bi_2 (A = Ca, Yb, Eu)

3.1 Introduction

The complex Zintl phases, especially Sb-based Zintl compounds, have been demonstrated to be promising TE materials for middle- to high-temperature applications. Remarkable achievements have been reported with maximal *ZT* around or more than 1, *e.g.*, β-Zn_4Sb_3 [1,2], $Yb_{14}Mn_{1-x}Al_xSb_{11}$ [3,4], and $A_yMo_3Sb_{7-x}Te_x$ [5]. In particular, Zintl phases AB_2Sb_2 (A = Ca, Yb, Eu, Sr; B = Zn, Mn, Cd, Mg) [6-10] crystallizing in $CaAl_2Si_2$ structure (Fig. 1.7) have been extensively studied with the highest *ZT* for $YbZn_{0.4}Cd_{1.6}Sb_2$ ~1.2 at 700 K.

The A-sites of these materials have been shown to contain exclusively divalent ions, which are limited to alkaline earth-based and rare earth-based elements like Eu and Yb, while B is a d^0, d^5, d^{10} transition metal or a main-group element like Mg^{2+} [11,12]. In spite of the extensive research on Zintl antimonides, analogous Bi-based Zintl materials have received little attention, even given the competitive TE performance of this system. For the $CaAl_2Si_2$ type Zintl phases, the crystal structures of both alkaline earth-based and rare earth-based AMg_2Bi_2 (A = Mg, Ca, Sr, Ba, Yb, Eu, Sm) have been reported [13-15]. However, the reported *ZT* is ~0.4 in $YbMg_2Bi_2$ and ~0.1 in $CaMg_2Bi_2$ and $EuMg_2Bi_2$ via melting, grinding, and annealing, not good enough for practical applications.

Through ball milling and hot pressing, the significantly enhanced thermoelectric properties have been achieved in those Bi-based Zintl materials, which will be described in the following sections. The experimental methods and simulation details are introduced in Section 3.2. Section 3.3 discusses the thermoelectric properties of solid solution $Ca_{1-x}Yb_xMg_2Bi_2$, along with the higher average *ZT* and conversion efficiency in Bi-reduced $Ca_{1-x}Yb_xMg_2Bi_y$ system. Section 3.4 studies the another base sample $EuMg_2Bi_2$ and more disordered (Ca,Yb,Eu)Mg_2Bi_2 Zintl phases, while some electronic calculations and lattice dynamic calculations are also included.

3.2 Experimental Methods and Simulation Details

Synthesis. A series of samples $Ca_{1-x}Yb_xMg_2Bi_2$ (x = 0, 0.3, 0.5, 0.7, and 1); $CaMg_2Bi_{1.98}$ and $Ca_{0.5}Yb_{0.5}Mg_2Bi_{1.99}$; $EuMg_2Bi_2$, $Eu_{0.5}Yb_{0.5}Mg_2Bi_2$, $Eu_{0.5}Ca_{0.5}Mg_2Bi_2$, and $(Eu_{0.5}Yb_{0.5})_{1-x}Ca_xMg_2Bi_2$ (x = 0.4, 0.5, 0.6, and 0.7); $Ca_{1-x}Na_xMg_2Bi_{1.98}$ (x = 0, 0.0025, 0.005, and 0.0075) were prepared by ball milling followed by hot pressing. Starting with calcium (Ca, Sigma Aldrich, 99.9%, pieces), ytterbium (Yb, Sigma Aldrich, 99.9%, cubes), europium (Eu, Atlantic, 99.9%, cubes), magnesium (Mg, Sigma Aldrich, 99.9%, pieces), sodium (Na, Sigma Aldrich, 99.9%, cubes), and bismuth (Bi, Sigma Aldrich, 99.999%, chunks), the elements were weighed and then loaded in a stainless steel jar with stainless steel balls for mechanical alloying by a high energy ball mill (SPEX 8000D) for 12 h. The final nanopowder was then loaded into a graphite die with an inner diameter of 12.7 mm, and consolidated by alternating current (AC) hot pressing at ~933 K for 2 min.

Characterization. A PANalytical multipurpose diffractometer with an X'celerator detector (PANalytical X'Pert Pro) was used to characterize the phases. Morphology and elemental ratios were characterized by scanning electron microscopy (SEM, LEO 1525) and Electron Probe Micro-Analysis (EPMA, JXA-8600), respectively. Transmission-electron microscopy (TEM, JEOL 2100F) was used to analyze the detailed microstructures. A Nicolet iS50 FT-IR Spectrometer with a Spectra-Tech Model 500 Series Variable Angle Specular Reflectance Accessory was used to measure the band gap.

Measurements. The electrical resistivity (ρ) and Seebeck coefficient (S) were simultaneously measured on a commercial system (ZEM-3, ULVAC) using the four-point direct current switching method and the static temperature difference method. The thermal conductivity was measured by measuring the thermal diffusivity (D) on a laser-flash apparatus (LFA 457, NETZSCH), specific heat (C_P) on a DSC (404 C, NETZSCH), and volumetric density (ρ_D) by the Archimedes method. The total thermal conductivity (κ) was calculated by $\kappa = D\rho_D C_p$. The carrier concentration (n) was obtained by Hall effect measurement (Van der Pauw method) at room temperature using a modified sample puck in a Physical Properties Measurement System (PPMS D060, Quantum Design) under a magnetic field of 3 Tesla. The Hall mobility (μ) was estimated by $1/\rho = ne\mu$ with electrical resistivity ρ from a ZEM-3 instrument. It is understood that there is a 3% error in the electrical resistivity, 5% in the Seebeck coefficient, and 5% in the thermal conductivity, resulting in an error of around 14% for ZT. For better readability of the figures, we have deliberately plotted the curves without the error bars.

Electronic calculation. The electronic structure was calculated by the density-functional theory (DFT) as implemented in the open-source Quantum Espresso program package [16]. The exchange-correlation function was taken within the generalized gradient approximation (GGA) in the parameterization of Perdew–Burke–Ernzerhof (PBE) [16,17]. All 4*f* states of Eu and Yb were included in the current calculations. Due to the self-interaction errors, the standard DFT methods cannot handle the partially filled and sometimes even closed f electrons. As an alternative we used the DFT+*U* formalism [18], in which we included a Hubbard *U* parameter to account for the on-site Coulomb interaction. A *U* of 6 eV for Eu and 9 eV for Yb were selected in order to shift the localized *f* states away from the Fermi level. The value of *U* is selected so that the *f* states lay just below the topmost *p* states of the valance band. We choose it simply because this separates the strongly localized *f* states from other states needed for the generation of maximally localized Wannier functions. A plane-wave basis was adopted for the expansion of the valence electron wave functions with kinetic-energy cutoffs of 80 Ry. For ground state calculations we used an 8×8×8 Monkhorst–Pack k-point mesh. From the ground state density, the Bloch states have been computed on a 4×4×4 mesh. To analyze the nature of the chemical bonding in the ordered compounds, selected conduction bands were projected onto maximally localized Wannier functions (MLWF) using the wannier90 code [19].

Furthermore, the electronic structure calculations of substituted (Ca,Eu,Yb)Mg_2Bi_2 compounds have been performed by means of the scalar relativistic Korringa–Kohn–Rostoker (KKR) method in combination with the coherent potential approximation (CPA)

as implemented in the AkaiKKR (machikaneyama) program package [20,21]. The calculations were performed in the scalar relativistic mode by solving the Dirac equation for core and valence states. The Moruzzi, Janak, and Williams (MJW) method was used for the parameterization of the exchange energy. The k-integration mesh was set to a size of (7×7×7) during the self-consistent cycles (213 k-points in the irreducible wedge of the Brillouin zone). The Ca, Eu, or Yb atoms are placed on the 1a Wyckoff position, and the Mg and Bi atoms are placed on the 2d positions.

Lattice dynamics calculation. The density functional perturbation theory (DFPT), implemented in the PHonon code of the Quantum Espresso distribution (34), was used for $CaMg_2Bi_2$, $EuMg_2Bi_2$, and $YbMg_2Bi_2$ lattice dynamics calculations. The self-consistent calculations were done in a scalar relativistic approximation, with the PBE GGA, and an energy cutoff of 80 Ry was used for the plane-wave expansion. A 8×8×8 k-space grid was used for these self-consistent calculations, resulting in 65 k points in the irreducible Brillouin zone. Once self-consistency was achieved, the PHonon code was used to generate the second order force constants from the basic unit cell. Based on the obtained force constants, the phonon dispersions and densities-of-states were calculated. The phonon density of states is shown with a Gaussian broadening of 0.75 cm^{-1}.

3.3 Thermoelectric Performance of $Ca_{1-x}Yb_xMg_2Bi_y$ Alloys

Reproduced with permission from *Journal of Materials Chemistry A*, 4, 4312-4320 (2016).

3.3.1 $Ca_{1-x}Yb_xMg_2Bi_2$

Fig. 3.1a shows the XRD patterns of $Ca_{1-x}Yb_xMg_2Bi_2$ with x = 0, 0.3, 0.5, 0.7, and 1. All diffraction peaks are indexed according to the reported structure of $CaAl_2Si_2$ (space group $P\bar{3}m1$, No. 164). The results indicate that Yb has successfully substituted Ca to form $Ca_{1-x}Yb_xMg_2Bi_2$ solid solutions. Little variation is observed in the lattice parameters a and c of all compounds because of similar size of Ca^{2+} and Yb^{2+} (Fig. 3.1b). There is a small amount of free Bi as the impurity phase indicated by the arrow in the figure except for the case when x = 1, consistent with other groups' prior reports [11]. However, with increasing Yb content, the impurity peaks gradually disappear. By applying the Zintl concept, the structure of $Ca_{1-x}Yb_xMg_2Bi_2$ can be described as the anionic building block $(Mg_2Bi_2)^{2-}$ with divalent cations (Ca^{2+} and $Yb^{2+)}$ seating between the chains to provide electrons.

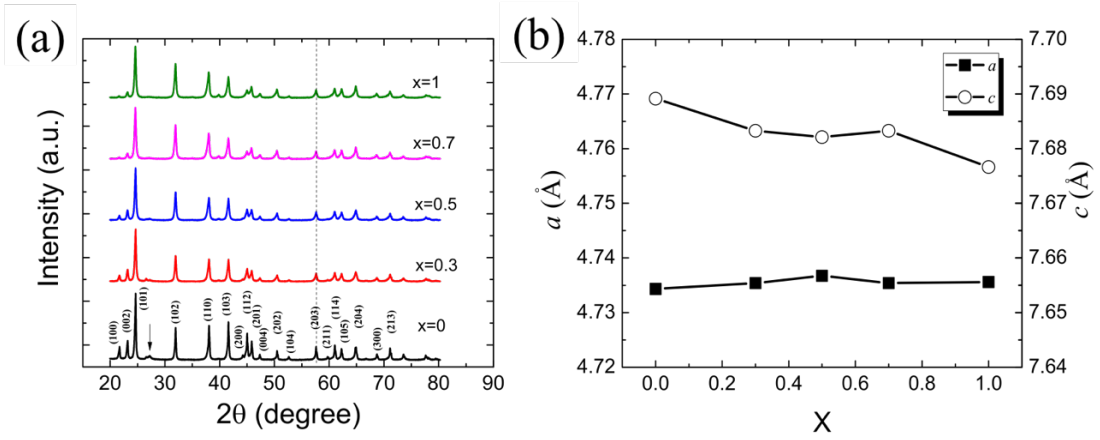

Figure 3.1 (a) XRD patterns of $Ca_{1-x}Yb_xMg_2Bi_2$ (x = 0, 0.3, 0.5, 0.7, and 1); (b) dependence of the unit-cell parameters on the Yb content x.

Fig. 3.2a shows the temperature-dependent electrical conductivity of $Ca_{1-x}Yb_xMg_2Bi_2$ samples. For pure Ca containing compound $CaMg_2Bi_2$, the electrical conductivity first decreases with increasing temperature due to phonon scattering, and then reaches a minimum and increases. Moreover, the electrical conductivity increases with increasing Yb concentration, which might be attributed to the increased carrier concentration shown in Table 3.1, despite a small reduction in Hall mobility. The carrier concentration (n) and Hall mobility (μ) listed in Table 3.1 affect the electrical conductivity (σ) by the relationship $\sigma = ne\mu$. Although both calcium ion and ytterbium ion used as cations in zintl phase with the similar size, the difference in electronegativity results in the different electrical properties. Because the dominant carriers are holes and calcium is more electropositive than ytterbium, calcium-rich compound means more electrons transfer, resulting in lower hole concentration.

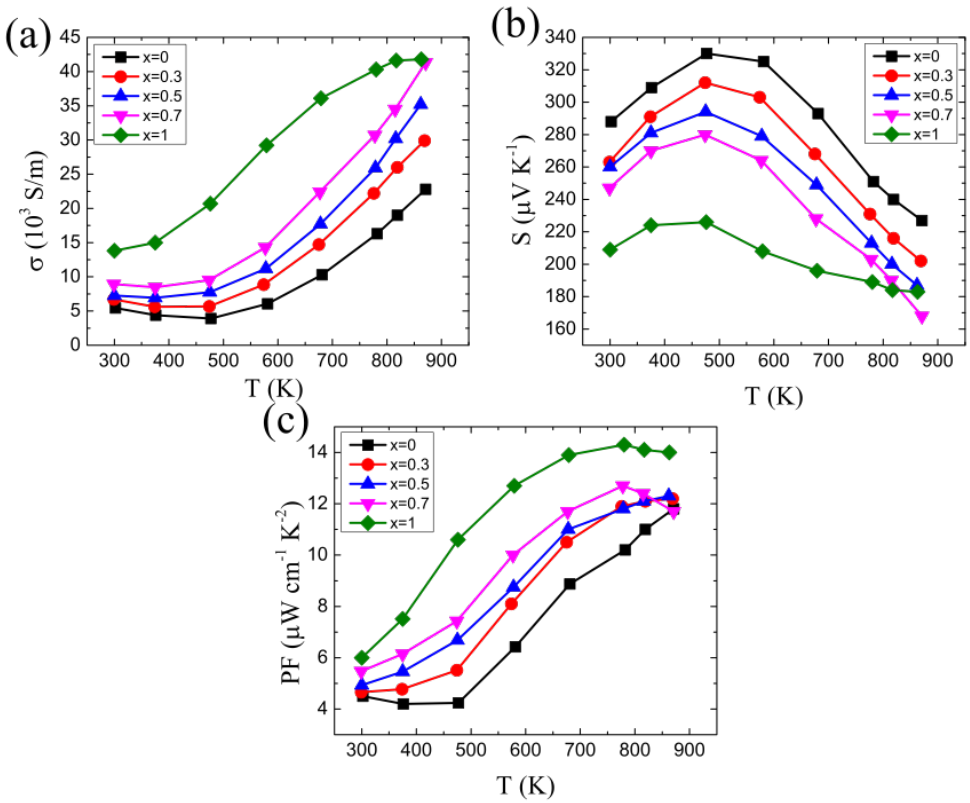

Figure 3.2 Temperature-dependent electronic transport properties of $Ca_{1-x}Yb_xMg_2Bi_2$ (x = 0, 0.3, 0.5, 0.7, and 1): (a) electrical conductivity; (b) Seebeck coefficient; and (c) power factor.

Fig. 3.2b represents the temperature-dependent Seebeck coefficient of all $Ca_{1-x}Yb_xMg_2Bi_2$ samples. Seebeck coefficient first increases with temperature, reaches a maximum and then decreases. And the Seebeck coefficient decreases as x increases, a consequence of the increased carrier concentration. Based on the single band model, a rough estimation of the effective mass can be obtained by the following Eq. 3.1-3 [22].

$$m^* = \frac{h^2}{2k_B T}\left[\frac{n}{4\pi F_{1/2}(\eta)}\right]^{2/3} \tag{3.1}$$

$$S = \pm\frac{k_B}{e}\left(\frac{(r+3/2)F_{r+3/2}(\eta)}{(r+3/2)F_{r+1/2}(\eta)} - \eta\right) \tag{3.2}$$

$$F_n(\eta) = \int_0^\infty \frac{\chi^n}{1 + e^{\chi - \eta}} d\chi \qquad (3.3)$$

Where $F_n(\eta)$ is the n^{th}-order Fermi integral, η the reduced Fermi energy, r the scattering factor, h the Plank constant, k_B the Boltzmann constant, and e the electron charge. As acoustic phonon scattering is commonly the main scattering mechanism for most thermoelectric materials, the scattering factor r could be considered as -1/2 in calculation [23]. These relationships give $m^* = 0.6 \pm 0.05\ m_e$, for all x values, shown in Table 3.1. Combining the electrical conductivity and Seebeck coefficient, the power factors of all samples are shown in Fig. 3.2c. With more Yb concentration, the power factor increases due to the increased carrier concentration.

Table 3.1 Room-temperature thermoelectric transport properties of $Ca_{1-x}Yb_xMg_2Bi_2$.

$Ca_{1-x}Yb_xMg_2Bi_2$	$x = 0$	$x = 0.3$	$x = 0.5$	$x = 0.7$	$x = 1$
Carrier concentration (10^{18} cm^{-3})	2.38	2.75	3.29	4.26	7.2
Hall mobility (cm^2 V^{-1} s^{-1})	143	153	138	131	119
Effective mass (m_e)	0.62	0.56	0.61	0.65	0.66

Fig. 3.3 shows the temperature-dependent thermal transport behavior of $Ca_{1-x}Yb_xMg_2Bi_2$. Specific heat (C_p) for all samples is shown in Fig. 3.3a. For samples containing Ca, the peaks around 543 K are observed which indicates there is a phase transition. This is mainly because of the existence of impurity phase Bi, as shown in Fig. 3.1a. And the same phenomenon has been observed in Bi_2Te_3 [24], the DSC curve is assigned to free bismuth melting. The melting point of Bi is 544 K, confirmed by the peak

observed in specific heat measurement, shown in Fig. 3.3a. With increasing x, because of decreasing impurity Bi, the impurity peak decreases and finally vanishes. To demonstrate free Bi does exist in some compositions, the optimized composition $Ca_{0.5}Yb_{0.5}Mg_2Bi_2$ was chosen to measure the high temperature XRD. The XRD patterns of powder sample were measured at 523 K and 573 K, and then measured again after cooling down to room temperature. When temperature of 523 K is lower than the melting point (544 K) of Bi, the XRD peak (around 27^o) is clearly seen in Fig. 3.3b. However, the XRD peak of the impurity phase Bi disappears when measured at temperature of 573 K, a clear demonstration of existence of Bi, which means Bi have melted or possibly got into the lattice. When the sample was cooled down to room temperature, the impurity phase Bi appears again. The high temperature XRD patterns results indicate the free Bi is indeed in the compound.

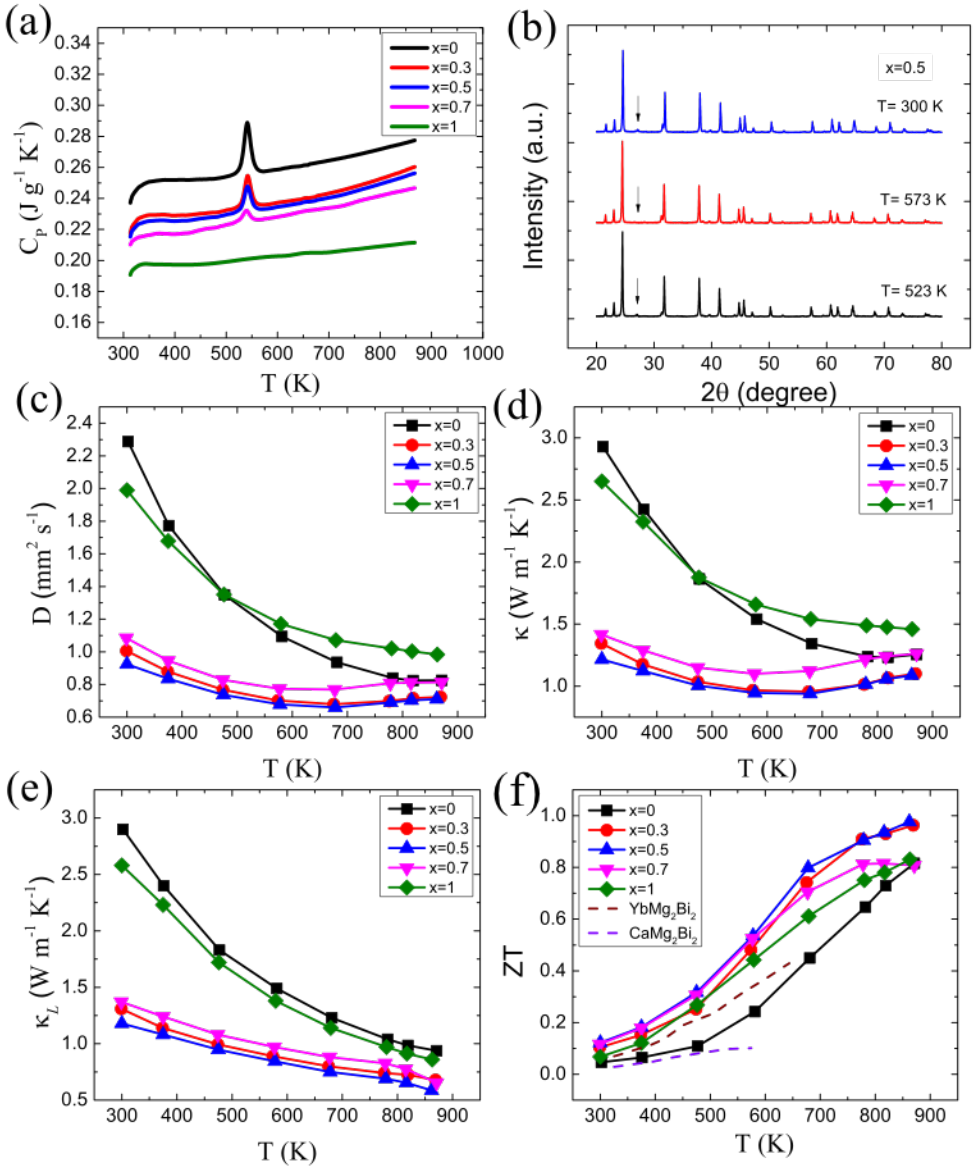

Figure 3.3 Temperature-dependent thermal transport properties of $Ca_{1-x}Yb_xMg_2Bi_2$ (x = 0, 0.3, 0.5, 0.7, and 1): (a) Specific heat; (c) thermal diffusivity; (d) total thermal conductivity; (e) lattice thermal conductivity; and (f) *ZT* values. (b) XRD patterns of $Ca_{0.5}Yb_{0.5}Mg_2Bi_2$ at 523 K, 573 K and 300 K (after cooling down).

Fig. 3.3c shows the thermal diffusivity of all samples. With increasing temperature, the diffusivity (D) of both $CaMg_2Bi_2$ and $YbMg_2Bi_2$ shows gradually decreased tendency,

while the diffusivity of mixed Ca and Yb compounds first decreases and then increases due to intrinsic excitation. C_p and D are used to calculate the total thermal conductivity (κ) of all the doped samples by $\kappa = D\rho_D C_p$, where ρ_D is the measured density of samples. The densities of all the samples $Ca_{1-x}Yb_xMg_2Bi_2$ with x = 0, 0.3, 0.5, 0.7, and 1 measured by Archimedes method are 5.50, 5.74, 6.20, 6.48, and 7.03 g cm^{-3}, respectively. The temperature dependence of the total thermal conductivity (κ) of all samples is plotted in Fig. 3.3d. Similar as the thermal diffusivity, the thermal conductivity of the Ca/Yb mixed compounds is expected to be lower than those of $CaMg_2Bi_2$ and $YbMg_2Bi_2$ because of the disorder introduced in the structure, which is the same mechanism as reported in the compounds $Ca_xYb_{1-x}Zn_2Sb_2$ [6]. The lattice thermal conductivity (κ_L), shown in Fig. 3.3e, is obtained by directly subtracting the electronic contribution (κ_e) from the total thermal conductivity. κ_e could be estimated by using the Wiedemann−Franz relationship ($\kappa_e = LT/\rho$), where L is the Lorenz number, approximated using a single parabolic band model. As excepted, the κ_L exhibits significant reduction in Ca/Yb mixed samples.

The figure-of-merit ZT versus temperature and Yb content x is plotted in Fig. 3.3f. With increasing temperature, ZT increases continuously. At 873 K, ZT reaches a maximum of ~1 for x = 0.5, owing to the lower thermal conductivity than other samples. The highest ZTs obtained for $CaMg_2Bi_2$ and $YbMg_2Bi_2$ are both ~0.8, much higher than the ZT ~0.1 for $CaMg_2Bi_2$ and ZT ~0.44 for $YbMg_2Bi_2$ by Andrew F. May *et al.* [14].

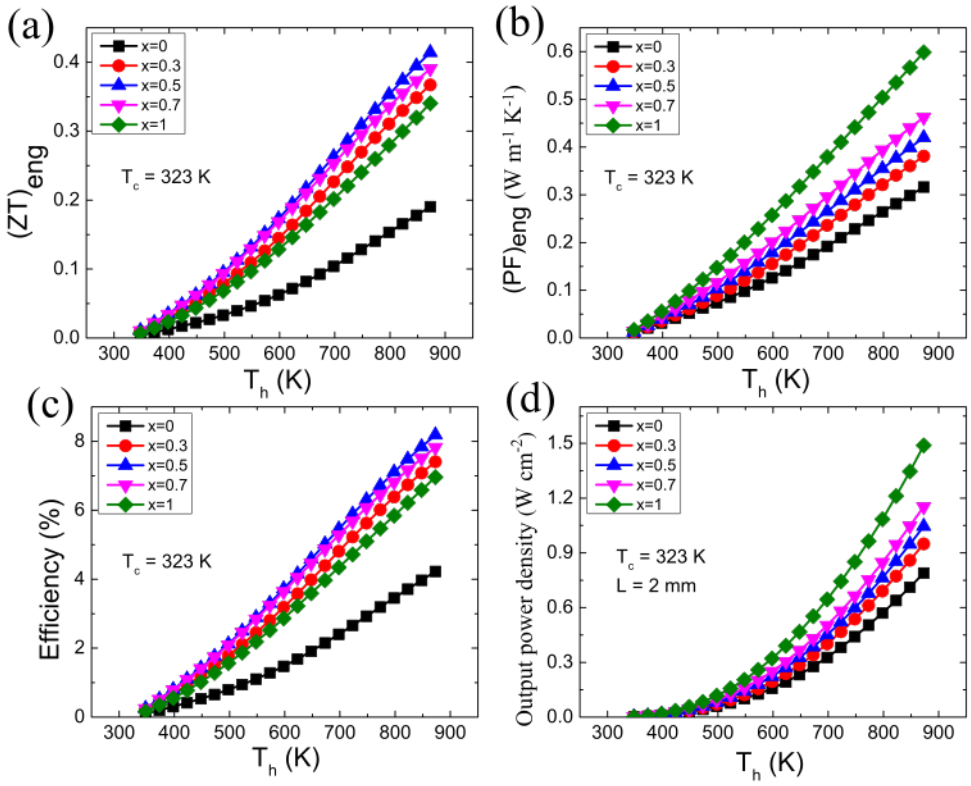

Figure 3.4 Calculated $(ZT)_{eng}$ (a) and $(PF)_{eng}$ (b) dependence of T_h at 873 K and T_c at 323 K for $Ca_{1-x}Yb_xMg_2Bi_2$ (x = 0, 0.3, 0.5, 0.7, and 1), efficiency (c) and Output power density (d) as a function of temperature gradient.

However, since ZT only indicates the ratio of electrical to thermal characteristics at each instantaneous temperature, it cannot indicate the practical efficiency of a TE material at a large temperature gradient between the cold and hot sides. Instead of using the peak ZT, Kim *et al*. proposed the engineering dimensionless figure of merit $(ZT)_{eng}$ as a function of thermal boundaries, *i.e*., the temperatures of hot side T_h and cold side T_c to reliably predict the possible efficiency and output power density. Fig. 3.4a and b shows the calculated $(ZT)_{eng}$ and $(PF)_{eng}$ dependence of the hot-side temperature up to 873 K while the cold-side temperature is kept at 323 K. It shows that the optimized sample with x = 0.5 improves the materials' performance by a factor of 2 in terms of $(ZT)_{eng}$ as compared with

the undoped sample with $x = 0$. Based on $(ZT)_{eng}$, $Ca_{0.3}Yb_{0.7}Mg_2Bi_2$ displays higher performance than $Ca_{0.7}Yb_{0.3}Mg_2Bi_2$ even though the peak ZT of the latter is higher than the former at T_h = 873 K. Assuming T_c = 323 K and 2 mm of leg length, we have calculated the maximum efficiency η_{max} and its corresponding output power density P_d including Thomson heat based on $(ZT)_{eng}$ and $(PF)_{eng}$. The conversion efficiency of the optimized $Ca_{0.5}Yb_{0.5}Mg_2Bi_2$ is about 8.2% at ΔT = 550 °C, shown in Fig. 3.4c. Fig. 3.4d shows $YbMg_2Bi_2$ has the best output power density of 1.5 W cm^{-2} because of the higher power factor among all the $Ca_{1-x}Yb_xMg_2Bi_2$ compounds.

3.3.2 $CaMg_2Bi_{1.98}$ and $Ca_{0.5}Yb_{0.5}Mg_2Bi_{1.99}$

To further optimize the thermoelectric properties of $Ca_{1-x}Yb_xMg_2Bi_2$ and especially the average ZT, we have tried to eliminate the free Bi impurity phase by reducing the initial Bi concentration in $CaMg_2Bi_2$ and $Ca_{0.5}Yb_{0.5}Mg_2Bi_2$. We found when the initial compositions are $CaMg_2Bi_{1.98}$ and $Ca_{0.5}Yb_{0.5}Mg_2Bi_{1.99}$, the peaks on the C_p curves for both cases vanish, as shown in Fig. 3.5b, indicating the disappearance of the impurity phase of Bi. The phase purity can also be confirmed by XRD patterns (Fig. 3.5a), the impurity peaks disappear after reducing the Bi concentration in comparison with Fig. 3.1a.

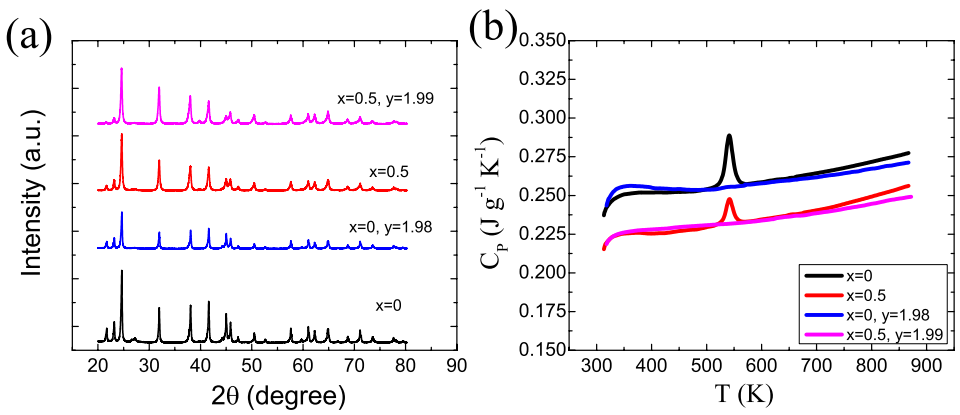

Figure 3.5 XRD patterns (a) and specific heat (b) for for $CaMg_2Bi_2$, $CaMg_2Bi_{1.98}$, $Ca_{0.5}Yb_{0.5}Mg_2Bi_2$, and $Ca_{0.5}Yb_{0.5}Mg_2Bi_{1.99}$.

Fig. 3.6 shows the electronic transport properties for $CaMg_2Bi_2$, $CaMg_2Bi_{1.98}$, $Ca_{0.5}Yb_{0.5}Mg_2Bi_2$, and $Ca_{0.5}Yb_{0.5}Mg_2Bi_{1.99}$. As shown in Fig. 3.6a, the electrical conductivity of Bi-reduced compounds ($CaMg_2Bi_{1.98}$ and $Ca_{0.5}Yb_{0.5}Mg_2Bi_{1.99}$) increases, especially at lower temperature, which could be attributed to the enhanced carrier concentration and almost unchanged Hall mobility. The impurities Bi probably acts as the electron donators in $CaMg_2Bi_2$ and $Ca_{0.5}Yb_{0.5}Mg_2Bi_2$, leading to the reduction in hole carrier concentration. Table 3.2 lists the carrier concentration (n) and Hall mobility (μ) for all four samples. However, $Ca_{0.5}Yb_{0.5}Mg_2Bi_{1.99}$ behaves metallic at all temperature range, which is different from the others, and its electrical conductivity becomes lower than that of $Ca_{0.5}Yb_{0.5}Mg_2Bi_2$ when temperature is above 673 K. The Seebeck coefficient displays a converse trend with the electrical conductivity as shown in Fig. 3.6b. Power factor calculated from the measured electrical conductivity and Seebeck coefficient are displayed in Fig. 3.6c. The power factor of Bi-reduced $CaMg_2Bi_{1.98}$ increases to some degree

compared with that of $CaMg_2Bi_2$, while the power factor of Bi-reduced $Ca_{0.5}Yb_{0.5}Mg_2Bi_{1.99}$ drastically increases and maintains the high value in the entire temperature range.

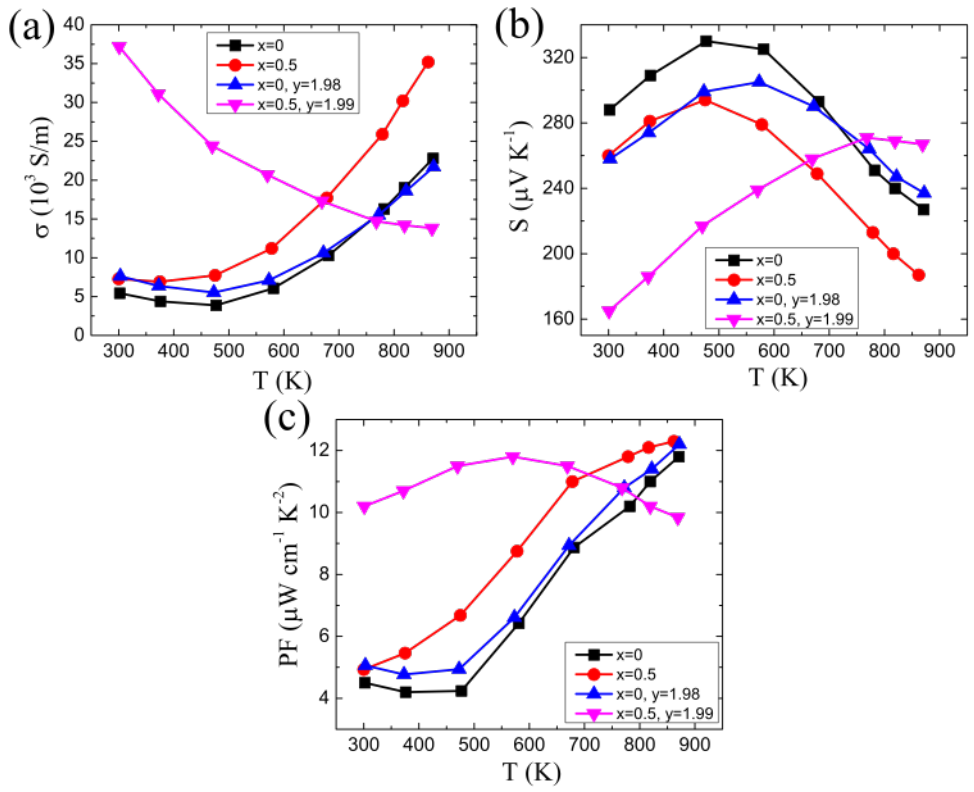

Figure 3.6 Temperature-dependent electronic transport properties of $CaMg_2Bi_2$, $CaMg_2Bi_{1.98}$, $Ca_{0.5}Yb_{0.5}Mg_2Bi_2$, and $Ca_{0.5}Yb_{0.5}Mg_2Bi_{1.99}$: (a) electrical conductivity; (b) Seebeck coefficient; and (c) power factor.

Table 3.2 Room-temperature thermoelectric transport properties of $Ca_{1-x}Yb_xMg_2Bi_y$

$Ca_{1-x}Yb_xMg_2Bi_y$	$x = 0$	$x = 0$, $y = 1.98$	$x = 0.5$	$x = 0.5$, $y = 1.99$
Carrier concentration (10^{18} cm^{-3})	2.38	3.46	3.29	15.00
Hall mobility (cm^2 V^{-1} s^{-1})	143	138	138	155

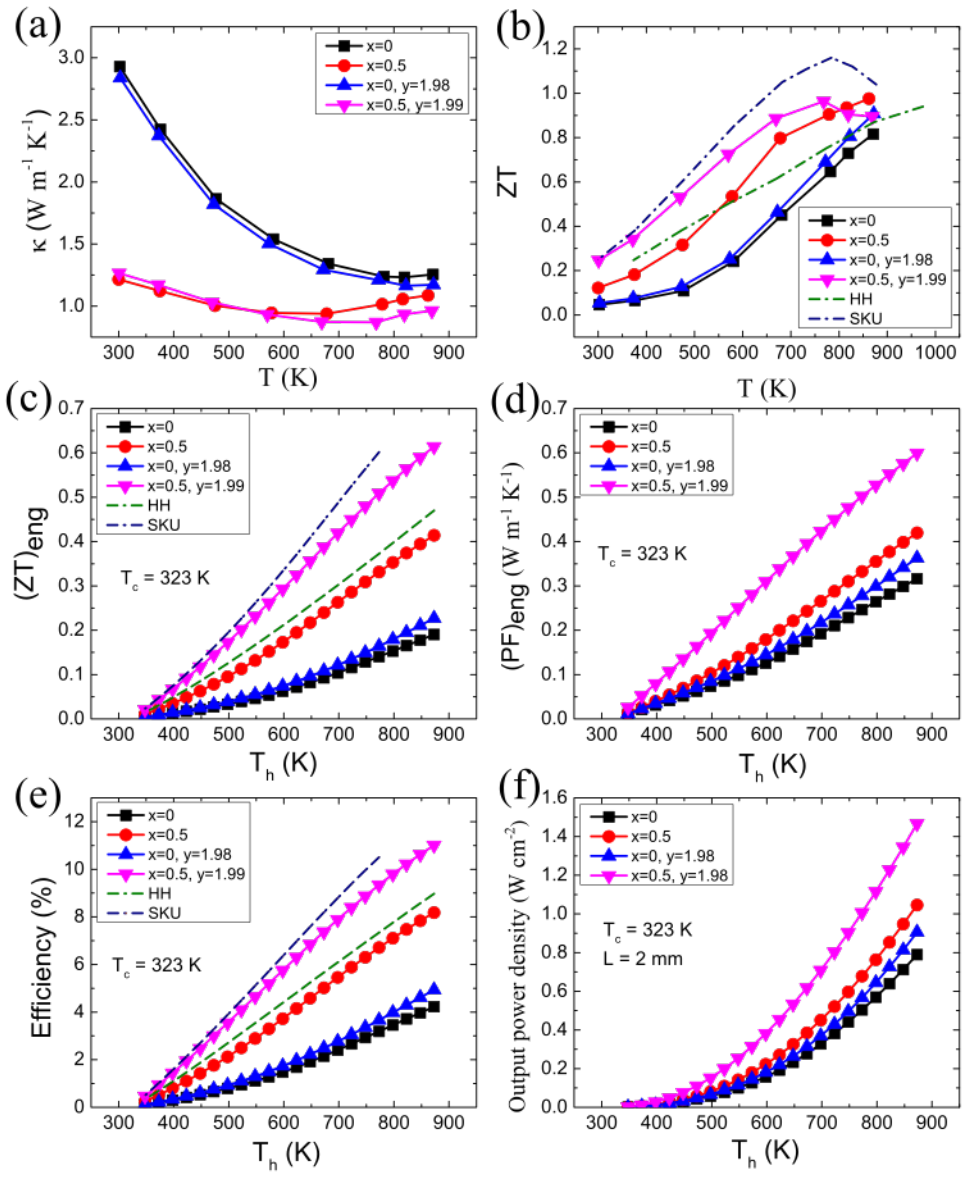

Figure 3.7 Temperature-dependent thermal conductivity (a), *ZT* (b), calculated $(ZT)_{eng}$ (c), and $(PF)_{eng}$ (d), efficiency (e), and output power density (f) for $CaMg_2Bi_2$, $CaMg_2Bi_{1.98}$, $Ca_{0.5}Yb_{0.5}Mg_2Bi_2$, and $Ca_{0.5}Yb_{0.5}Mg_2Bi_{1.99}$. In (b), (c), and (e), the data of p-type Half-Heusler and p-type skutterudite is included for comparison.

The thermal conductivity (Fig. 3.7a) decreases a little at higher temperature for Bi-reduced samples. As a result, *ZT* values, especially the *ZT* values at low temperatures, drastically increase for both Bi-reduced compounds $CaMg_2Bi_{1.98}$ and $Ca_{0.5}Yb_{0.5}Mg_2Bi_{1.99}$ (Fig. 3.7b) although the peak *ZT* values do not differ too much. We have also used the same method to calculate $(ZT)_{eng}$ and $(PF)_{eng}$ dependence of the hot side temperature up to 873 K while the cold side temperature was kept at 323 K. Fig. 3.7c shows the $(ZT)_{eng}$ of $Ca_{0.5}Yb_{0.5}Mg_2Bi_{1.99}$ can reach to 0.6, 50% higher than that of $Ca_{0.5}Yb_{0.5}Mg_2Bi_2$. The $(PF)_{eng}$ of $Ca_{0.5}Yb_{0.5}Mg_2Bi_{1.99}$ also increases 50% due to the relatively higher power factor in the entire temperature range shown in Fig. 3.7d. The calculated efficiency and output power density based on $(ZT)_{eng}$ and $(PF)_{eng}$ are shown in Fig. 3.7e and f. A conversion efficiency about 11.3% and output power density of 1.5 W cm^{-2} are expected for Bi-reduced samples $Ca_{0.5}Yb_{0.5}Mg_2Bi_{1.99}$, which are significantly higher than those of the samples with Bi impurity. The enhancement of thermoelectric performance comes mainly from purifying the phase by reducing Bi concentration. We believe further improvement on *ZT* is highly possible by optimizing the carrier concentration.

We would like to point out that the efficiency about 11% for T_h of 873 K and T_c of 323 K makes this material competitive with half-Heulser and skutterudites for power generation in this temperature range. For comparison, the *ZT* value, $(ZT)_{eng}$ and efficiency of the typical half-Heulser [25] and skutterudites [26] are shown in Fig. 3.7b, c and e, because of their potential in practical applications. The hot side temperature for skutterudites is 773 K since it becomes unstable when T_h is larger than that. In the same temperature range, the efficiency (Fig. 3.7e) of $Ca_{0.5}Yb_{0.5}Mg_2Bi_{1.99}$ is even higher than that

of half-Heusler, just a little lower than that of skutterudites. Such a good efficiency makes this material a potential p-type thermoelectric material to pair with the existing n-type materials.

3.4 High Thermoelectric Performance of Eu-Alloyed AMg_2Bi_2

Reproduced with permission from *Proc Natl Acad Sci USA*, 113, E4125-E4132 (2016).

May *et al*. recently reported on $EuMg_2Bi_2$, which exhibits a resistivity similar to that of $CaMg_2Bi_2$. Such a high resistivity is not reasonable when considering the appearance of the 4*d* and 4*f* electrons in Eu [14]. In our previous study, a significantly enhanced *ZT* value ~1 was obtained for the optimized samples of $Ca_{1-x}Yb_xMg_2Bi_y$ by ball milling and hot pressing, 150% higher than the reported samples by melting and solidification method [27]. Inspired by our investigation on analogous Bi-based Zintl AMg_2Bi_2 (A = Ca, Yb) phases, disordered $(Ca,Yb,Eu)Mg_2Bi_2$ Zintl phases have been studied in the following section.

It has been demonstrated that the base sample $EuMg_2Bi_2$ has the lowest resistivity and achieves much higher *ZT* value ~1. Compared with the reported $EuMg_2Bi_2$ with $ZT < 0.1$, this improvement is significant and mainly attributed to the pure phase and nanostructures achieved by the ball milling and hot pressing method. Further, due to the weakly affected carrier mobility by band engineering and multi strain field fluctuation by

alloy effects on A-site (Ca, Yb, and Eu), a significantly enhanced thermoelectric figure of merit, ZT ~1.3 is achieved.

3.4.1 $EuMg_2Bi_2$, $Eu_{0.5}Yb_{0.5}Mg_2Bi_2$, and $Eu_{0.5}Ca_{0.5}Mg_2Bi_2$

$EuMg_2Bi_2$, $Eu_{0.5}Yb_{0.5}Mg_2Bi_2$, and $Eu_{0.5}Ca_{0.5}Mg_2Bi_2$ were fabricated by mechanical alloying and hot pressing, and confirmed to be phase pure within the XRD detection limit (Fig. 3.8). To assess the TE performance of these samples, the electrical resistivity, Seebeck coefficient, and thermal conductivity were measured from 300 to 873 K, as shown in Fig. 3.9. Hall-effect measurements were performed to aid in the analysis of these measurements (Table 3.3). For comparison, the TE properties of the three base compositions $CaMg_2Bi_2$, $YbMg_2Bi_2$, and $EuMg_2Bi_2$ are shown in the insets of Fig. 3.9.

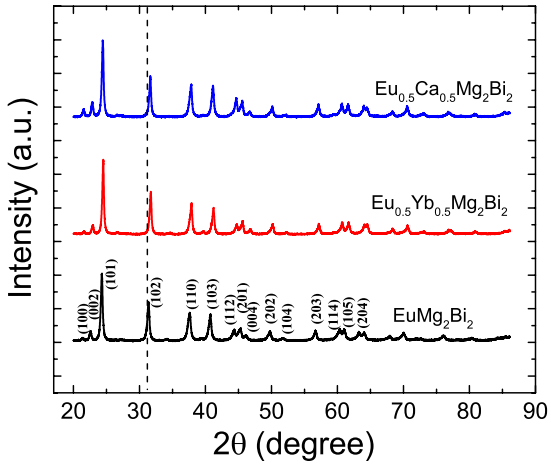

Figure 3.8 XRD patterns of AMg_2Bi_2 (A = Eu, $Eu_{0.5}Ca_{0.5}$, $Eu_{0.5}Yb_{0.5}$).

Fig. 3.9a illustrates the electrical resistivity as a function of temperature. All

samples seem to follow ρ vs. $T^{1.5}$, indicating that the carrier transport is dominated by acoustic phonon scattering before the intrinsic excitation. $EuMg_2Bi_2$ and $Eu_{0.5}Yb_{0.5}Mg_2Bi_2$ exhibit very similar resistivity, while $Eu_{0.5}Ca_{0.5}Mg_2Bi_2$ shows higher resistivity, largely because of its decreased carrier concentration and mobility. The carrier concentration increases by almost one order of magnitude from 2.38 $\cdot 10^{18}$ cm^{-3} for $CaMg_2Bi_2$ and 7.2 $\cdot 10^{18}$ cm^{-3} for $YbMg_2Bi_2$ to 4.36 $\cdot 10^{19}$ cm^{-3} for $EuMg_2Bi_2$. Therefore, at room temperature, $EuMg_2Bi_2$ shows a much lower resistivity ~7 μΩ m than that of $CaMg_2Bi_2$ (~184 μΩ m) and $YbMg_2Bi_2$ (~72.6 μΩ m). As expected, the lower Seebeck coefficient of $EuMg_2Bi_2$ is achieved due to the enhanced carrier concentration and mobility. Specifically, at room temperature, S increases from ~100 μV K^{-1} for $EuMg_2Bi_2$ to ~209 μV K^{-1} for $YbMg_2Bi_2$ and ~288 μV K^{-1} for $CaMg_2Bi_2$. As shown in Fig. 3.9b, it can be observed that the higher carrier concentration in $EuMg_2Bi_2$ effectively suppresses the bipolar effect, while the inset clearly shows the bipolar effect occurring in $CaMg_2Bi_2$ and $YbMg_2Bi_2$ at very low temperatures because of the low carrier concentration. Among all the samples, $EuMg_2Bi_2$ exhibits the highest average power factor, nearly three times that of $CaMg_2Bi_2$ and $YbMg_2Bi_2$ at room temperature (Fig. 3.9c).

Fig. 3.9a illustrates the electrical resistivity as a function of temperature. All samples seem to follow ρ vs. $T^{1.5}$, indicating that the carrier transport is dominated by acoustic phonon scattering before the intrinsic excitation. $EuMg_2Bi_2$ and $Eu_{0.5}Yb_{0.5}Mg_2Bi_2$ exhibit very similar resistivity, while $Eu_{0.5}Ca_{0.5}Mg_2Bi_2$ shows higher resistivity, largely because of its decreased carrier concentration and mobility. The carrier concentration increases by almost one order of magnitude from 2.38 $\cdot 10^{18}$ cm^{-3} for $CaMg_2Bi_2$ and 7.2

$\cdot 10^{18}$ cm^{-3} for $YbMg_2Bi_2$ to 4.36 $\cdot 10^{19}$ cm^{-3} for $EuMg_2Bi_2$. Therefore, at room temperature, $EuMg_2Bi_2$ shows a much lower resistivity ~7 μΩ m than that of $CaMg_2Bi_2$ (~184 μΩ m) and $YbMg_2Bi_2$ (~72.6 μΩ m). As expected, the lower Seebeck coefficient of $EuMg_2Bi_2$ is achieved due to the enhanced carrier concentration and mobility. Specifically, at room temperature, S increases from ~100 μV K^{-1} for $EuMg_2Bi_2$ to ~209 μV K^{-1} for $YbMg_2Bi_2$ and ~288 μV K^{-1} for $CaMg_2Bi_2$. As shown in Fig. 3.9b, it can be observed that the higher carrier concentration in $EuMg_2Bi_2$ effectively suppresses the bipolar effect, while the inset clearly shows the bipolar effect occurring in $CaMg_2Bi_2$ and $YbMg_2Bi_2$ at very low temperatures because of the low carrier concentration. Among all the samples, $EuMg_2Bi_2$ exhibits the highest average power factor, nearly three times that of $CaMg_2Bi_2$ and $YbMg_2Bi_2$ at room temperature (Fig. 3.9c).

The temperature dependence of thermal conductivity and that of lattice thermal conductivity are shown in Fig. 3.9d and 3.9e, respectively. $Eu_{0.5}Ca_{0.5}Mg_2Bi_2$ and $Eu_{0.5}Yb_{0.5}Mg_2Bi_2$ show much lower thermal conductivity than that of $EuMg_2Bi_2$ due to the alloy effect. The total thermal conductivity of $Eu_{0.5}Ca_{0.5}Mg_2Bi_2$ is even lower than that of $Eu_{0.5}Yb_{0.5}Mg_2Bi_2$ mainly because of the lower electronic contribution κ_e, estimated using the Wiedemann−Franz relationship ($\kappa_e = LT/\rho$), where L is the Lorenz number approximated using a single parabolic band model, which leads to similar lattice thermal conductivity ($\kappa_{Lat} = \kappa - \kappa_e$) of $Eu_{0.5}Ca_{0.5}Mg_2Bi_2$ with $Eu_{0.5}Yb_{0.5}Mg_2Bi_2$. The figure of merit is shown in Fig. 3.9f. As compared to the reported ZT ~0.1 in $EuMg_2Bi_2$ by the melting and solidification method, our $EuMg_2Bi_2$ sample by the ball milling and hot pressing method possesses a much improved ZT ~1. For both the alloyed $Eu_{0.5}Yb_{0.5}Mg_2Bi_2$ and

$Eu_{0.5}Ca_{0.5}Mg_2Bi_2$, the average *ZT*s over the whole temperature range are higher than that of $EuMg_2Bi_2$ at temperature below 773 K.

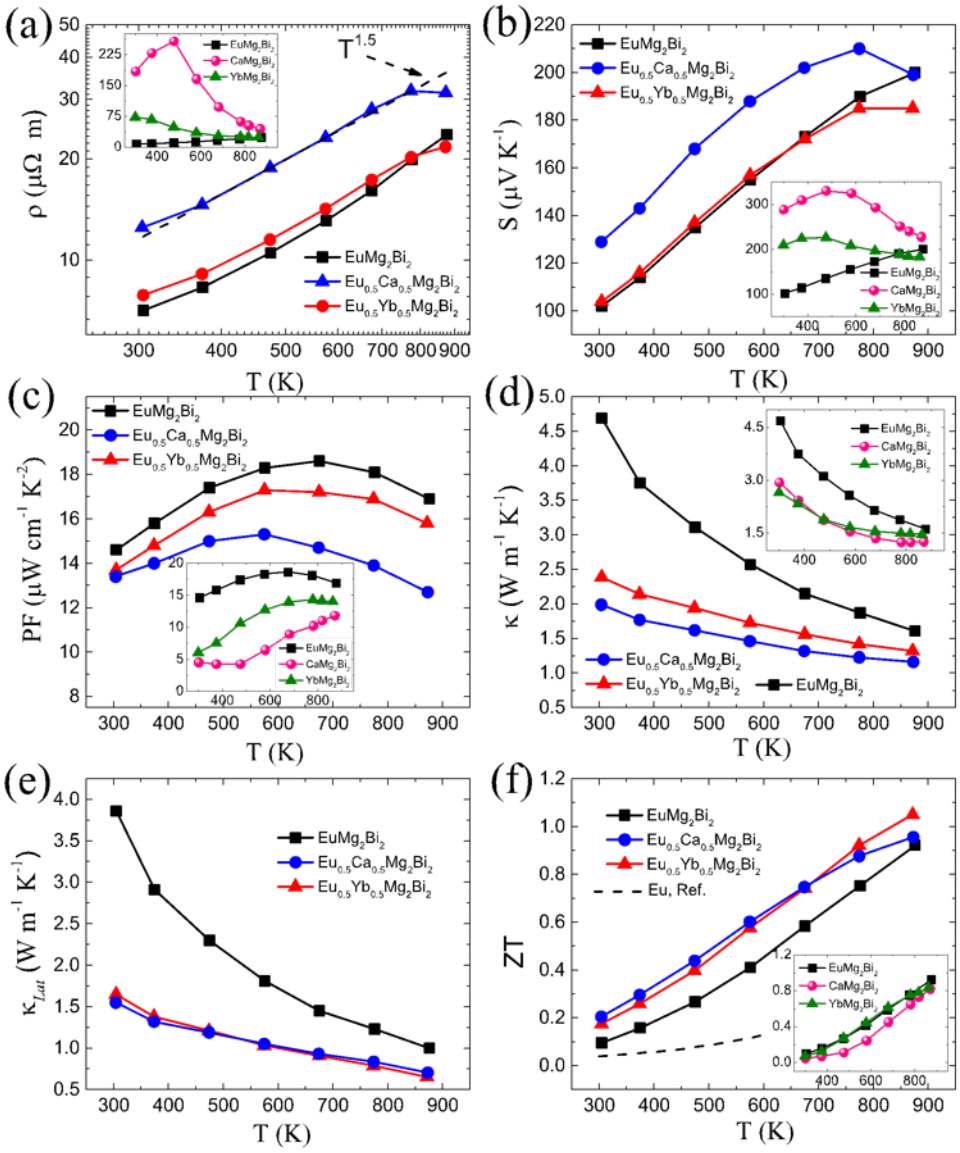

Figure 3.9 Temperature-dependent TE properties for AMg_2Bi_2 (A = Eu, $Eu_{0.5}Ca_{0.5}$, $Eu_{0.5}Yb_{0.5}$). (a) Electrical resistivity, (b) Seebeck coefficient, (c) power factor, (d) total thermal conductivity, (e) lattice thermal conductivity, and (f) *ZT* values. The insets separately show the respective TE properties for the three base compositions AMg_2Bi_2 (A = Ca, Yb, Eu).

Table 3.3 Electric transport properties of AMg_2Bi_2 (A = Eu, $Eu_{0.5}Ca_{0.5}$, $Eu_{0.5}Yb_{0.5}$).

AMg_2Bi_2	Eu	$Eu_{0.5}Ca_{0.5}$	$Eu_{0.5}Yb_{0.5}$
Carrier concentration (10^{19} cm^{-3})	4.36	3.14	3.98
Hall mobility (cm^2 V^{-1} s^{-1})	202	159	200
Effective mass (m_e)	0.71	0.78	0.68

3.4.2 Electronic and Lattice Dynamics Calculations for Three Base Compounds AMg_2Bi_2 (A = Ca, Yb, Eu)

To better understand the transport behavior of the AMg_2Bi_2 family, density functional theory was first used to investigate the crystal and band structures, charge distribution and chemical bonding for the three base compounds AMg_2Bi_2 (A = Ca, Yb, Eu).

The calculated crystal structures of the three base compounds are listed in Table 3.4. The larger Eu^{2+} ion expands the structure and results in a larger geometric anisotropy of the crystal, as observed from XRD patterns with left shifting (Fig. 3.8). The Zintl compounds crystallizing in the $CaAl_2Si_2$ structure have been demonstrated to be p-type by both the first principle calculation and experiments [10,28], while the n-type compound has barely been found.

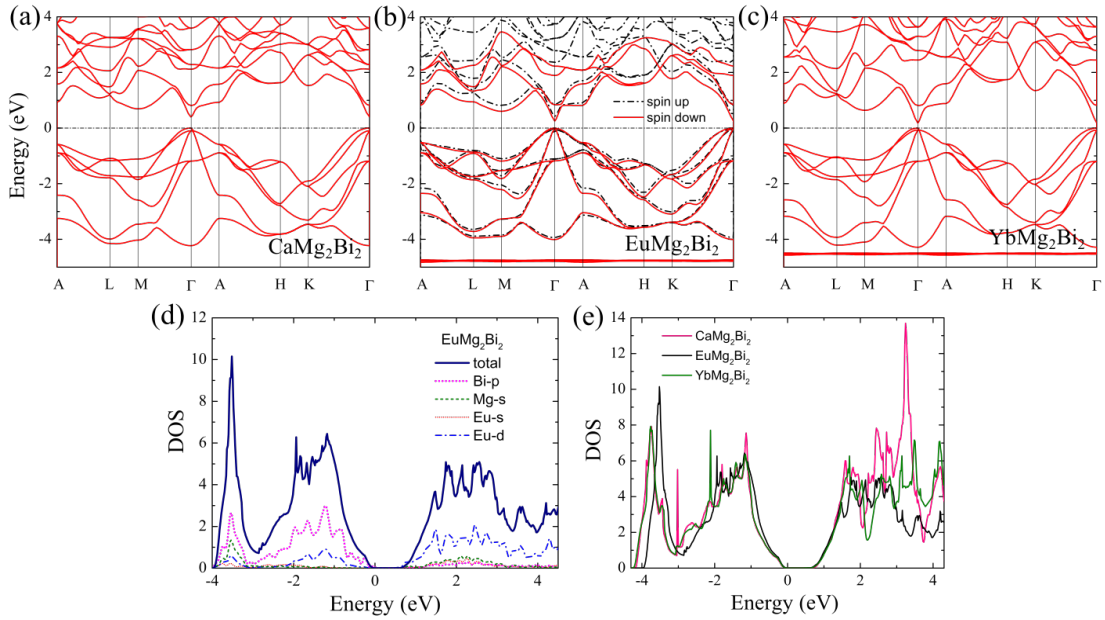

Figure 3.10 DFT calculations. Band structures of (a) $CaMg_2Bi_2$, (b) $EuMg_2Bi_2$, and (c) $YbMg_2Bi_2$; (d) total and projected DOS of $EuMg_2Bi_2$; and (e) DOS of three base compounds.

Table 3.4 Sound velocity and Debye temperature of AMg_2Bi_2.

	c-axis Longitudinal(m/s)	c-axis Transverse (m/s)	a-axis longitudinal(m/s)	a-axis transverse (m/s)	a-axis Transverse (m/s)	Debye Temperature (K)
$CaMg_2Bi_2$	3057	2658	3133	2146	1817	248
$EuMg_2Bi_2$	2870	1646	2796	2186	1640	223
$YbMg_2Bi_2$	2500	1420	2680	1748	1200	222

The DFT calculated band structures of the three base compounds are shown in Fig. 3.10a-3c, proving that the Bi-based AMg_2Bi_2 Zintl phases are also intrinsically p-type. Clearly, both light- and heavy-hole bands exist near the top of the zone center. The direct band gap (E_g) energy for $CaMg_2Bi_2$ is estimated to be 0.4 eV, smaller than the previously

reported value of 0.7 eV estimated by the TB-mBJ method [13]. FTIR specular reflectance measurement plus Kramers-Kronig analysis shows the band gap for $CaMg_2Bi_2$ to be around 0.42 (Supplementary Fig. 2) and is in agreement with our DFT results. Due to the 4*f* electrons, E_g is observed to be 0.25 eV for $EuMg_2Bi_2$ and 0.18 eV for $YbMg_2Bi_2$.

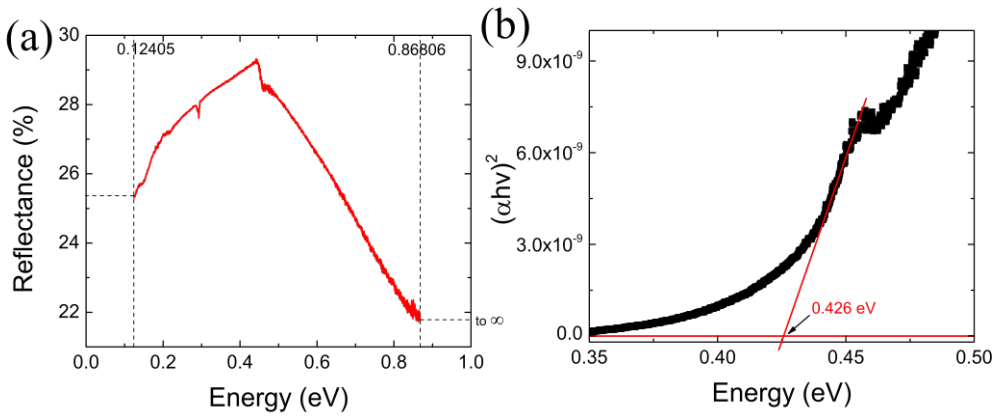

Figure 3.11 Band-gap measurement for base compound $CaMg_2Bi_2$. (a) FTIR specular-reflectance result with incident angle of 25 degrees; (b) band gap ~0.426 eV by using Kramers-Kronig method.

Fig. 3.10d shows the total and projected density of states (DOS) of $EuMg_2Bi_2$. It is clear that the Bi-p states dominate the valence bands. Overlaps of Mg-s and Bi-p states in the valence region (-4eV) are also observed, indicating the hybridization between these states. This hybridization supports the polyanionic $(Mg_2Bi_2)^{-2}$ Zintl nature of these materials.

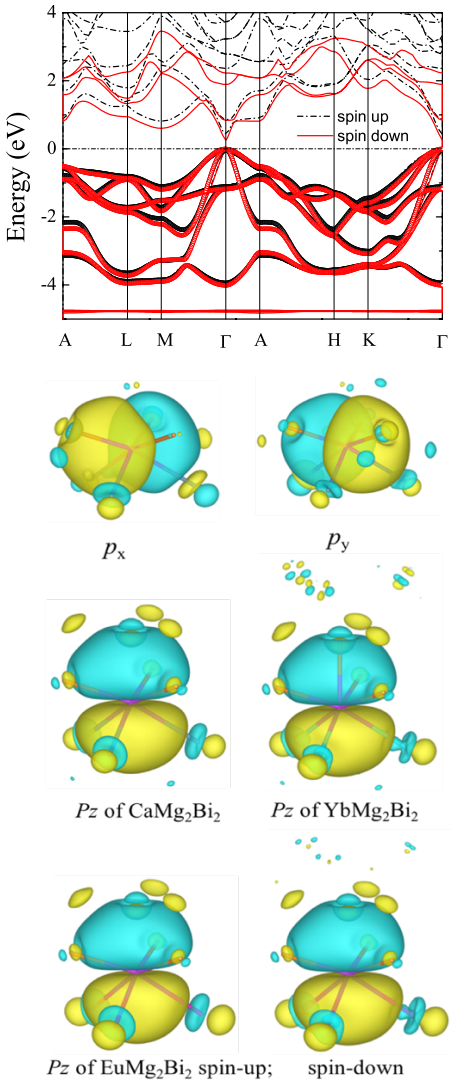

Figure 3.12 Band structure of $EuMg_2Bi_2$ and corresponding valence MLWFs. Top: Circles indicate a six-dimensional manifold that has been disentangled from the full band structure (solid lines). Bottom: Bi-atom-centered *p*-like MLWFs (p_x, p_y, p_z) obtained from this manifold. Isosurfaces of different color correspond to two opposite values for the amplitudes of the real-valued MLWFs.

The DOS of all compounds is shown in Fig. 3.10e. The $EuMg_2Bi_2$ crystal possesses the largest geometric anisotropy, but a nearly zero crystal field splitting energy (Δ_{cr}) (Table 3.4). The small Δ_{cr} results in the higher band degeneracy near the Fermi level, which is always favorable for the electrical transport properties of thermoelectric materials [29];

this is consistent with the recent report on the selection criterion $-0.06 < \Delta_{cr} < 0.06$ with band gap Eg < 1.5eV for promising Zintl TE candidates [30]. Moreover, to obtain an insightful picture of the chemical bonding, we generated the maximally localized Wannier functions (MLWFs) of all three compounds. It can be observed that the top six valence bands can be well represented by the six p-like MLWFs centered on two Bi atoms (Fig. 3.12). Additionally, strong hybridizations are found between Bi and Eu/Yb, explaining the small band gap and large hole mobility in $EuMg_2Bi_2$ and $YbMg_2Bi_2$.

In addition to electronic calculations, to further understand the thermal transport, the phonon dispersions and densities-of-states were calculated based on the density functional perturbation theory (DFPT).

The phonon band structures of $CaMg_2Bi_2$, $EuMg_2Bi_2$, and $YbMg_2Bi_2$ are presented in Fig. 3.13. We see that: (1) The phonon frequencies of all pure compounds are relatively low. For instance, the three acoustic modes of each pure compound are all comprised of low frequencies of 50 cm^{-1} (6 meV) or less, above which they intersect optical branches. Meanwhile, the maximum optical mode frequency is only 250 cm^{-1} (31 meV). These low phonon frequencies are favorable for the thermoelectric transport properties. (2) Significant dispersion of the optical modes is observed in all of the three base compounds. Therefore, unlike other thermoelectric materials with complex crystal structures, the optical modes of the current compounds possess nonzero group velocities and contribute significantly to the heat transport. Thus, the usual phonon transport model based on the Debye approximation may require consideration in these compounds. (3) The low frequency parts of the phonon

spectra become more depressed with increased A-site mass. The $CaMg_2Bi_2$ compound possesses three optical modes near 130 cm^{-1}, while these optical modes move down and intersect the acoustic models in $EuMg_2Bi_2$ and $YbMg_2Bi_2$ compounds. Therefore, lower acoustic phonon group velocities and stronger phonon-phonon scattering can be expected in the latter two compounds. Table 3.5 lists the calculated sound velocity and Debye temperature for three pure compounds. The calculated Debye temperatures for three pure compounds are very close to the experimental values measured by the specific heat method (244 K for $CaMg_2Bi_2$, 211 K for $EuMg_2Bi_2$, and 207 K for $YbMg_2Bi_2$) [13]. The A-site mass dependence of the sound velocity is also clearly seen. The sound velocities of AMg_2Bi_2 compounds are smaller than that of the AMg_2Sb_2 compound, as reported by Singh *et al*. [31]. Furthermore, these sound velocities of AMg_2Bi_2 compounds are comparable to those of the excellent thermoelectrics, such as Bi_2Te_3 and PbTe, for which longitudinal sound speeds are typically around 3 km/s and transverse sound speeds around 2 km/s [32,33], which suggests that AMg_2Bi_2 compounds would be good TE materials.

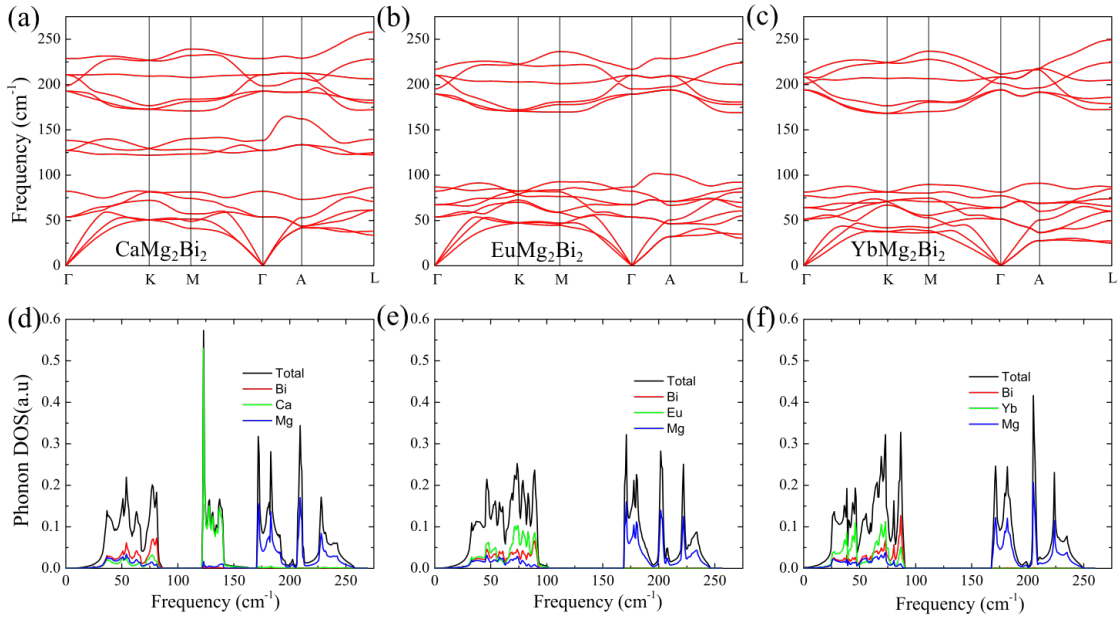

Figure 3.13 Calculated phonon dispersions (in cm-1) for (a) $CaMg_2Bi_2$, (b) $EuMg_2Bi_2$, and (c) $YbMg_2Bi_2$ along high symmetry directions; Calculated phonon densities of states for (d) $CaMg_2Bi_2$, (e) $EuMg_2Bi_2$, and (f) $YbMg_2Bi_2$.

Figs. 3.13d-f show the calculated phonon densities-of-states (PDOS), including partial contributions from the Ca/Eu/Yb, Mg, and Bi sites. For $CaMg_2Bi_2$, the total DOS breaks up into three separate regions: Bi-dominated below ~100 cm^{-1}, primarily Ca between 120 and 150 cm^{-1}, and primarily Mg between ~170 and 250 cm^{-1}. On the other hand, the total PDOS of $EuMg_2Bi_2$/$YbMg_2Bi_2$ breaks up into two separate regions: Eu/Yb-dominated below approximately 100 cm^{-1}, and primarily Mg between ~170 and 250 cm^{-1}. The Eu/Yb domination below 100 cm^{-1} cannot be explained by the increased mass only, but also by the strong *f*-hybridization of the nearest Eu/Yb atoms, as indicated by the maximally localized Wannier functions.

3.4.3 $(Eu_{0.5}Yb_{0.5})_{1-x}Ca_xMg_2Bi_2$

Because of the similar electronic properties between $EuMg_2Bi_2$ and $Eu_{0.5}Yb_{0.5}Mg_2Bi_2$ and the lower thermal conductivity in $Eu_{0.5}Ca_{0.5}Mg_2Bi_2$, Ca is introduced to replace some of the Eu and Yb in $Eu_{0.5}Yb_{0.5}Mg_2Bi_2$ while the ratio of Eu and Yb is kept the same. Fig. 3.14 shows the XRD pattern of $(Eu_{0.5}Yb_{0.5})_{1-x}Ca_xMg_2Bi_2$ with x = 0.4, 0.5, 0.6, and 0.7. The peaks can be well indexed according to the reported structure of $CaAl_2Si_2$. When Ca is introduced, a small impurity phase Bi is observed, the same as in our previous report on $Yb_xCa_{1-x}Mg_2Bi_2$ [27].

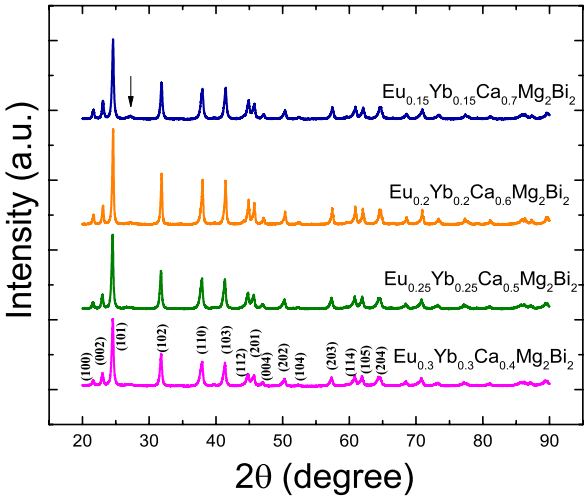

Figure 3.14 XRD pattern for $(Eu_{0.5}Yb_{0.5})_{1-x}Ca_xMg_2Bi_2$.

Electrical transport. The electrical transport properties as a function of temperature are illustrated in Fig. 3.15 for $(Eu_{0.5}Yb_{0.5})_{1-x}Ca_xMg_2Bi_2$ with x = 0.4, 0.5, 0.6, and 0.7. Based on our DFT calculation, the band gaps for ordered $CaMg_2Bi_2$, $YbMg_2Bi_2$, and $EuMg_2Bi_2$ are 0.40, 0.18, and 0.25 eV, respectively. Adjusting the ratios of Ca/Yb/Eu

in $(Eu_{0.5}Yb_{0.5})_{1-x}Ca_xMg_2Bi_2$ actually changes both the band gap energy and the relative positions of bands, directly affecting their electrical properties. The temperature-dependent electrical resistivity is shown in Fig. 3.15a. The resistivity for all samples shows a similar trend of increasing with temperature following ρ vs. $T^{1.5}$ as for AMg_2Bi_2 (A = Eu, $Eu_{0.5}Ca_{0.5}$, $Eu_{0.5}Yb_{0.5}$) (Fig. 3.9a). With increasing Ca concentration, the electrical resistivity gradually increases, mainly due to the reduction of carrier concentration. Consistent with the tendency of electrical resistivity, the Seebeck coefficients increase with increasing Ca concentration, as shown in Fig. 3.15b. The Seebeck coefficients of all samples exhibit peak values, the typical characteristic of the bipolar effect. With increasing concentrations of Eu/Yb, the increased carrier concentrations by reduced band gap causes the peaks to shift to higher temperatures. The relationship between Seebeck coefficient and carrier concentration at room temperature is plotted in Fig. 3.15c. Even though DFT calculation has demonstrated that there are three bands at the valence band edge that are degenerate at Γ point, the single parabolic band model with a single combined effective mass has been successfully applied in Zintl AZn_2Sb_2 (A = Sr, Ca, Yb, Eu) [10]. Similarly, here we also applied the single parabolic band model with the assumption of acoustic phonon scattering; the dashed line is the theoretical Pisarenko line with $m^* = 0.7m_e$. All of the experimental data falls well onto the calculated line. This good agreement between the single-band model and the experimental data demonstrates that the different compositions in A-site have almost no influence on the valence band structure at 300 K, confirmed by the DOS calculation discussed above. Fig. 3.15d shows the power factor, which slightly increases with Eu/Yb concentration.

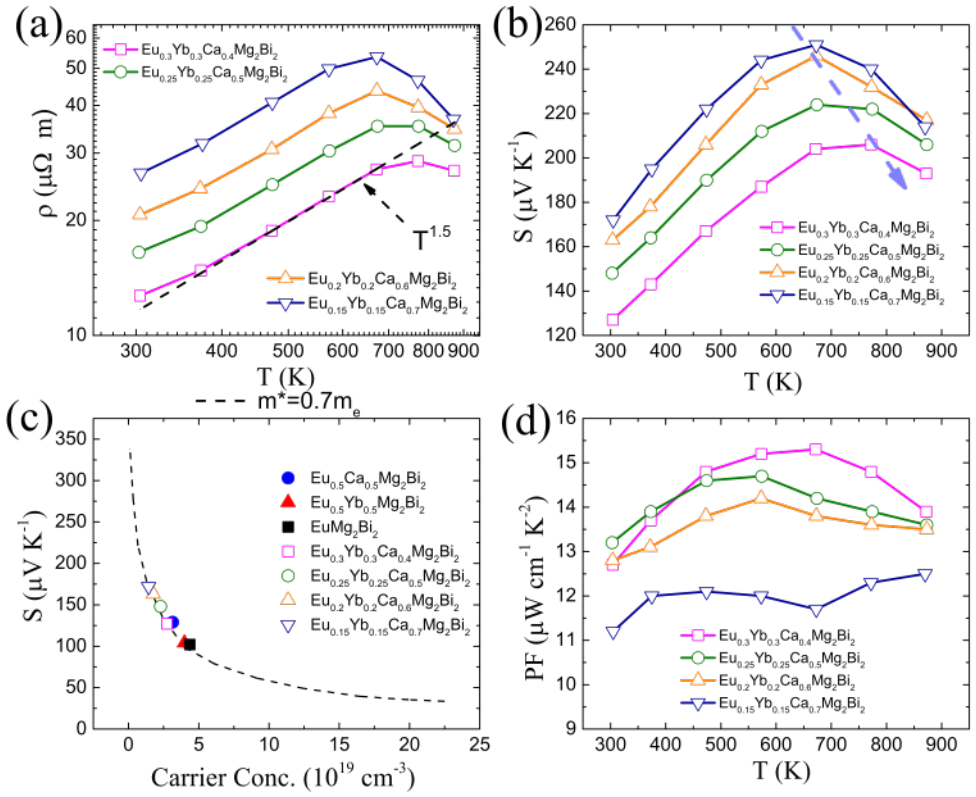

Figure 3.15 Temperature-dependent electrical transport properties for $(Eu_{0.5}Yb_{0.5})_{1-x}Ca_xMg_2Bi_2$. (a) Electrical resistivity, (b) Seebeck coefficient, and (d) power factor. (c) The Pisarenko plot with m* = 0.7 m_e at 300 K for all samples.

Band Engineering of (Ca,Eu,Yb)Mg_2Bi_2: weakly affected VB for high mobility and adjusted CB by alloying. Generally speaking, substituting atoms disturbs the lattice, making perfectly coherent electron waves impossible. Instead, the electrons are scattered by such atoms, resulting in the reduction of carrier mobility. This phenomenon is therefore called chemical disorder scattering, which is not beneficial for electronic performance. For example, the mobility drops by more than 30% in n-type $(PbTe)_{1-x}(PbSe)_x$ solid solutions due to chemical disorder scattering [34]. However, as shown in Table 3.6, the carrier mobility of $(Eu_{0.5}Yb_{0.5})_{1-x}Ca_xMg_2Bi_2$ is not reduced much due to chemical disorder

scattering.

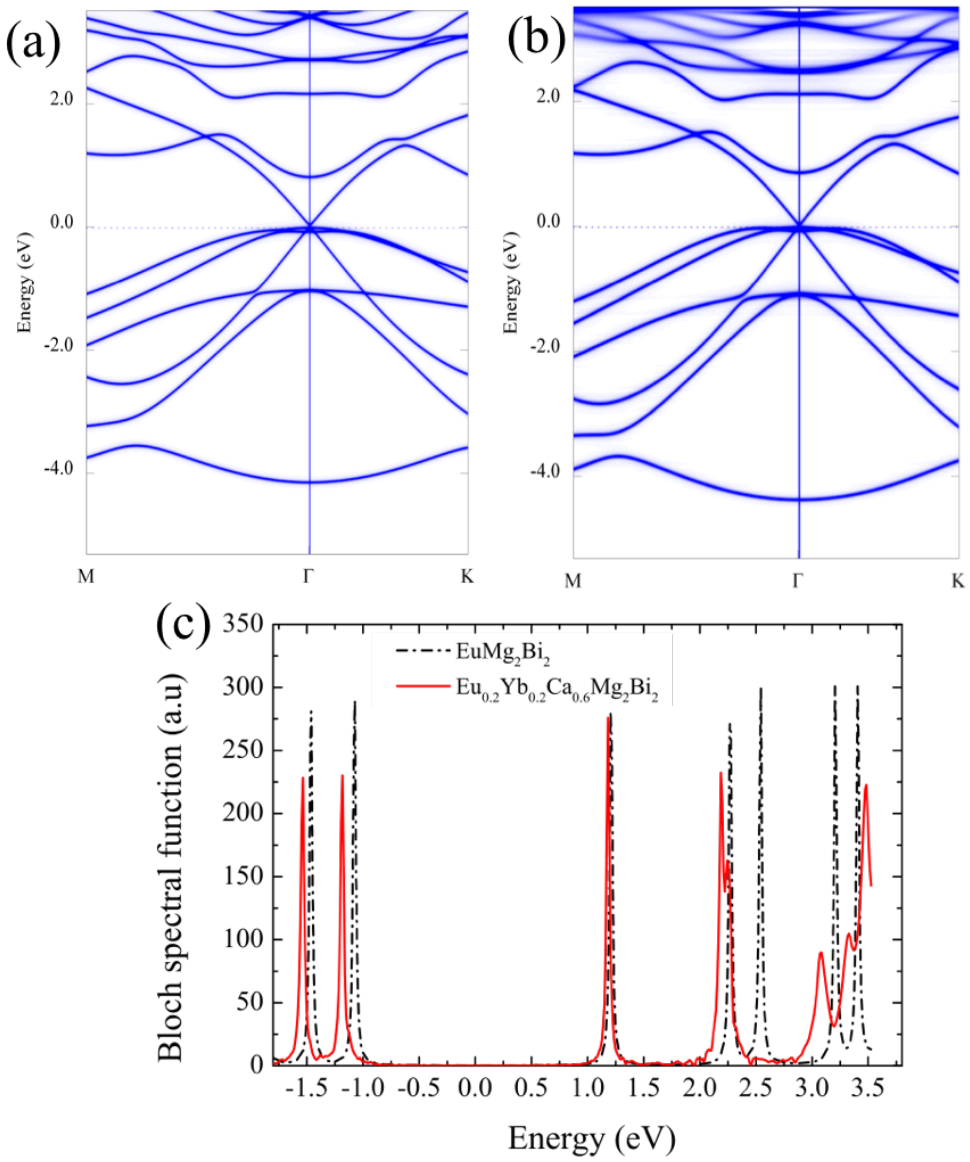

Figure 3.16 Bloch spectral functions of substituted $Eu_{0.2}Yb_{0.2}Ca_{0.6}Mg_2Bi_2$. Compared are the Bloch spectral functions of pure EuMg2Bi2 (a), substituted $Eu_{0.2}Yb_{0.2}Ca_{0.6}Mg_2Bi_2$ (b) for the high-symmetry directions M-Γ-K, and (c) the Bloch spectral functions of two compounds projected on the M-point.

The carrier mobility is inversely proportional to the product of effective mass and scattering rate. Our DFT calculations reveal that both the effective mass and scattering rate are nearly unaffected by the Yb/Ca substitution. The comparison of the electronic structure of the optimized $Eu_{0.2}Yb_{0.2}Ca_{0.6}Mg_2Bi_2$ with $EuMg_2Bi_2$ is demonstrated in Figs. 3.16a-b using the Bloch spectral function calculated by the KKR-CPA method. The lifetime $\tau \propto (\Delta E)^{-1}$ of chemical disorder scattering is introduced here, inversely proportional to the energy width of the states. By comparing the different states of the base and substituted compounds, it is seen that the hole states are much less influenced than the electron states in the whole band structure. This is consistent with the nearly unchanged effective masses (Table 3.6). On the other hand, the width of the Bloch spectral function projected at M point is compared in Fig. 3.16c. The inspection of the Bloch spectral function also reveals that the broadening, and thus the relaxation times τ, is only significant in the conducting bands. This is also beneficial in maintaining the high carrier mobility in the disordered structures [34].

Table 3.5 Electric transport properties for $(Eu_{0.5}Yb_{0.5})_{1-x}Ca_xMg_2Bi_2$ with x = 0.4, 0.5, 0.6, and 0.7.

$(Eu_{0.5}Yb_{0.5})_{1-x}Ca_xMg_2Bi_2$	x = 0.4	x = 0.5	x = 0.6	x = 0.7
Carrier concentration (10^{19} cm^{-3})	2.73	2.28	1.77	1.43
Hall mobility (cm^2 V^{-1} s^{-1})	180	166	171	164
Effective mass (m_e)	0.70	0.77	0.77	0.72

Reduced thermal conductivity through nanostructure, strain, and dislocation. Thermal conductivity is calculated as the product of density, specific heat (Fig. 3.17a), and thermal diffusivity (Fig. 3.17b). The peak around 543 K observed (Fig. 3.17a) indicates there is a phase transition. This is mainly because of the existence of Bi as the impurity phase, as observed in Fig. 3.14. The melting point of Bi is 544 K, consistent with the peak observed in specific heat measurement. The same phenomenon has been demonstrated in the study of $Ca_{1-x}Yb_xMg_2Bi_2$.

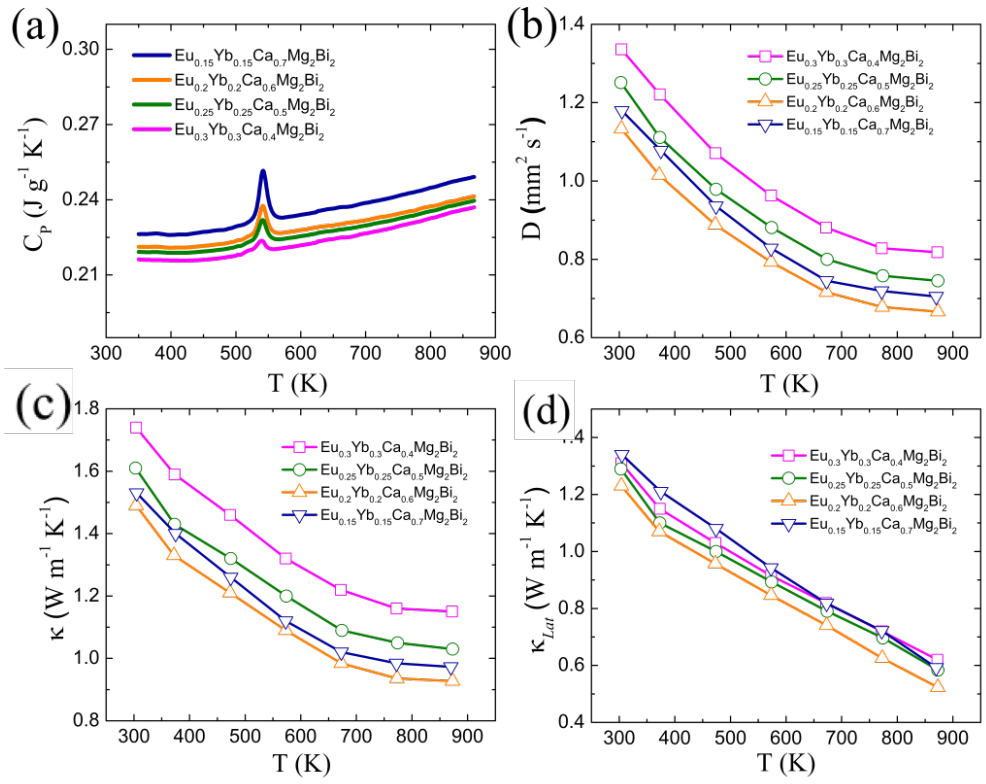

Figure 3.17 Temperature-dependent thermal conductivity for $(Eu_{0.5}Yb_{0.5})_{1-x}Ca_xMg_2Bi_2$. (a) Specific heat, (b) Thermal diffusivity, (c) Total thermal conductivity, and (d) lattice thermal conductivity.

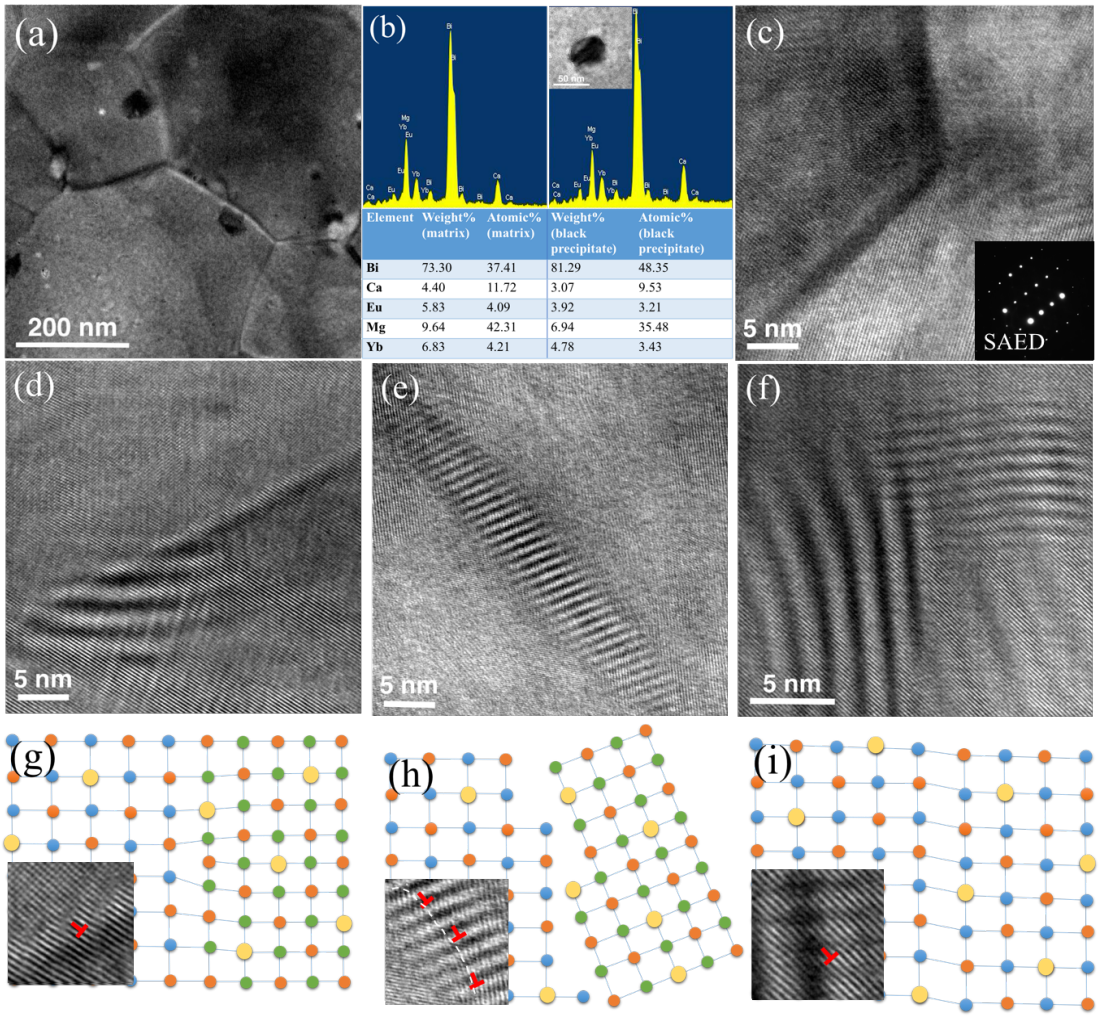

Figure 3.18 Typical microstructures for $Eu_{0.2}Yb_{0.2}Ca_{0.6}Mg_2Bi_2$. (a) Medium-magnification TEM image showing mesoscale grains with black precipitates; (b) EDS spectra for matrix (left) and precipitate (right) with elemental composition data, (c) HRTEM image of grain boundary showing good crystallization; inset: the selected area electron diffraction pattern; (d) semi-coherent strain by misfit dislocation around the grain boundary; (e) incoherent interaction near the grain boundary; (f) coherent strain inside the grain; (g), (h), and (i) are schematic diagrams illustrating three possible types of semi-coherent, incoherent, and coherent interactions, respectively with inset magnification of one segment corresponding to Figs. 3.18d-f, respectively (larger yellow circles represent dopants).

Fig. 3.17c shows the temperature dependence of the total thermal conductivity κ for all $(Eu_{0.5}Yb_{0.5})_{1-x}Ca_xMg_2Bi_2$ samples. At room temperature, the κ of base compounds

AMg_2Bi_2 (A = Eu, Yb, Ca), shown in Fig. 3.9d, is ~3 W m^{-1} K^{-1}, and is dramatically reduced to 1.5 W m^{-1} K^{-1} in the $Eu_{0.2}Yb_{0.2}Ca_{0.6}Mg_2Bi_2$ sample. For all alloyed samples in Fig. 3.17c, with increasing Ca concentration, the thermal conductivity first decreases, reaching the lowest point at x = 0.6, and then increases. By directly subtracting the electronic contribution from the total thermal conductivity, the lattice thermal conductivities (κ_{Lat}) were obtained and are shown in Fig. 3.17d. Specifically, the lowest lattice thermal conductivity decreases to 0.5 W m^{-1} K^{-1} at 873 K in the sample with x = 0.6. Apparently, the alloying effect contributes much to the reduction in lattice thermal conductivity, which would significantly enhance the efficiency due to the weakly affected carrier mobility and the similar effective mass.

The microstructure of the optimized $Eu_{0.2}Yb_{0.2}Ca_{0.6}Mg_2Bi_2$ sample is investigated by transmission electron microscopy (TEM). The presence of nanoscale grains around 200-500 nm is evident in Fig. 3.18a. The black nano precipitates around 5-50 nm can also be observed inside grains or near boundaries. Elemental analysis by energy dispersion X-ray spectroscopy (EDS) indicates Bi concentration is higher in the precipitates (Fig. 3.18b), consistent with the Bi peaks shown in XRD patterns and specific heat curve. Fig. 3.18c shows the clean grain boundaries by high resolution TEM and crystalline grains of the sample. Moreover, a number of different defect strains were observed in the samples, as shown in Fig. 3.18d-f, which might be evidence of point defects in alloyed structures.

The strain is defined as the measurement of the relative displacement of atoms/ions

from a reference configuration. Normally, there are three types of precipitate-matrix or matrix-matrix interfaces: coherent (elastic strain), incoherent, and semi-coherent (plastic strain) (shown in Figs. 3.18g-i) [35]. The coherent elastic strain and semi-coherent plastic strain are common. In most cases, the incoherent interface would seldom involve strain field due to the minimal interaction between the phases. The three types of interactions can largely affect the phonon scattering, and the detailed analysis is shown in Figs. 3.18d-i. In Fig. 3.18d, the semi-coherent strain caused by misfit dislocations is observed near the grain boundary with the corresponding schematic representation plotted in Fig. 3.18g. The inset magnification of one segment of Fig. 3.18d clearly indicates several dislocations. Near the grain boundary shown in Fig. 3.18e, another type of incoherent interaction is also observed even possibly with strain fields appearing. The enlarged image is displayed in Fig. 3.18h with the corresponding schematic representation. The last type of interaction of the elastic strain is observed inside the grains mainly due to the large alloy concentration as shown in Fig. 3.18f. Most of the strain field fluctuations observed in Fig. 3.18 are likely to be caused by the Ca, Yb, and Eu disorder in the lattice because of the mass and size differences, which could significantly reduce the lattice thermal conductivity.

Inspired by the dramatically reduced disorders in the compounds, further insight into the phonon transport properties were considered to compare the ordered and disordered compounds. As discussed in the previous section, the usual phonon transport model based on the Debye approximation may be insufficient to describe the lattice thermal conductivity of AMg_2Bi_2 compounds. First-principle calculations of the third order force constants may give an insightful description of the phonon transport properties. But such

calculations require a huge amount of computation resources. The situation is even more problematic for the disordered compounds. Hence, we applied an approximate Boltzmann-Peierls theory, namely a generalized Callaway formula [36], to the ordered and disordered compounds.

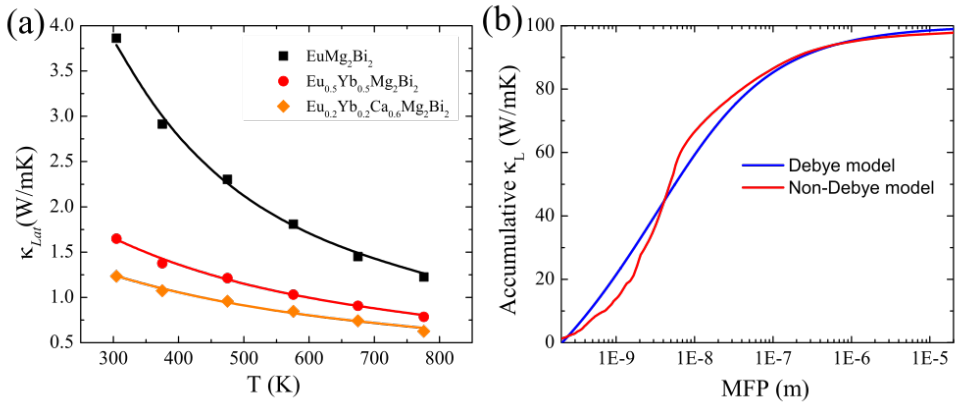

Figure 3.19 (a) Lattice thermal conductibility of (Ca,Eu,Yb)Mg_2Bi_2; (b) The accumulative lattice thermal conductivity vs. mean free-path in $Yb_{0.2}Eu_{0.2}Ca_{0.6}Mg_2Bi_2$.

We use the following high-temperature expression, which is a generalization of the Callaway treatment to a non-Debye approximation

$$\kappa_{lat} = \frac{k_B}{3V}\int I(\omega)d\omega \tag{3.4}$$

where $I(\omega) \equiv \langle v_g^2 \rangle_\omega G(\omega)\tau(\omega)$, V is the unit volume, ω is the phonon angular frequency, k_B is the Boltzmann constant, $\langle v_g^2 \rangle_\omega$ is the frequency averaged group velocity, $G(\omega)$ is the density of states, and $\tau(\omega)$ is a relaxation time, which in the Callaway treatment is independent of normal-mode polarization.

We consider four scattering mechanisms in (Ca,Eu,Yb)Mg_2Bi_2: the point-defects

scattering, phonon-phonon scattering, electron-phonon scattering, and grain boundary scattering. The relaxation times are $\tau_{PD}^{-1} = A\omega^4$, $\tau_U^{-1} = BT\omega^2$, $\tau_{PE}^{-1} = C\omega$ and $\tau_{GB}^{-1} = \frac{v_a}{L}$, respectively. Therefore, the combined phonon relaxation time can be expressed as:

$$\tau_C^{-1} = A\omega^4 + BT\omega^2 + C\omega + \frac{v_s}{L} \tag{3.5}$$

where L is the average grain size (taken from the TEM observation), and the coefficients *A, B,* and *C* are fitting parameters. The fitted results are shown as the solid lines in Fig. 3.19a. The coefficients *A, B,* and *C* for all of these samples are summarized in Table 3.7.

Table 3.6 Values of lattice thermal conductivity fit parameters as defined by Eqs. 3.4 and 3.5.

Composition	B (10^{-17}sK^{-1})	A (10^{-40} s^3)	C (10^{-34})	L (nm)
$EuMg_2Bi_2$	1.7	0	0.1	300
$Yb_{0.5}Eu_{0.5}Mg_2Bi_2$	1.74	0.76	0.1	300
$Yb_{0.2}Eu_{0.2}Ca_{0.6}Mg_2Bi_2$	1.78	1.25	0.1	300

The electron-phonon scattering is very weak in all three samples, indicating low deformation potential E_{def}, which is also responsible for the high carrier mobility observed above [34]. The strength of the phonon-phonon scatterings is nearly unchanged based on the similar B (discussed later), while the point-defect scattering rate increases with the site substitution. For instance, the point-defect scattering of $Yb_{0.2}Eu_{0.2}Ca_{0.6}Mg_2Bi_2$ is twice that of $Yb_{0.5}Eu_{0.5}Mg_2Bi_2$, indicating the effect of remarkable mass and strain field fluctuation. Therefore, the fitted results are consistent with the TEM observation.

To study the effects of nanostructures on the lattice thermal conductivity of (Ca,Eu,Yb)Mg_2Bi_2 alloys, we calculated the accumulative lattice thermal conductivity of $Yb_{0.2}Eu_{0.2}Ca_{0.6}Mg_2Bi_2$, as shown in Fig. 3.19b. It is clear that a large portion of heat is carried by phonons with mean free path lengths longer than 300 nm. Therefore, the nanostructures can decrease the lattice thermal conductivity of (Ca,Eu,Yb)Mg_2Bi_2 alloys.

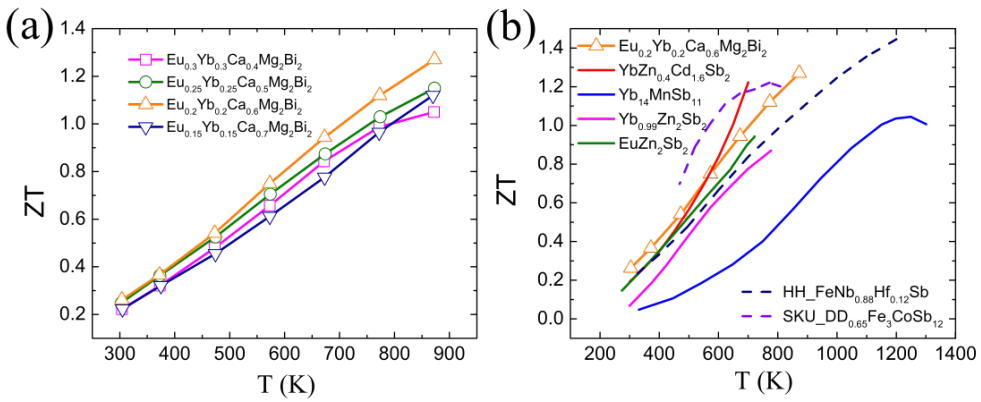

Figure 3.20 Thermoelectric performance for p-type zintl phases. (a) Temperature-dependent *ZT* values for $(Eu_{0.5}Yb_{0.5})_{1-x}Ca_xMg_2Bi_2$, and (b) *ZT* comparison of typical high temperature p-type Zintl phases materials [3,7,8,37]and other good p-type skutterudites (SKU) [38] and half-Heuslers (HH) [39].

Enhanced Figure of Merit. The highest *ZT* that can be achieved in a given material system is governed by its material parameter

$$B = 5.745\times10^{-6}\frac{\mu(m^*/m_0)^{3/2}}{\kappa_{Lat}}T^{5/2} \tag{3.6}$$

where m^*, m_0, μ, κ_{Lat}, and T are the carrier effective mass, free-electron mass, carrier mobility, lattice thermal conductivity, and absolute temperature, respectively. Therefore,

heavy effective mass, high carrier mobility, and low lattice thermal conductivity are highly desirable for good thermoelectric performance.

However, in the simplest solid solutions, the net result of alloying on *ZT* relies on two effects with opposite influences: mobility reduction and lattice thermal conductivity reduction. Here, because of the band structure engineering with weak chemical disorder scattering, weakly affected mobility is achieved. Further reduction of thermal conductivity by strain fluctuation scattering successfully leads to a record peak *ZT* of ~1.3 in $Eu_{0.2}Yb_{0.2}Ca_{0.6}Mg_2Bi_2$ (Fig. 3.20a). Such a *ZT* value is competitive with the reported Sb-based p-type Zintl phases [3,7,8,37] and even other good p-type skutterudites [38] and half-Heuslers [39] in this temperature range (Fig. 3.20b). Compared with best TE performance of $YbZn_{0.4}Cd_{1.6}Sb_2$, our Bi-based Zintl phases are non-toxic in addition to having a higher *ZT*, which is beneficial in aiming toward practical applications of these compounds.

Conclusion. We demonstrated for the first time that the base Zintl compound $EuMg_2Bi_2$ can achieve peak *ZT* ~1. Further partial substitution of Ca and Yb at Eu obtains a *ZT* as high as ~1.3 in $(EuYb)_{0.2}Ca_{0.6}Mg_2Bi_2$, better than the best known Sb-based Zintl compound $YbZn_{0.4}Cd_{1.6}Sb_2$. The low lattice thermal conductivity resulted from dislocations and multiple types of strains, as well as nanostructures, and plays a decisive role in the enhanced TE performance. DFT calculations indicate this chemical disorder scattering only influences the conduction band, ensuring the relatively high carrier mobility. This finding of better TE performance of Bi-based Zintl phases could pave the way for practical applications of this compound for middle temperature ranges.

3.5 Reference

[1] T. Caillat, J. P. Fleurial, A. Borshchevsky, *Journal of Physics and Chemistry of Solids* **1997**, *58*, 1119–1125.

[2] M. Chitroub, F. Besse, H. Scherrer, *Journal of Alloys and Compounds* **2008**, *460*, 90–93.

[3] S. R. Brown, S. M. Kauzlarich, F. Gascoin, G. J. Snyder, *Chem. Mater.* **2006**, *18*, 1873–1877.

[4] E. S. Toberer, C. A. Cox, S. R. Brown, T. Ikeda, A. F. May, S. M. Kauzlarich, G. J. Snyder, *Adv. Funct. Mater.* **2008**, *18*, 2795–2800.

[5] H. Xu, K. M. Kleinke, T. Holgate, H. Zhang, Z. Su, T. M. Tritt, H. Kleinke, *J. Appl. Phys.* **2009**, *105*, 053703–6.

[6] F. Gascoin, S. Ottensmann, D. Stark, S. M. Haïle, G. J. Snyder, *Adv. Funct. Mater.* **2005**, *15*, 1860–1864.

[7] H. Zhang, J.-T. Zhao, Y. Grin, X.-J. Wang, M.-B. Tang, Z.-Y. Man, H.-H. Chen, X.-X. Yang, *J. Chem. Phys.* **2008**, *129*, 164713–6.

[8] X.J. Wang, M.B. Tang, H.H. Chen, X.X. Yang, J.T. Zhao, U. Burkhardt, Y. Grin, *Appl. Phys. Lett.* **2009**, *94*, 092106–4.

[9] H. Zhang, L. Fang, M. B. Tang, Z. Y. Man, H. H. Chen, X. X. Yang, M. Baitinger, Y. Grin, J. T. Zhao, *J. Chem. Phys.* **2010**, *133*, 194701–6.

[10] E. S. Toberer, A. F. May, B. C. Melot, E. Flage-Larsen, G. J. Snyder, *Dalton Trans.* **2010**, *39*, 1046–1054.

[11] C. Zheng, R. Hoffmann, R. Nesper, H. G. Von Schnering, *J. Am. Chem. Soc.* **1986**, *108*, 1876–1884.

[12] J. K. Burdett, G. J. Miller, *Chem. Mater.* **1990**, *2*, 12–26.

[13] A. F. May, M. A. McGuire, D. J. Singh, R. Custelcean, G. E. Jellison Jr., *Inorg. Chem.* **2011**, *50*, 11127–11133.

[14] A. F. May, M. A. McGuire, D. J. Singh, J. Ma, O. Delaire, A. Huq, W. Cai, H. Wang, *Phys. Rev. B* **2012**, *85*, 035202–10.

[15] D. Ramirez, A. Gallagher, R. Baumbach, T. Siegrist, *Journal of Solid State*

Chemistry **2015**, *231*, 217–222.

[16] J. P. Perdew, K. Burke, M. Ernzerhof, *Phys. Rev. Lett.* **1996**, *77*, 3865–3868.

[17] Gironcoli D, et al., *J. Phys.: Condens. Matter* **2009**, *21*, 395502.

[18] A. I. Liechtenstein, V. I. Anisimov, J. Zaanen, *Phys. Rev. B* **1995**, *52*, 5467–5470.

[19] N. Marzari, A. A. Mostofi, J. R. Yates, I. Souza, D. Vanderbilt, *Rev. Mod. Phys.* **2012**, *84*, 1419–1475.

[20] H. Akai, P. H. Dederichs, *Phys. Rev. B* **1993**, *47*, 8739–8747.

[21] H. Akai, *Phys. Rev. Lett.* **1998**, *81*, 3002–3005.

[22] L.D. Zhao, S.H. Lo, J. He, H. Li, K. Biswas, J. Androulakis, C.I. Wu, T. P. Hogan, D.Y. Chung, V. P. Dravid, *J. Am. Chem. Soc.* **2011**, *133*, 20476–20487.

[23] V. Murashov, M. A. White, T. M. Tritt, **2004**.

[24] R. Setnescu, I. Bancuta, T. Setnescu, V. CIMPOCA, S. Jipa, I. POPESCU, *The 2th Coference on Applied Sciences in Envoronmental and Materials Studies* **2010**, 28–30.

[25] R. He, H. S. Kim, Y. Lan, D. Wang, S. Chen, Z. Ren, *RSC Advances* **2014**, *4*, 64711–64716.

[26] Q. Jie, H. Wang, W. Liu, H. Wang, G. Chen, Z. Ren, *Phys. Chem. Chem. Phys.* **2013**, *15*, 6809–6816.

[27] J. Shuai, Z. Liu, H. S. Kim, Y. Wang, J. Mao, R. He, J. Sui, Z. Ren, *J. Mater. Chem. A* **2016**, *4*, 4312–4320.

[28] L. Bjerg, G. K. H. Madsen, B. B. Iversen, *Chem. Mater.* **2012**, *24*, 2111–2116.

[29] J. H. Van Vleck, *Phys. Rev.* **1932**, *41*, 208–215.

[30] J. Zhang, L. Song, K. F. F. Fischer, W. Zhang, X. Shi, G. K. H. Madsen, B. B. Iversen, *Nature Communications* **2016**, *7*, 1–7.

[31] D. J. Singh, D. Parker, *J. Appl. Phys.* **2013**, *114*, 143703–8.

[32] C. Chiritescu, C. Mortensen, D. G. Cahill, D. Johnson, P. Zschack, *J. Appl. Phys.* **2009**, *106*, 073503–6.

[33] Y.L. Pei, Y. Liu, *Journal of Alloys and Compounds* **2012**, *514*, 40–44.

[34] H. Wang, A. D. LaLonde, Y. Pei, G. J. Snyder, *Adv. Funct. Mater.* **2012**, *23*,

1586–1596.

[35] J. He, M. G. Kanatzidis, V. P. Dravid, *Materials Today* **2013**, *16*, 166–176.

[36] J. Callaway, *Phys. Rev.* **1959**, *113*, 1046–1051.

[37] A. Zevalkink, W. G. Zeier, E. Cheng, J. Snyder, J.P. Fleurial, S. Bux, *Chem. Mater.* **2014**, *26*, 5710–5717.

[38] G. Rogl, A. Grytsiv, P. Rogl, E. Bauer, M. Zehetbauer, *Intermetallics* **2011**, *19*, 546–555.

[39] C. Fu, S. Bai, Y. Liu, Y. Tang, X. Zhao, L. Chen, T. Zhu, *Nature Communications* **2016**, *6*, 1–7.

Chapter 4

Phase Pure $Ca_{1-x}Yb_xZn_2Sb_2$, $Ca_{1-x}Eu_xZn_2Sb_2$, and $Eu_{1-x}Yb_xZn_2Sb_2$ by Mechanical Alloying and Hot Pressing

Reproduced with permission from *Nano Energy*, 25, 134-144 (2016).

4.1 Introduction

It is well known that thermoelectric properties are dependent on chemical composition and microstructure that is sensitive to the preparation method. The traditional method such as melting-solidification-annealing (briefed as "melting" hereafter) is widely used for preparing thermoelectric samples with good thermoelectric properties in some cases [1-4]. However, for some materials with elements having high vapor pressure like Mg in $Mg_2Si_{1-x}Sn_x$ or Sb in Skutterudites, it is difficult to use high temperature melting method for accurate control of the molar ratio [5-7]. Therefore, alternatively, mechanical alloying (MA) by high-energy ball milling process is studied for the synthesis of double filled skutterudites p-type $Ce_{0.45}Nd_{0.45}Fe_{3.5}Co_{0.5}Sb_{12}$ and n-type $CoSb_{3-x}Te_x$, Mg_2Si-Mg_2Sn alloy, *etc.* [8-14] and also has achieved a great success to fabricate a variety of poplar high-performance thermoelectric bulk materials such as Bi_2Te_3 [15] and PbTe [10], PbSe [16] without introducing any impurity.

Zintl phases AM_2X_2 (A = Ca, Yb, Eu, Sr; M = Zn, Mn, Cd, Mg; X = Sb, Bi), especially AZn_2Sb_2, crystalizing in $CaAl_2Si_2$ structure, have been extensively studied as

thermoelectric materials [17-22]. For many years, the dominant preparation method for AZn_2Sb_2 zintl compounds has been melting. For example, the reported synthesis process for $Ca_{1-x}Yb_xZn_2Sb_2$ is to first heat the samples to above 1000 ^oC and hold them at that temperature between 12 h and 96 h, and then cool the samples down to between 500 ^oC and 800 ^oC and hold for more than two days [17]. The total processing time of this method is more than 200 h. Besides, all the previous reports on Zintl phase AZn_2Sb_2 via melting method have ZnSb, Zn_4Sb_3 or $M_9Zn_{4.5}Sb_9$ (M = Yb, Eu) as the secondary phases [17-22]. The recent study shows that the observed extremely high carrier concentration can be explained by the vacancies in A-site. The initial high-temperature step may have led Yb to vaporize or react with the container [23]. The DFT calculation also predicated that vacancies on the A-site are most energetically favorable point defects and concentration of vacancies depends strongly on the electronegativity of A [24]. The residual vacancies and impurities have an impact on the measured thermoelectric performance and make it difficult to fully understand the fundamental thermoelectric properties in AZn_2Sb_2 series, especially when trying to study the effects caused by elemental substitutions. Considering the drawbacks of defect formation and long time process by melting method, mechanical alloying (MA) by high-energy ball milling process is studied for synthesis of these Zintl compounds.

The current study aims to explore the effect of ball milling and hot pressing method on the thermoelectric performances of $Ca_{1-x}Yb_xZn_2Sb_2$, $Ca_{1-x}Eu_xZn_2Sb_2$, and $Eu_{1-x}Yb_xZn_2Sb_2$ samples. By preparing all samples without impurities detected by XRD, the fundamental thermoelectric properties, such as effective mass and mobility, would be

explored. A significant enhancement on thermoelectric properties is achieved in $Ca_{1-x}Yb_xZn_2Sb_2$ compounds. The highest *ZT* value of ~0.9 is observed for the optimized composition $Ca_{0.25}Yb_{0.75}Zn_2Sb_2$, which is ~50% higher than the reported values [17].

4.2 Sample Synthesis and Results of Characterization

Sample preparation. Calcium (Ca, Sigma Aldrich, 99.9%, pieces), ytterbium (Yb, Sigma Aldrich, 99.9%, cubes), europium (Eu, Atlantic, 99.9%, cubes), zinc (Zn, Sigma Aldrich, 99.9%, powder), and antimony (Sb, Sigma Aldrich, 99.999%, chunks) were weighed according to the stoichiometry of $Ca_{1-x}Yb_xZn_2Sb_2$ (x = 0, 0.25, 0.5, 0.75, and 1), $EuZn_2Sb_2$, $Eu_{0.5}Yb_{0.5}Zn_2Sb_2$, $Eu_{0.5}Ca_{0.5}Zn_2Sb_2$, and sealed directly in the stainless steel jar with stainless steel balls inside an argon-filled glovebox. Then jar was taken out for mechanical alloying by a high energy ball mill (SPEX 8000D) for 12 h. The obtained final nanopowder was then loaded into a graphite die with an inner diameter of 12.7 mm, and consolidated by hot pressing at ~923 K for 2 min. The unchanged mass of stainless jar and stainless balls after thousands of ball milling hours indicates less effect from source of ion contamination. The final hot pressed samples were sliced and polished avoiding any carbon element during hot-press for later characterization.

Results of Characterization. The XRD patterns of $Ca_{1-x}Yb_xZn_2Sb_2$ (x = 0, 0.25, 0.5, 0.75, and 1), $Eu_{0.5}Yb_{0.5}Zn_2Sb_2$, $Eu_{0.5}Ca_{0.5}Zn_2Sb_2$, and $EuZn_2Sb_2$ are shown in Fig. 4.1a and b. All diffraction peaks are indexed according to the reported structure of $CaAl_2Si_2$ (space group $P\bar{3}m1$, No. 164) [25]. All the samples were found to be phase pure within the

XRD detection limit. However, by using the melting method, most reports show the impurity phases, such as ZnSb, Zn_4Sb_3, and $M_9Zn_{4.5}Sb_9$ (M = Yb, Eu) [17-22]. The refined unit cell parameters *a* and *c* of each compound are shown in Fig. 4.1c. Little variation is observed in the lattice parameters of all $Ca_{1-x}Yb_xZn_2Sb_2$ compounds, represented by first five samples, because of similar atomic radius of Ca (194 pm) and Yb (197 pm). The last three Eu containing samples are observed to show a larger unit cell parameters *a* and *c*, consistent with the bigger atomic radius of Eu (204 pm). As expected, among the last three samples, the Eu-rich compound $EuZn_2Sb_2$ showed the largest lattice parameter (*a*,*c*).

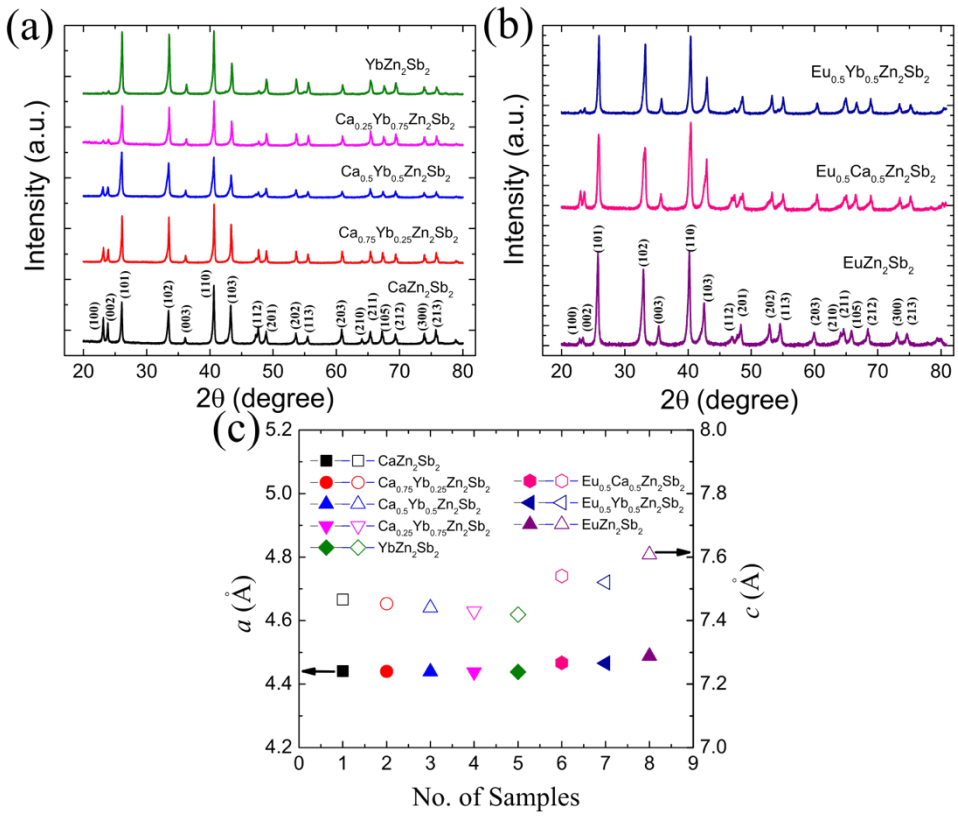

Figure 4.1 (a) XRD patterns for $Ca_{1-x}Yb_xZn_2Sb_2$ (x = 0, 0.25, 0.5, 0.75, and 1); (b) XRD patterns for $EuZn_2Sb_2$, $Eu_{0.5}Ca_{0.5}Zn_2Sb_2$, and $Eu_{0.5}Yb_{0.5}Zn_2Sb_2$. (c) Refined lattice parameters *a* and *c* for $Ca_{1-x}Yb_xZn_2Sb_2$ (x = 0, 0.25, 0.5, 0.75, and 1), $EuZn_2Sb_2$, $Eu_{0.5}Ca_{0.5}Zn_2Sb_2$, and $Eu_{0.5}Yb_{0.5}Zn_2Sb_2$.

The SEM and STEM images of the optimized $Ca_{0.25}Yb_{0.75}Zn_2Sb_2$ sample are displayed in Fig. 4.2a and b. Both of them clearly indicate the sample is densely packed. A wide range of grain size from 50 to 500 nm is also observed. Fig. 4.2c shows a high-resolution TEM image to elucidate two grains adjacent to each other. The corresponding fast Fourier transformation (FFT) image for upside grain, as the inset of Fig. 4.2c, can be successfully indexed according to $P\bar{3}m1$ hexagonal structure along the [301] zone axis. Interestingly, some black (indicated by the black arrow) and white (indicated by the white arrow) nanoinclusions can be observed under high magnification, shown in Fig. 4.2d. Most of these nanoinclusions, hardly detected by XRD, range from 5 nm to 10 nm. To further investigate the elemental compositions of these nanoinclusions, the energy dispersive X-ray (EDX) elemental mapping has been taken to analyze the elemental distributions and are shown in Fig. 4.2e and Fig. 4.2f. It is found that the white nanoinclusions represent Yb-rich precipitates, while the black nanoinclusions represent element-poor precipitates with less concentration of some elements. Those small size of nano-precipitates might affect phonons with very small mean free path and make some contributes to lower the lattice thermal conductivity.

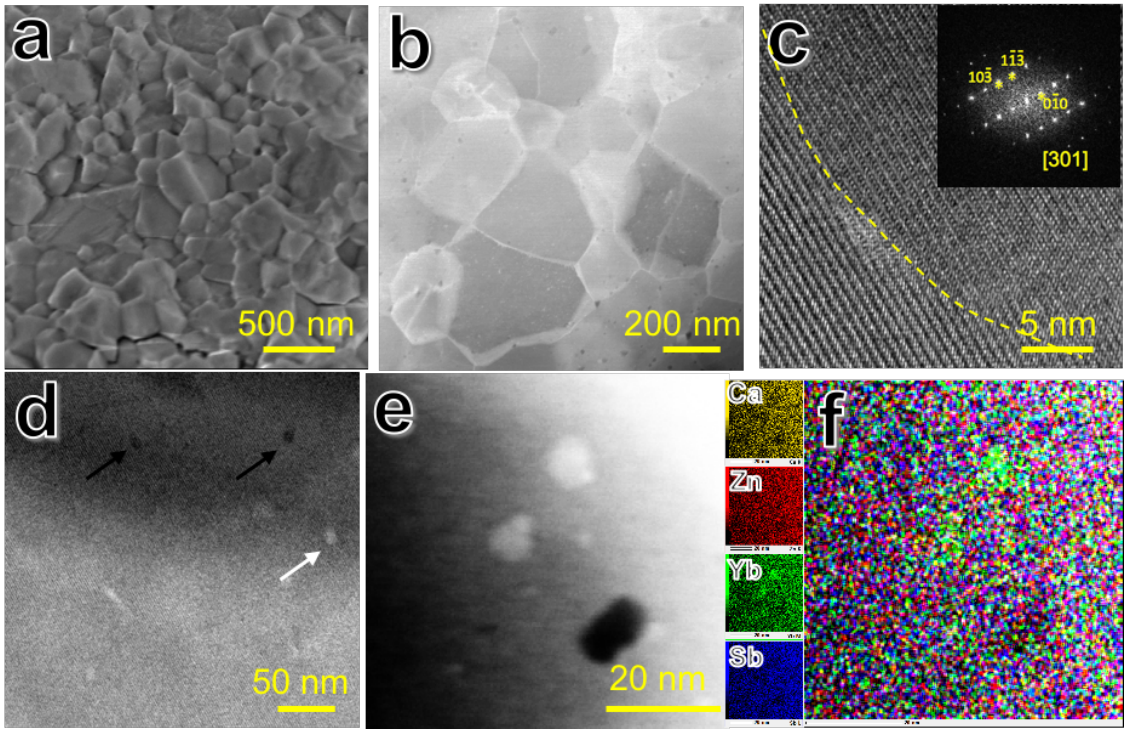

Figure 4.2 Typical microstructure for $Ca_{0.25}Yb_{0.75}Zn_2Sb_2$. (a) SEM image; (b) STEM imge; (c) high magnification TEM with grain boundary with Fast Fourier transformation (FFT) image for right side grain; (d) high magnification TEM images with black and white nanoinclusions; (e) and (f) EDS mapping for the selected enlarged nanoinclusions.

4.3 Transport Properties and Discussion

The temperature dependence of electrical resistivity and Seebeck coefficient of all ball milled and hot pressed $Ca_{1-x}Yb_xZn_2Sb_2$ compounds are shown in Fig. 4.3a. and 4.3c. They behave like typical degenerated semiconductor: increase with temperature. In Fig. 4.3a, by increasing Yb content, the resistivity is decreased for $x < 0.5$ and then increased a little. For comparison, the resistivity and Seebeck coefficient of three representative samples by melting method ($CaZn_2Sb_2$, $YbZn_2Sb_2$, and $Ca_{0.25}Yb_{0.75}Zn_2Sb_2$) reported by

Gascoin *et al*. are also shown [17]. Clearly, $CaZn_2Sb_2$ (x = 0) prepared by melting shows much higher resistivity and also higher Seebeck coefficient, while $YbZn_2Sb_2$ (x = 1) by the melting method exhibits lower resistivity and much lower Seebeck coefficient. The optimized sample $Ca_{0.25}Yb_{0.75}Zn_2Sb_2$ (x = 0.75) via ball milling shows a lower resistivity and higher Seebeck coefficient than the same composition by melting. For $Ca_{1-x}Yb_xZn_2Sb_2$ samples made by melting, the electric resistivity drops sharply from 23.7 $\mu\Omega$ m to 3.2 $\mu\Omega$ m as Yb content increases, which might attribute to the increased Yb vacancies. The melting method would introduce A-site vacancies to form probably because of heavy loss of atom A during the processing. Deficiency of A-site cations leads to fewer electrons in the bonding and anti-bonding states, which would contribute to the lower resistivity by increasing the hole carrier concentration. At the same time, the increased carrier concentration would contribute to the reduction in Seebeck coefficient for samples made by melting based on Pisarenko relations with the assumption of similar effective mass [17] (further discussed later).

The electric transport properties of ball milled and hot pressed Eu-containing samples $EuZn_2Sb_2$ and $Eu_{0.5}A_{0.5}Zn_2Sb_2$ (A= Yb, Ca) are also shown in comparison with $CaZn_2Sb_2$, $YbZn_2Sb_2$, and $Ca_{0.5}Yb_{0.5}Zn_2Sb_2$ in Fig. 4.3b and Fig. 4.3d. The resistivity of $EuZn_2Sb_2$ is higher than $YbZn_2Sb_2$ but lower than $CaZn_2Sb_2$. The Eu alloyed compounds ($Eu_{0.5}Ca_{0.5}Zn_2Sb_2$ and $Eu_{0.5}Yb_{0.5}Zn_2Sb_2$) appear to have intermediate properties. The resistivity and Seebeck coefficient of $EuZn_2Sb_2$ appears not much different from the reported melting samples [18]. The tendency for Eu to form the vacancies is hard, as calculated by G. S. Pomrehn *et al*. [24], which might be the reason why the electric

transport properties appear similar between two different synthesis method. Power factor ($PF = S^2/\rho$) calculated from the measured electrical resistivity and Seebeck coefficient is plotted in Fig. 4.3e and f. In Fig. 4.3e, with higher Yb concentration, the power factor of $Ca_{1-x}Yb_xZn_2Sb_2$ samples increases. Compared with the three samples prepared by melting method, the power factors of all our samples are ~100% higher, mainly attribute to the higher phase purity by eliminating the A-site vacancies. Among all the samples shown in Fig. 4.3f, $EuZn_2Sb_2$ possesses the highest power factor of ~21 μW cm^{-1} K^{-2}.

The carrier concentration (n) and Hall mobility (μ) are listed in Table 4.1, and related to electrical resistivity by $1/\rho = ne\mu$. The effect of Yb concentration on resistivity and carrier concentration is plotted in Fig. 4.4a. With increasing Yb concentration, the carrier concentration of samples by melting increases from $3.1x10^{19}$ to $15x10^{19}$ cm^{-3} and resistivity decreases sharply, as a result of increased vacancies in Yb-site by melting method. However, our samples prepared by ball milling and hot pressing method showed lower carrier concentrations, with the highest of ~$8.75x10^{18}$ cm^{-3} in $Ca_{0.5}Yb_{0.5}Zn_2Sb_2$, about half of that in $YbZn_2Sb_2$ by melting.

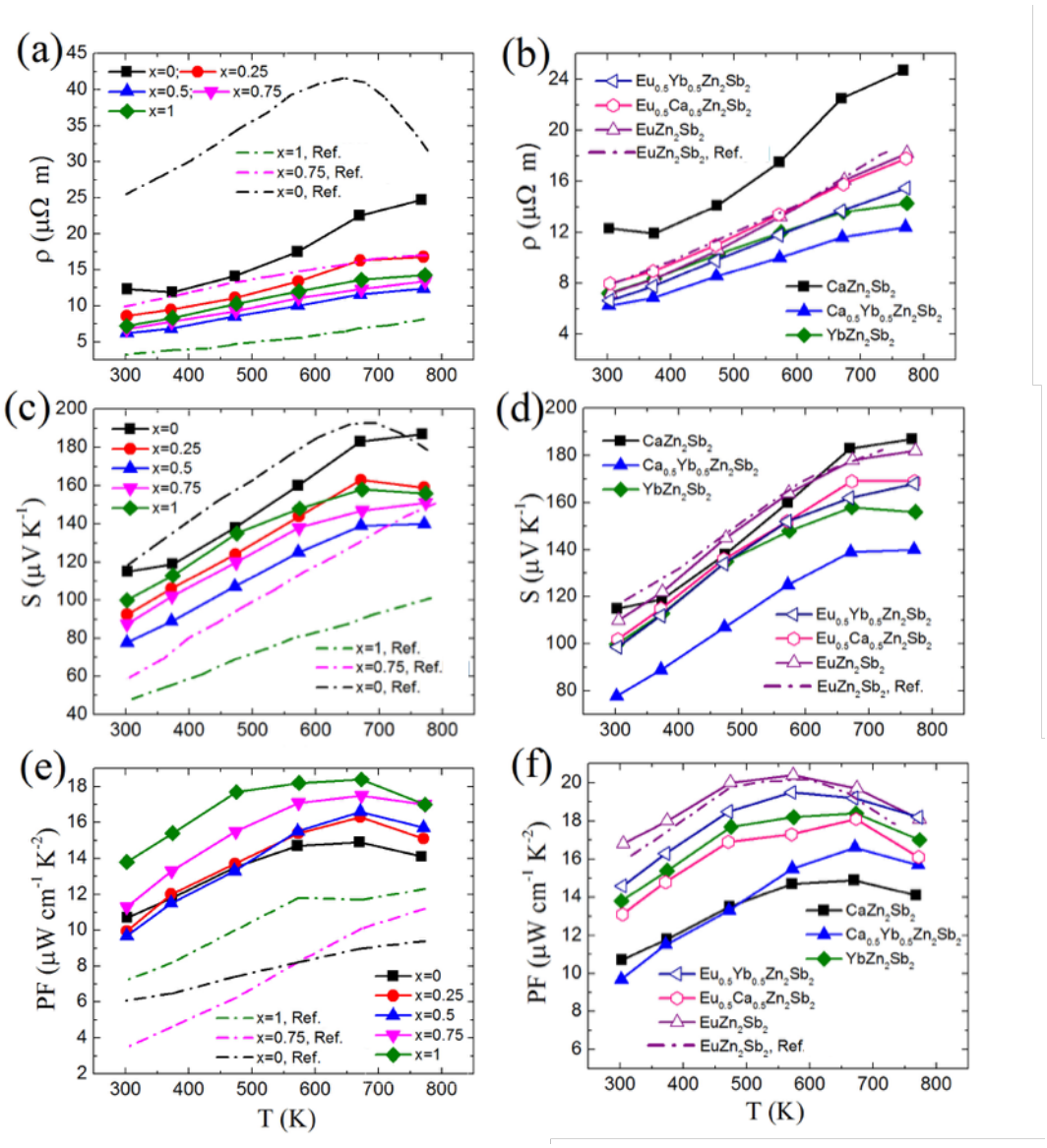

Figure 4.3 Temperature-dependent thermoelectric properties of $Ca_{1-x}Yb_xZn_2Sb_2$ (x = 0, 0.25, 0.5, 0.75, and 1), $EuZn_2Sb_2$, $Eu_{0.5}Ca_{0.5}Zn_2Sb_2$, and $Eu_{0.5}Yb_{0.5}Zn_2Sb_2$: (a) and (b) electrical resistivity; (c) and (d) Seebeck coefficient; (e) and (f) power factor. Four typical compounds from literature are included for comparison.

Table 4.1 Room-temperature thermoelectric transport properties of $Ca_{1-x}Yb_xZn_2Sb_2$, $EuZn_2Sb_2$, $Eu_{0.5}Ca_{0.5}Zn_2Sb_2$, and $Eu_{0.5}Yb_{0.5}Zn_2Sb_2$.

$Ca_{1-x}Yb_xZn_2Sb_2$	$x = 0$	$x = 0.25$	$x = 0.5$	$x = 0.75$	$x = 1$
Carrier concentration (10^{19} cm^{-3})	5.92	6.91	8.72	6.08	4.14
Hall mobility (cm^2 V^{-1} s^{-1})	85.9	105	115	152	209
Effective mass (m_e)	1.02	0.85	0.81	0.73	0.66

AZn_2Sb_2	Eu	$Eu_{0.5}Ca_{0.5}$	$Eu_{0.5}Yb_{0.5}$
Carrier concentration (10^{19} cm^{-3})	3.60	5.11	4.49
Hall mobility (cm^2 V^{-1} s^{-1})	240	153	210
Effective mass (m_e)	0.69	0.79	0.69

The single parabolic band model has been successfully applied in Zintl AZn_2Sb_2 system and DFT calculation has also demonstrated that AZn_2Sb_2 contains three bands at the valence band edge that are degenerate at Γ point, which can be modeled as a single parabolic band with a single combined effective mass [21]. Previous studies show those Zintl compounds have similar effective mass of ~0.6 m_e [21-23]. The Pisarenko relations are plotted in Fig. 4.4b by using a density of states (DOS) effective mass $m^* = 0.6\ m_e$ and assuming acoustic phonons are the primary scattering sources [26,27]. The well-

established Pisarenko relations between the Seebeck coefficient and carrier concentration gives a good description of the experimental data for rare earth alloyed AZn_2Sb_2 samples. However, for Ca-rich AZn_2Sb_2, the enhanced Seebeck coefficient lying above the Pisarenko line indicates an increase in the density of state mass.

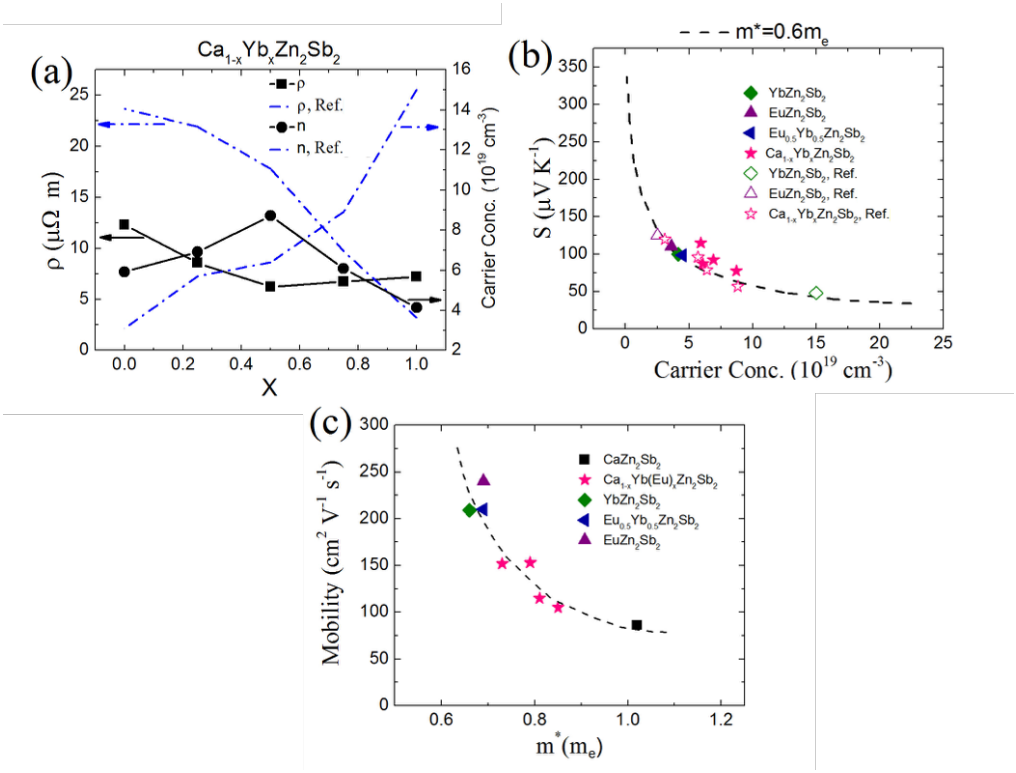

Figure 4.4 (a) Room temperature resistivity and carrier concentration comparison between samples of $Ca_{1-x}Yb_xZn_2Sb_2$ (x = 0, 0.25, 0.5, 0.75, and 1) made by ball milling and melting; (b) Seebeck coefficients dependence of carrier concentration n in accordance with a single band model with $m^* = 0.6\ m_e$ at 300K; (c) Carrier mobility verses effective mass for all samples.

SPB model is used to calculate each sample's DOS effective mass [26-28]. The Ca-rich compound shows higher effective mass than the rare earth-rich compounds, and with more Ca, the effective mass gradually increases (Table 4.1). With increasing Ca

concentration, the Hall mobility gradually decreases to 85.9 $cm^2\ V^{-1}\ s^{-1}$ in $CaZn_2Sb_2$. The highest mobility of ~240 $cm^2\ V^{-1}\ s^{-1}$ is found in $EuZn_2Sb_2$. Although higher concentration would lead to lower mobility, the big difference in mobility between the rare earth and Ca alloyed AZn_2Sb_2 is surprising. The classical definition of mobility is ($\mu = e\tau/m^*$) [29,30]. Previous studies assume the effective masses for all AZn_2Sb_2 samples are almost similar, the difference in mobility is most likely interpreted by the changes in τ arising from differences in microstructure and/or bonding features. Here, the experimental data from our samples by ball milling and hot pressing shows that the Hall mobility (μ) decreases with increased effective mass (Fig. 4.4c). Therefore, it is also possible that the change of effective mass would also change the mobility.

Fig. 4.5 shows the temperature-dependent thermal transport behavior of $Ca_{1-x}Yb_xZn_2Sb_2$ and Eu alloyed AZn_2Sb_2 samples. Specific heat (C_p) for all samples is shown in Fig. 4.5a and it decreases gradually from Ca rich samples to Yb/Eu rich samples because of the increased atomic mass. All the specific heat curves increase with temperature. Fig. 4.5b shows the thermal diffusivity of all samples. With increasing temperature, the diffusivity (D) of all samples shows a gradually decreasing tendency. C_p and D are used to calculate the total thermal conductivity (κ) of all the samples by $\kappa = D\rho_D C_p$, where ρ_D is the measured density of samples. Densities of samples $Ca_{1-x}Yb_xZn_2Sb_2$ with x = 0, 0.25, 0.5, 0.75, and 1 are 5.25, 5.74, 6.23, 6.61, 7.05 g cm^{-3}, and densities for samples $Eu_{0.5}Yb_{0.5}Zn_2Sb_2$, $Eu_{0.5}Ca_{0.5}Zn_2Sb_2$, and $EuZn_2Sb_2$ are 6.90, 6.04, and 6.81, respectively, ~ 98% of the theoretical densities. As shown in Fig. 4.5c, the total thermal conductivity decreases dramatically in the mixed Ca/Yb compounds $Ca_{1-x}Yb_xZn_2Sb_2$ made by different

methods, indicating alloying is quite effective in lowering the lattice thermal conductivity. The much high thermal conductivity in sample $YbZn_2Sb_2$ by melting might attribute to the increased electronic contribution κ_e, estimated using the Wiedemann−Franz relationship ($\kappa_e = LT/\rho$), where L is the Lorenz number, approximated using a single parabolic band model [28]. In Fig. 4.5d, it is clear that the samples with Ca and Yb/Eu have lower thermal conductivity because of the mass fluctuations, while samples with mixed Eu/Yb isn't influenced by point defect scattering because of the similar atomic mass. However, given the considerable amounts of impurity phases $Eu_9Zn_{4.5}Sb_9$ [18], the $EuZn_2Sb_2$ sample by melting shows a little lower thermal conductivity. By directly subtracting the electronic contribution from the total thermal conductivity, the lattice thermal conductivity (κ_L) were obtained and shown in Fig. 4.5e and f. It is observed that lattice thermal conductivity of $CaZn_2Sb_2$ prepared by different methods appear to be similar, while the Yb-containing samples via ball milling show a little lower lattice thermal conductivity. As detected by EDX in Fig. 4.2f, Yb-rich nano precipitates might have effects on scattering the phonons with small mean free path to lower the lattice thermal conductivity. For the alloyed $Ca_{0.5}Yb_{0.5}Zn_2Sb_2$ sample, the lattice thermal conductivity reaches as low as 0.4 W m^{-1} K^{-1} mainly because of the point defects. This point defects scattering also lower the lattice thermal conductivity in $Eu_{0.5}Ca_{0.5}Zn_2Sb_2$, but not in $Eu_{0.5}Yb_{0.5}Zn_2Sb_2$ because of the dominating mass disorder scattering effect. The data reported before on $EuZn_2Sb_2$ suggested a significant lower lattice thermal conductivity [18], which is not really correct since they overestimated the κ_e by using higher L.

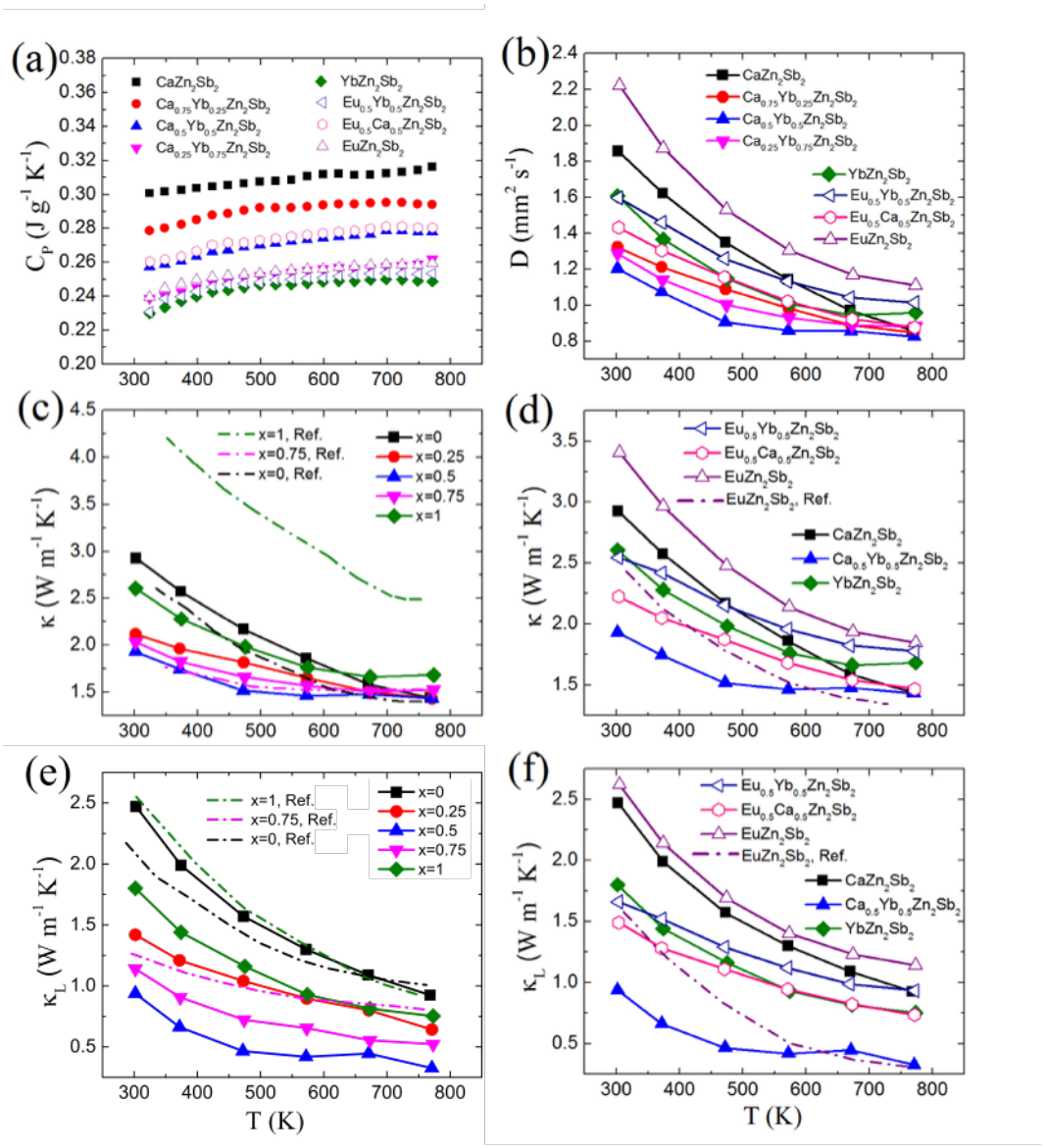

Figure 4.5 Temperature-dependent thermal transport properties of $Ca_{1-x}Yb_xZn_2Sb_2$ (x = 0, 0.25, 0.5, 0.75, and 1), $EuZn_2Sb_2$, $Eu_{0.5}Ca_{0.5}Zn_2Sb_2$, and $Eu_{0.5}Yb_{0.5}Zn_2Sb_2$: (a) Specific heat; (b) thermal diffusivity; (c) and (d) total thermal conductivity; and (e) and (f) lattice thermal conductivity. Four typical compounds from literature are included in (c), (d) and (f) for comparison.

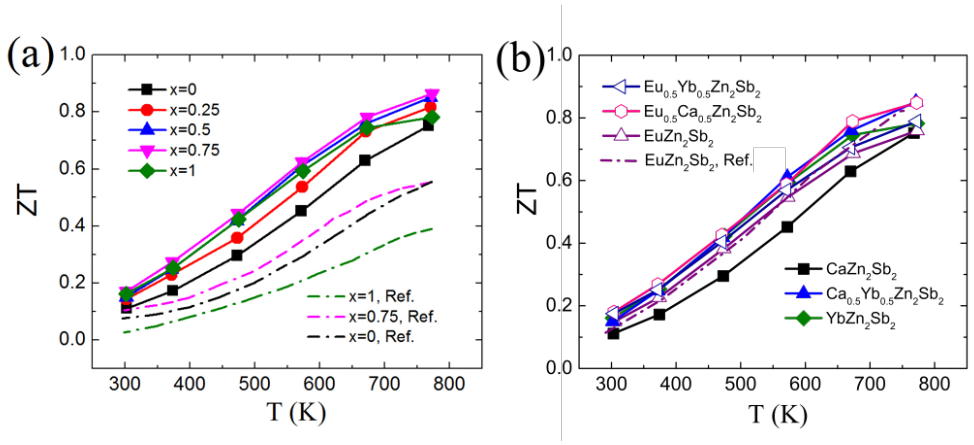

Figure 4.6 Temperature-dependent *ZT* for $Ca_{1-x}Yb_xZn_2Sb_2$ (x = 0, 0.25, 0.5, 0.75, and 1) $EuZn_2Sb_2$, $Eu_{0.5}Ca_{0.5}Zn_2Sb_2$, and $Eu_{0.5}Yb_{0.5}Zn_2Sb_2$. Four typical compounds from literature are included in (a) and (b) for comparison.

Combining the electrical and thermal properties, the corresponding *ZT* values are shown in Fig. 4.6a and b. With increasing temperature, *ZT* increases continuously. Ball milling and hot pressing method doesn't make too much difference in *ZT* for $EuZn_2Sb_2$. However, for $Ca_{0.25}Yb_{0.75}Zn_2Sb_2$, we obtained the highest *ZT* ~0.9 at 773 K, an improvement of ~50% that of the best reported sample by melting. The obtained enhancement is even more obvious for $YbZn_2Sb_2$ via ball milling, indicating adjusting electrical conductivity (*e.g.,* controlling vacancies) is very crucial in optimizing properties for the compounds especially within AZn_2Sb_2 system. In addition, given that the lattice thermal conductivity has been regarded as the only one independent material properties, in order to further increase *ZT*, it is important to optimize the electrical part to strike a balance between conflicting factor of high electrical conductivity and low electron thermal conductivity. It is very perspective that in order to further improve *ZT*, some effective small doping in Ca/Yb alloyed site would be useful by increasing electric conductivity and power

factor without sacrificing the low thermal conductivity.

Up to very recently, the conventional *ZT* and *PF* especially the peak *ZT* and *PF* have been used as the criteria to guide the thermoelectric materials performance. However, for thermoelectric devices that work at a large temperature difference, cumulative *ZT* and *PF* over the whole temperature range are more important, not the peak *ZT* and *PF*, in determining the possible efficiency and output power density, respectively. Recently, Kim *et al*. took another big step and proposed the engineering figure of merit $(ZT)_{eng}$ as a function of thermal boundaries, *i.e*., the temperatures of hot side T_h and cold side T_c to reliably predict the possible efficiency and output power density [30]. Fig. 4.7 shows the calculated $(ZT)_{eng}$ and $(PF)_{eng}$ dependence of the hot-side temperature up to 773 K while the cold-side temperature is kept at 323 K. It shows that the optimized sample $Ca_{0.25}Yb_{0.75}Zn_2Sb_2$ improves the materials' performance by 45% in terms of $(ZT)_{eng}$ over $CaZn_2Sb_2$. Compared with the same composition $Ca_{0.25}Yb_{0.75}Zn_2Sb_2$ prepared by melting, our sample $Ca_{0.25}Yb_{0.75}Zn_2Sb_2$ has $(ZT)_{eng}$ doubled. $EuZn_2Sb_2$ exhibits the highest $(PF)_{eng}$ ~0.86 W m^{-1} K^{-1}. Assuming T_c = 323 K and 2 mm of leg length, we have calculated the maximum efficiency η_{max} and its corresponding output power density P_d using $(ZT)_{eng}$ and $(PF)_{eng}$. The conversion efficiency of the optimized $Ca_{0.25}Yb_{0.75}Zn_2Sb_2$ is about 8.4% at ΔT = 450 °C, almost twice that of the similar composition by melting method. $EuZn_2Sb_2$ shows the best output power density of 2.1 W cm^{-2}.

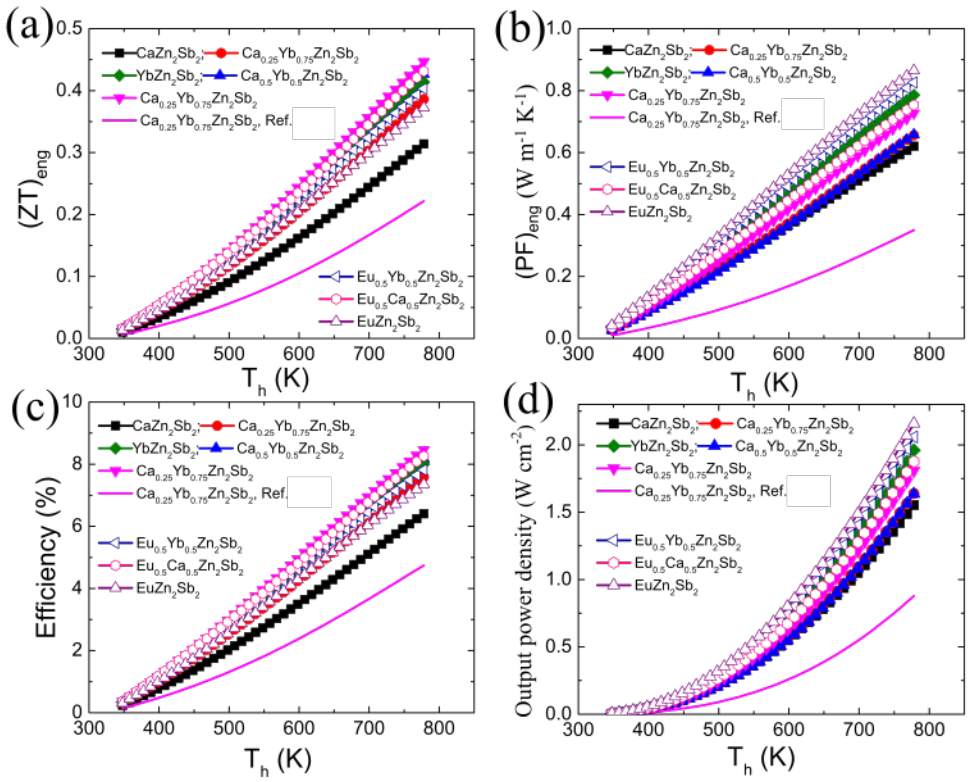

Figure 4.7 Calculated $(ZT)_{eng}$ (a) and $(PF)_{eng}$ (b) dependence of T_h up to 773 K and T_c at 323 K for $Ca_{1-x}Yb_xZn_2Sb_2$ (x = 0, 0.25, 0.5, 0.75, and 1), $EuZn_2Sb_2$, $Eu_{0.5}Ca_{0.5}Zn_2Sb_2$, and $Eu_{0.5}Yb_{0.5}Zn_2Sb_2$, efficiency (c) and output power density (d) as a function of hot side temperature. The data of the best performance of $Ca_{0.25}Yb_{0.75}Zn_2Sb_2$ from literature are included for comparison.

Ball milling and hot pressing has been demonstrated to be effective to fabricate high performance phase pure Zintl compounds AZn_2Sb_2, especially $Ca_{1-x}Yb_xZn_2Sb_2$ with enhanced thermoelectric properties. The larger carrier mobility in the rare-earth-alloyed compounds appears to be an inherent feature of these materials, but the experimentally measured smaller effective mass may also be a reason for the increased Hall mobility with

increasing Yb/Eu concentration in AZn_2Sb_2. The highest *ZT* value achieved is ~0.9 for x = 0.75 at 773 K, ~50% higher than the best of the sample made by melting method.

4.4 Reference

[1] Y. Z. Pei, X. Y. Shi, A. LaLonde, H. Wang, L. D. Chen, G. J. Snyder, *Nature* **2011**, 473, 66-69.

[2] Y. Z. Pei, A. LaLonde, S. Iwanaga, G. J. Snyder, *Energy Environ. Sci*. **2011**, 4, 2085-2089.

[3] X. Shi, J. Yang, J. R. Salvador, M. Chi, J. Y. Cho, H. Wang, S. Bai, J. Yang, W. Zhang, L. Chen, *J. Am. Chem. Soc*. **2011**, 133, 7837-7846.

[4] Q. Zhang, F. Cao, K. Lukas, W. S. Liu, K. Esfarjani, C. Opeil, D. Broido, D. Parker, D. J. Singh, G. Chen, Z. F. Ren, *J. Am. Chem. Soc*. **2012**, 134, 17731-17738.

[5] Q. Zhang, J. He, T. J. Zhu, S. N. Zhang, X. B. Zhao, T. M. Tritt, *Appl. Phys. Lett*. **2008**, 93, 102109

[6] H. Y. Chen, N. Savvides, T. Dasgupta, C. Stiewe, E. Mueller, *Phys. Status Solidi* A **2010**, 207, 2523-2531.

[7] W. S. Liu, X. J. Tan, K. Yin, H. J. Liu, X. F. Tang, J. Shi, Q. J. Zhang, C. Uher, *Phys. Rev. Lett.* **2012**, 108, 166601.

[8] M. Riffel, J. Schilz, *Scr. Metall. Mater*. **1995**, 32, 1951-1956.

[9] M. S. Toprak, C. Stiewe, D. Platzek, S. Williams, L. Bertini, E. Muller, C. Gatti, Y. Zhang, M. Rowe, M. Muhammed, *Adv. Funct. Mater.* **2004**, 14, 1189-1196.

[10] H. Wang, J. F. Li, C. W. Nan, M. Zhou, W. S. Liu, B. P. Zhang, T. Kita, *Appl. Phys. Lett*. **2006**, 88, 092104.

[11] W. S. Liu, B. P. Zhang, J. F. Li, H. L. Zhang, L. D. Zhao, *J. Appl. Phys*. **2007**, 102, 103717.

[12] X. Yan, B. Poudel, Y. Ma, W. S. Liu, G. Joshi, H. Wang, Y. C. Lan, D. Z. Wang, G. Chen, Z. F. Ren, *Nano Lett*. **2010**, 10, 3373-3378.

[13] Q. Jie, H. Wang, W. S. Liu, H. Wang, G. Chen, Z. F. Ren, *Phys. Chem. Chem. Phys*. **2013**, 15, 6809-6816.

[14] S. W. You, I. H. Kim, S. M. Choi, W. S. Seo, *J. Nanomater*. **2013**, 2013, 815925.

[15] B. Poudel, Q. Hao, Y. Ma, Y. C. Lan, A. Minnich, B. Yu, X. Yan, D. Z. Wang, A. Muto, D. Vashaee, X. Y. Chen, J. M. Liu, M. S. Dresselhaus, G. Chen, Z. F. Ren, *Science* **2008**, 320, 634-638.

[16] Q. Y. Zhang, H. Wang, W. S. Liu, H. Z Wang, B. Yu, Q. Zhang, Z. T. Tian, G. Ni, S. Lee, K. Esfarjani, G. Chen, Z. F. Ren, *Energy Environ. Sci*. **2012**, 5, 5246-5251.

[17] F. Gascoin, S. Ottensmann, D. Stark, S. M. Haile, G. J. Snyder, *Adv. Funct. Mater*. **2005**, 15, 1860-1864.

[18] H. Zhang, J. T. Zhao, Yu. Grin, X. J. Wang, M. B. Tang, Z. Y. Man, H. H. Chen, X. X. Yang, *J. Chem. Phys.* **2008**, 129, 164713.

[19] C. Yu, T. J. Zhu, S. N. Zhang, X. B. Zhao, J. He, Z. Su, Terry M. Tritt, *J. Appl. Phys*. **2008**, 104, 013705.

[20] X. J. Wang, M. B. Tang, H. H. Chen, X. X. Yang, J. T. Zhao, U. Burkhardt, Yu. Grin, *Appl. Phys. Lett*. **2009**, 94, 092106.

[21] E. S. Toberer, A. F. May, B. C. Melot, E. F. Larsen, G. J. Snyder, *Dalton Trans*. **2010**, 39, 1046-1054.

[22] A.F. May, M.A. McGuire, J. Ma, O. Delaire, A. Huq, R. Custelcean, *J. Appl. Phys*. **2012**, 111, 033708.

[23] A. Zevalkink, W.G. Zeier, E. Cheng,G. J. Snyder, J.P. Fleurial, S. Buxm, *Chem. Mater.* **2014**, 26, 5710.

[24] G. S. Pomrehn, A. Zevalkink, W. G. Zeier, A. van de Walle, G. J. Snyder, *Angew. Chem. Int. Ed.* **2014**, 53, 3422.

[25] C. Zheng, R. Hoffmann, R. Nesper, H.G. Von Schnering, *J. Am. Chem. Soc.* **1986**, 108, 1876-1884.

[26] J. P. Heremans, V, Jovovic, E. S. Toberer, A. Saramat, K. Kurosaki, A. Charoenphakdee, S. Yamanaka, G. J. Snyder, *Science* **2008**, 321, 554-557.

[27] J. P. Heremans, B. Wiendlocha, A. M. Chamoire, *Energy Environ. Sci*. **2012**, 5, 5510-5530.

[28] L. D. Zhao, S. H. Lo, J. Q. He, H. Li, K. Biswas, J. Androulakis, C. I. Wu, T. P. Hogan, D. Y. Chung, V. P. Dravid, M. G. Kanatzidis, *J. Am. Chem. Soc*. **2011**, 133, 20476-20487.

[29] V. I. Fistul, Heavily Doped Semiconductors, Plenum, New York **1969**.

[30] C. Wood, *Rep. Prog. Phys*. **1988**, 51, 459.

[31] H. S. Kim, W. S. Liu, G. Chen, C. W. Chu, Z. F. Ren, *Proc. Natl. Acad. Sci. U.S.A.* **2015**, 112, 8205-8210.

Chapter 5

P-type Layered Zintls with Na Doping

5.1 Introduction

Based on the dimensionless figure of merit (*ZT*), defined as $ZT = (S^2\sigma/\kappa)T$, an ideal thermoelectric material must have a power factor *PF* as high as possible and thermal conductivity κ as low as possible. Generally, the effective strategies of bulk nanostructuring, nanoscale secondary phase, complex crystal structure and solid solution are desirable for low thermal conductivity, which significantly increases the *ZT*s [1-3]. However, for practical use, high power factor is as important as efficiency when the capacity of the heat source is huge (such as solar heat), or the cost of the heat source is not a concern (such as waste heat from automobiles, steel industry, *etc.*) [4]. The output power density is mainly determined by the power factor in addition to the hear source temperature and geometry via the following formula:

$$\omega = \frac{1}{4}\frac{(T_h - T_c)^2}{L}PF \tag{5.1}$$

where ω, T_h, T_c, and L represent the output power density, hot side temperature, cold side temperature, and length of thermoelectric legs, respectively. The enhancements for power factor have been found possible through modification of carrier concentration, resonant state, band convergence, and energy barrier filtering [5,6].

The low efficiency, unavailability, and in some cases toxicity of good thermoelectric materials prevent thermoelectric generators from widely being applied in converting waste heat into electricity to make a real impact on environment [7]. Typically, the best thermoelectric materials are still Bi_2Te_3 [8,9] and Pb-Te-based materials [10], which contain heavy elements such as lead and tellurium that are toxic and not abundant. In the ongoing search for promising materials, the availability and cost of the raw elements need to be seriously considered. For example, Zintl compounds, formed between the alkali or alkaline-earth metals and the post-transition elements from group 13-15, have been shown to be promising candidates for thermoelectric materials due to their complex crystal structures, resulting in low lattice thermal conductivities. The layered structure Mg_3Sb_2, $CaZn_2Sb_2$, $CaMg_2Bi_2$, *ect*. are potentially good candidates due to their environmentally friendliness and earth-abundance as introduced in Chapter 1. Generally, good thermoelectric performance is found in doped semiconductors, so it is important to be able to control the carrier concentration in Zintl compounds via doping. For example, Na has been considered as an ideal hole dopant with little effect on the other physical properties in many materials, such as Na doping in $Ca_5Al_2Sb_2$ [11], Ca_3AlSb_3 [12], *etc.*

As discussed in Chapter 3, Bi-based Zintl phase $CaMg_2Bi_2$ has recently attracted some attention [13,14]. Using the ball milling and hot pressing method, we have achieved a competitive *ZT* value of ~0.8 in $CaMg_2Bi_2$ [15]. Further investigation demonstrated a 1% Bi deficiency ($CaMg_2Bi_{1.98}$) resulted in phase pure Zintl phase with a peak *ZT* of ~0.9. However, the carrier concentration of $CaMg_2Bi_{1.98}$ is relatively low (in the order of 10^{18} cm^{-3}), it is important to increase the carrier concentration through doping.

Another potential good p-type candidate is Mg_3Sb_2. However, due to the difficulties in synthesizing single phase by conventional synthesis routes, the highest reported *ZT* is just ~0.2 between 773 and 873 K, impeding by its high resistivity [16]. Recently, some progress was reported by Bhardwaj et al. [17,18]. They doped Bi in Sb site in the $Mg_3Sb_{2-x}Bi_x$ to enhance the *ZT* close to 0.6 at ~773 K and 10 at% Pb on Sb to improve *ZT* to 0.84 at ~773 K. However, the average *ZT* of the best composition $Mg_3Sb_{1.8}Bi_{0.2}$ is relatively low and Pb doping does not seem to be attractive due to the toxicity of Pb. In addition to doping in the Sb-site, Zn, Mn, Cd, *etc.* have been used to dope into the Mg site focusing on low temperature properties [19-21].

In this chapter, we explore the effect of doping Na into cation site on the thermoelectric transport properties in $Ca_{1-x}Na_xMg_2Bi_{1.98}$ and $Mg_{3-x}Na_xSb_2$, hoping to increase the carrier concentration for better electric property.

5.2 $Ca_{1-x}Na_xMg_2Bi_{1.98}$

Reproduced with permission from *Applied Physics Letters*, 108, 183901 (2016).

Fig. 5.1a shows the X-ray diffraction (XRD) patterns of $Ca_{1-x}Na_xMg_2Bi_{1.98}$ (x = 0, 0.0025, 0.005, and 0.0075). Na doped $Ca_{1-x}Na_xMg_2Bi_{1.98}$ show the same XRD patterns as the pure phase without noticeable peak position shift. All diffraction peaks are indexed with the reported $CaAl_2Si_2$ structure-type (trigonal, No. 164, P-3m1). The change in lattice

parameters is negligible with Na doping, attributed to the very small amount of dopant. By applying the Zintl concept, the structure of $CaMg_2Bi_{1.98}$ can be described as an anionic building block $(Mg_2Bi_2)^{2-}$ with divalent cations Ca^{2+} located between the chains to provide electrons. Na and Ca belong to alkali and alkaline earth metals, respectively, and show similar behaviors by donating electrons to the more electronegative anions $(Mg_2Bi_2)^{2-}$ and form covalent bonds. Increasing Na content effectively increases the carrier concentrations (discussed later). It can be concluded that Na is incorporated into the lattice in $Ca_{1-x}Na_xMg_2Bi_{1.98}$. The SEM image of the optimized $Ca_{0.995}Na_{0.005}Mg_2Bi_{1.98}$ sample is displayed in Fig. 5.1b, from which we can see that the sample is densely packed and the grain size varies from 100 to 500 nm.

To determine the effect of Na doping at the Ca site on the thermoelectric properties of $Ca_{1-x}Yb_xMg_2Bi_2$, electrical resistivity, Seebeck coefficient, and power factor were first measured. Fig. 5.2a illustrates the electrical resistivity as a function of temperature up to 873 K. The electrical resistivity of the Na doped samples is much smaller than that of the un-doped one, indicating Na is a very effective hole doner. At room temperature, the resistivity of sample with $x = 0.0075$ is around 9.2 μΩ m, which is about 15 time smaller compared to 131 μΩ m for the un-doped sample. The Hall carrier concentration at 300 K is shown in Table 5.1. Obviously, the carrier concentration has increased by more than one order of magnitude from 3.46×10^{18} cm^{-3} to 4.4×10^{19} cm^{-3}. With increasing Na content, Hall mobility experienced little change. Moreover, the relation for the resistivity dependence of temperature follows ρ vs. $T^{1.5}$ indicating that the carrier transport mechanism is dominated by acoustic phonon scattering before intrinsic excitation. For $x =$

0.75 at%, it is observed the resistivity exhibits a metal-like behavior, indicating the doping level is high enough to suppress the intrinsic excitation.

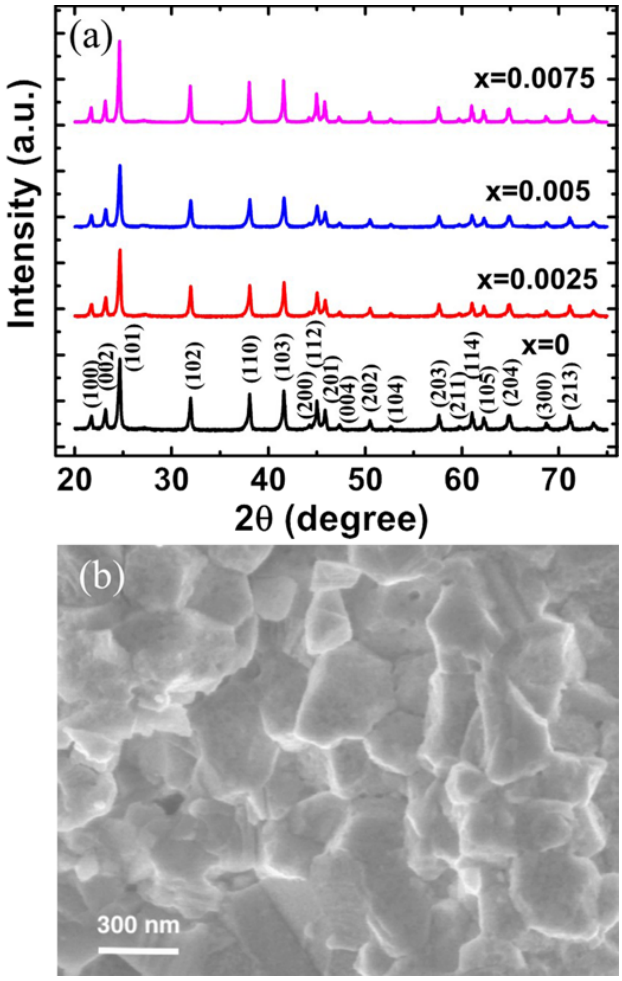

Figure 5.1 XRD patterns of $Ca_{1-x}Na_xMg_2Bi_{1.98}$ (x = 0, 0.0025, 0.005, and 0.0075) (a). SEM image of $Ca_{0.995}Na_{0.005}Mg_2Bi_{1.98}$ (b).

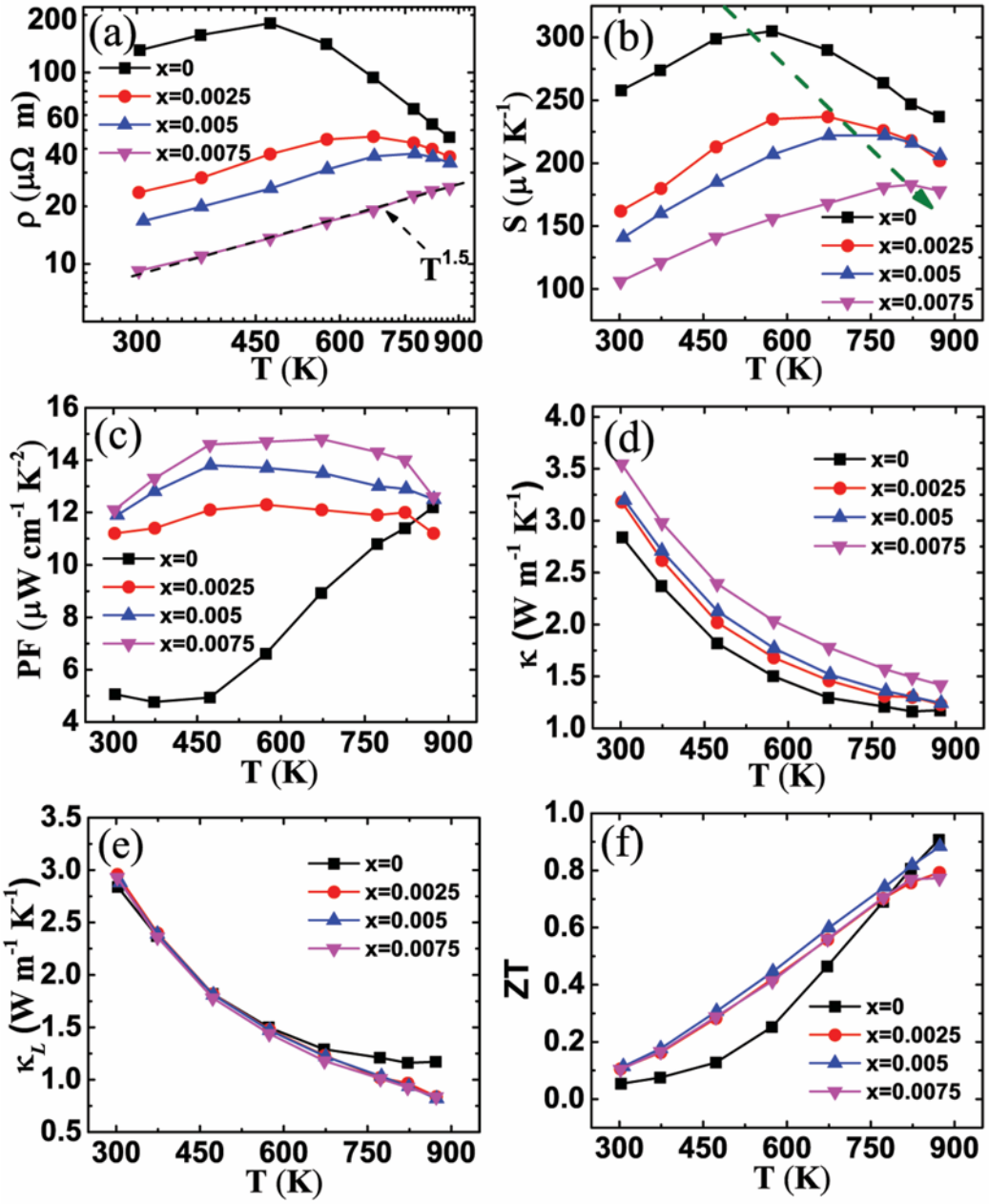

Figure 5.2 Temperature-dependent electrical resistivity (a), Seebeck coefficient (b), power factor (c), total thermal conductivity (d), lattice thermal conductivity (e) and *ZT* values (f) of $Ca_{1-x}Na_xMg_2Bi_{1.98}$ (x = 0, 0.0025, 0.005, and 0.0075).

Fig. 5.2b represents the temperature-dependent Seebeck coefficient of all the Na doped samples. The positive Seebeck coefficient indicates a p-type electrical transport behavior. Doping of Na into Ca sites decreases the Seebeck coefficient, and the decrease becomes smaller with Na content increases from 0.0025 to 0.0075. Meanwhile, all the samples exhibit peak values of the Seebeck coefficient, the typical characteristics of bipolar effect due to the very small band gap [13,22]. With more Na concentration, the temperature corresponding to peak Seebeck coefficient increases, indicating that the increased majority carrier concentration suppresses the bipolar effect.

Table 5.1 Room temperature thermoelectric transport properties of $Ca_{1-x}Na_xMg_2Bi_{1.98}$.

$Ca_{1-x}Na_xMg_2Bi_{1.98}$	$x = 0$	$x = 0.0025$	$x = 0.005$	$x = 0.0075$
Carrier concentration (10^{19} cm^{-3})	0.346	1.84	2.53	4.40
Hall mobility (cm^2 V^{-1} s^{-1})	138	144	147	154

Fig. 5.2c shows the power factor calculated from the measured electrical resistivity and Seebeck coefficient of $Ca_{1-x}Na_xMg_2Bi_{1.98}$ samples. With increasing Na concentration from $x = 0$ to 0.0075, power factor monotonically increases over the entire temperature range, especially at low temperatures. The power factor increases from 5 μW cm^{-1} K^{-2} for $x = 0$ to 12 μW cm^{-1} K^{-2} for $x = 0.0075$ at 300 K. Unlike the un-doped sample, all the Na doped samples maintain high power factors over all temperatures.

Fig. 5.2d shows the total thermal conductivity as a function of temperature for the $Ca_{1-x}Na_xMg_2Bi_{1.98}$ samples. The densities (ρ_D) of all the samples $Ca_{1-x}Na_xMg_2Bi_{1.98}$ with x = 0, 0.0025, 0.005, and 0.0075 measured by Archimedes method are 5.48, 5.50, 5.52, and 5.49 g cm^{-3}, respectively. All samples are densely packed, demonstrated by the SEM images taken on the freshly fractured surface. Specific heat (C_p) and the diffusivity (D) are used to calculate the total thermal conductivity (κ) of all the samples by using $\kappa = D\rho_D C_P$. The total thermal conductivity gradually increases with increasing Na doping concentration, mainly due to the enhanced contribution of electronic thermal conductivity κ_e, estimated using the Wiedemann−Franz relationship ($\kappa_e = LT/\rho$), where L is the Lorenz number, based on a single parabolic band model. By directly subtracting the electronic contribution from the total thermal conductivity, the lattice thermal conductivities (κ_L) were obtained and are shown in Fig. 5.2e. It is well known that the total thermal conductivity comprises three parts, including lattice thermal conductivity, electronic thermal conductivity, and bipolar thermal conductivity ($\kappa_{total} = \kappa_L + \kappa_e + \kappa_{bipol}$). In order to investigate the effect of Na substitution on the κ_L, the lattice thermal conductivity before the occurrence of intrinsic excitation (~550 K) are used to make the comparison. It is apparent that all samples exhibit almost the same value before 550 K, which means doping with Na at such a low concentration does not result in a significant scattering of the phonons.

The figure-of-merit ZT versus temperature and Na content x is plotted in Fig. 5.2f. With increasing temperature, ZT increases continuously. The Na doped samples have better ZT values when the temperature is below 750 K, mainly due to the improved power factor.

The optimized composition is $Ca_{0.995}Na_{0.005}Mg_2Bi_{1.98}$, which possesses the highest *ZT* over all temperatures and reaches a peak *ZT* of ~0.9 at 873 K.

Since *ZT* only indicates the ratio of electrical to thermal characteristics at each instantaneous temperature, it cannot indicate the practical efficiency of a TE material at a large temperature gradient between the cold and hot sides. Instead of using the peak *ZT*, Kim *et al*. recently took another big step and proposed the engineering figure of merit $(ZT)_{eng}$ as a function of thermal boundary conditions, *i.e*., the temperatures of hot side T_h and cold side T_c to reliably predict the possible efficiency and output power density. Fig. 5.3a and b show the calculated $(PF)_{eng}$ and ω_{max} and dependence of the hot side temperature up to 773 K while the cold side temperature is kept at 323 K. It is clear that both $(PF)_{eng}$ and ω_{max} increase more than 100% with Na doping concentration from $x = 0$ to 0.0075. Specifically, the un-doped sample exhibits a $(PF)_{eng}$ ~0.36 W m^{-1} K^{-1} and ω_{max} ~2.5 W cm^{-2} but the 0.0075 Na doped sample exhibits a $(PF)_{eng}$ ~0.77 W m^{-1} K^{-1} and ω_{max} ~5.3 W cm^{-2}. Fig. 5.3c and d present the hot side temperature dependence of $(ZT)_{eng}$ and efficiency, respectively. The calculated $(ZT)_{eng}$ increases from 0.23 for $x = 0$ to 0.4 for the optimized sample with $x = 0.005$, which makes the possible efficiency increase from 4.9% for $x = 0$ to 7.8% for $x = 0.005$ at $T_h = 873$ K.

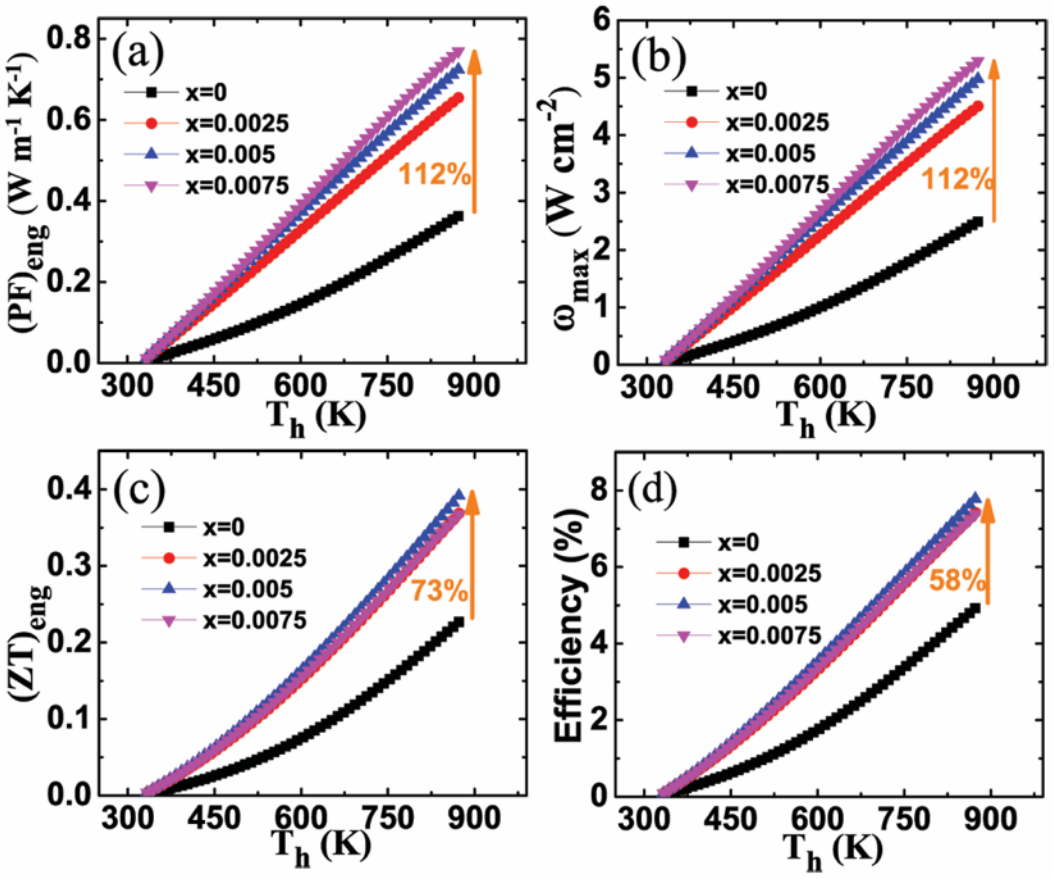

Figure 5.3 Engineering power factor (*PF*)eng dependence of hot side temperature (a), output power density ωmax (b), engineering figure of merit (*ZT*)eng (c), and efficiency of $Ca_{1-x}Na_xMg_2Bi_{1.98}$ (x= 0, 0.0025, 0.005, and 0.0075) (d).

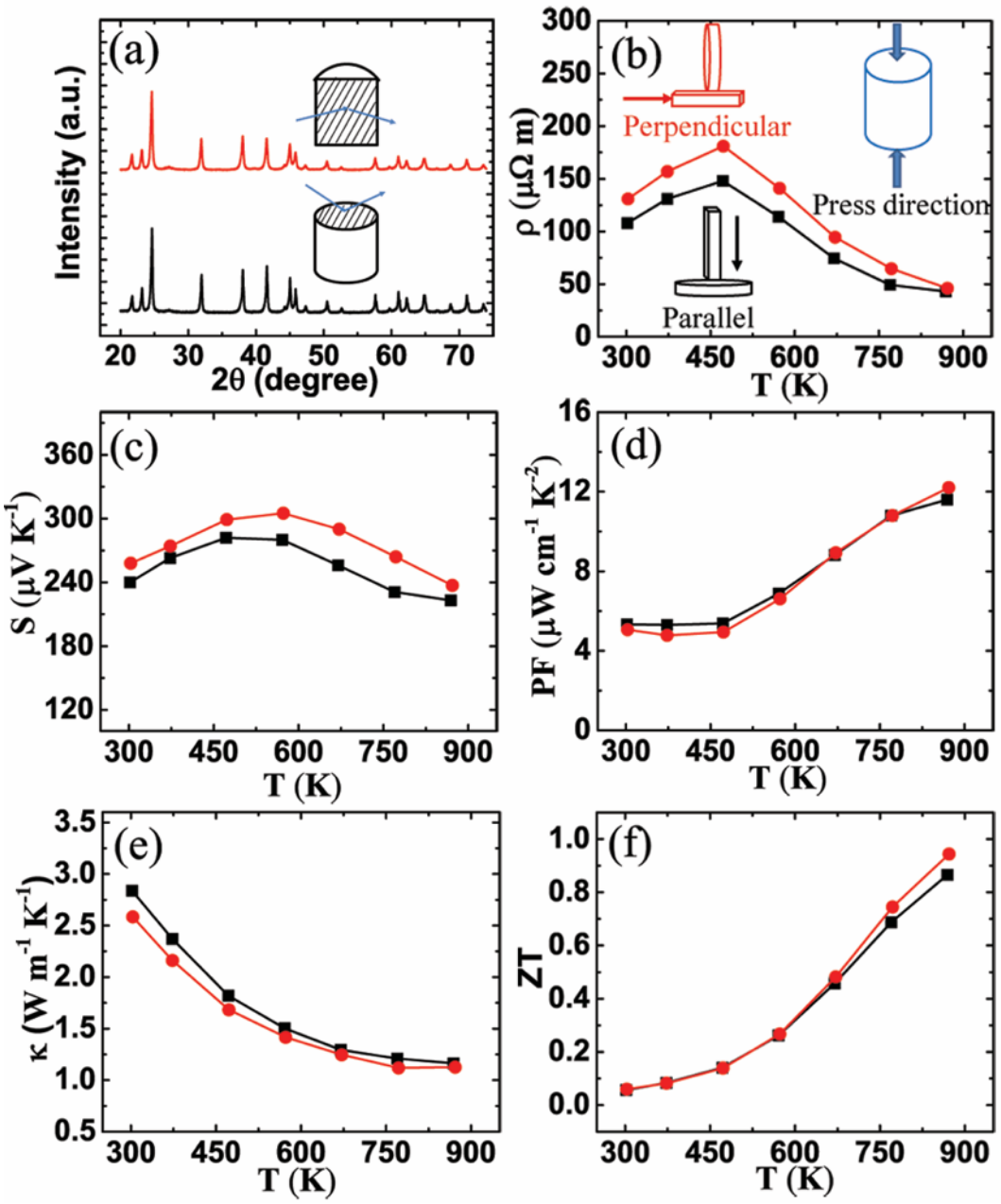

Figure 5.4 XRD patterns of planes perpendicular and parallel to the hot press direction of as-pressed $CaMg_2Bi_{1.98}$ sample (a). Thermoelectric properties of $CaMg_2Bi_{1.98}$ measured parallel and perpendicular to the hot press direction: (b) electrical resistivity, (c) Seebeck coefficient, (d) power factor, (e) thermal conductivity, and (f) *ZT*.

In order to investigate the anisotropy of the thermoelectric properties, thick un-doped $CaMg_2Bi_{1.98}$ samples were prepared. Fig. 5.4a a shows the very similar X-ray diffraction patterns from both planes perpendicular and parallel to the hot press direction, which might attribute to the uniform polycrystalline grains observed in the SEM image. Figs. 5.4b-f show the thermoelectric properties of $CaMg_2Bi_{1.98}$ measured in two different directions. The electrical resistivity and Seebeck coefficient measured perpendicular to the press direction is about 10% higher than parallel direction, indicating there is minor grain orientation. However, there in no much difference between the power factors measured from the two directions. Further due to the similar thermal conductivities in Fig. 5.4e, the *ZT* values in two directions are basically the same within the experimental errors ~10-12%. Therefore, the similar thermoelectric properties along the parallel and perpendicular to hot press direction shows that $CaMg_2Bi_{1.98}$ has little anisotropy.

The exploration of complex Zintl compounds continues to reveal good thermoelectric properties. Good thermoelectric properties are achieved in Bi-based Zintl compound $Ca_{1-x}Na_xMg_2Bi_{1.98}$ by doping Na into Ca to increase the carrier concentration and power factor. The optimized $Ca_{0.995}Na_{0.005}Mg_2Bi_{1.98}$ sample achieves better average *ZT*, output power density and efficiency. This work highlights the potential of Na doped $Ca_{1-x}Na_xMg_2Bi_{1.98}$ for potential waste heat recovery application for middle temperatures.

5.3 $Mg_{3-x}Na_xSb_2$

Reproduced with permission from *Acta Materialia*, 93, 187-193 (2015).

Sample Synthesis. Magnesium (Mg, Sigma Aldrich, 99.9%, pieces), sodium (Na, Sigma Aldrich, 99.9%, cubes), and antimony (Sb, Sigma Aldrich, 99.9%, chunks) were weighed according to the stoichiometry of $Mg_{3-x}Na_xSb_2$ with x = 0, 0.006, 0.0125, and 0.025, and then loaded in a stainless steel jar with stainless steel balls for mechanical alloying by a high-energy ball mill (SPEX 8000D) for 20 h. The final nanopowder was then loaded into a graphite die with an inner diameter of 12.7 mm, and consolidated by direct current (DC) hot pressing at ~1023 K for 2 min.

Results and discussion. Fig. 5.5 shows the XRD patterns of $Mg_{3-x}Na_xSb_2$ (x =0, 0.006, 0.0125, and 0.025). Na doped $Mg_{3-x}Na_xSb_2$ show the same XRD patterns as the pure phase without noticeable peak position shift. All diffraction peaks are indexed with the reported structure of inverse α-La_2O_3 structure-type. The change in lattice parameters is negligible with Na doping, which should attribute to the very small amount of dopant compared with other groups' prior work [17]. And according to the definition of Zintl compounds, Na and Mg, belonging to alkali and alkaline earth metals, respectively, show similar behaviors by donating electrons to the more electronegative anions Sb to form covalent bonds. Increasing Na content effectively increases carrier concentrations (discussed later). So it clearly demonstrates that Na atoms are successfully doped into Mg site.

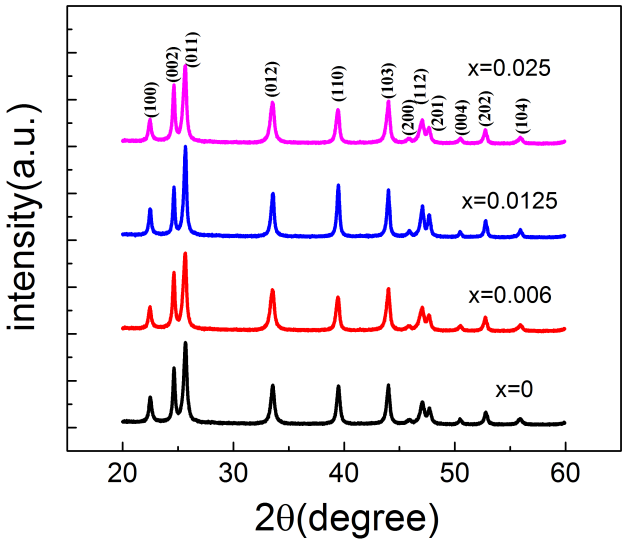

Figure 5.5 XRD patterns of $Mg_{3-x}Na_xSb_2$ (x = 0, 0.006, 0.0125, and 0.025).

The SEM image of the optimized $Mg_{2.875}Na_{0.0125}Sb_2$ sample is displayed in Fig. 5.6a, from which we can see that the sample is dense, consistent with the density measurement (discussed later). In order to confirm the grain size distribution and phase purity at microscopic scale, TEM investigation was carried out. Fig. 5.6b is a low-magnification TEM image, which shows the clear grain boundaries and grain sizes are about 1 μm. A selected area electron diffraction (SAED) pattern is recorded from one of these grains, shown in Fig. 5.6c. All of the spots in Fig. 5.6c can be successfully indexed according to *P*-3*m*1 hexagonal structure along the [130] zone axis with lattice parameters a = 4.56 Å and c = 7.23 Å which are consistent with the XRD data. Fig. 5.6d shows a high-resolution TEM image and elucidates three grains adjacent to each other sharing a triple junction with the presence of planes $01\bar{1}0$ (0.39 nm) and $10\bar{1}3$ (0.21 nm) of $Mg_{2.875}Na_{0.0125}Sb_2$. The micrograph, Fig. 5.6d, clearly reveals that each grain is truly single

crystalline with stacking of different planes and with random orientation with respect to each other.

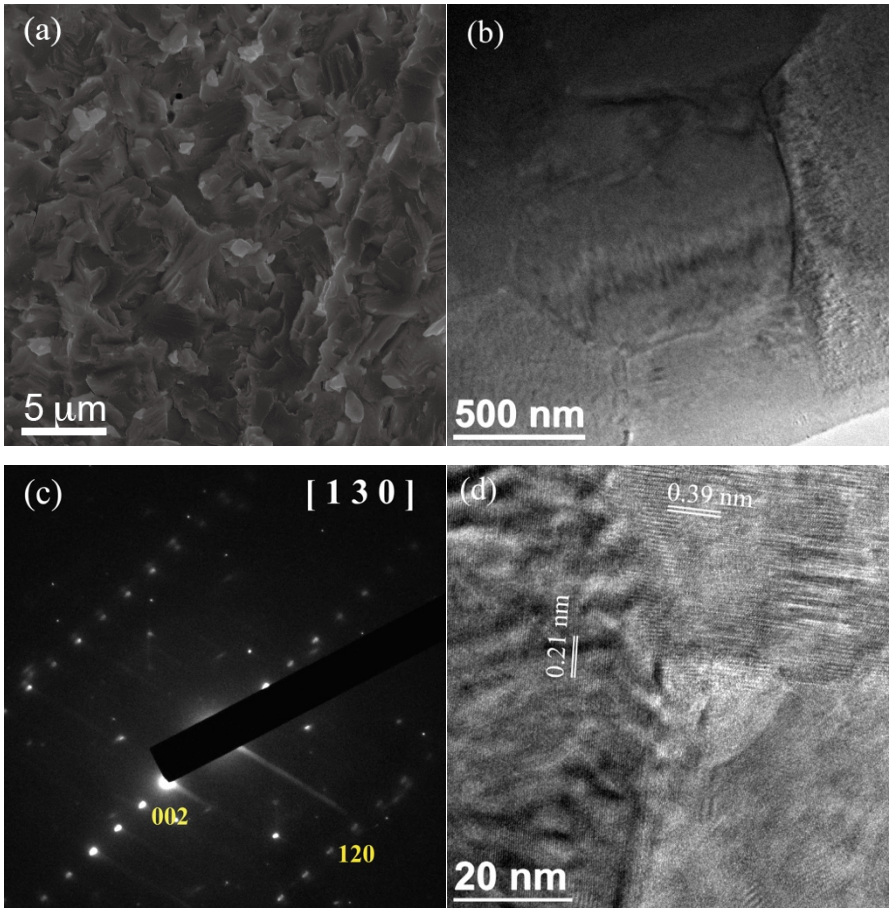

Figure 5.6 SEM and TEM images of sample $Mg_{2.9875}Na_{0.0125}Sb_2$: (a) SEM image; (b) medium magnification TEM image; (c) selected area electron diffraction (SAED) pattern; and (d) high resolution TEM image.

To determine the effect of Na doping on Mg site on the thermoelectric properties of $Mg_{3-x}Na_xSb_2$, electrical resistivity, Seebeck coefficient, and power factor were measured and shown in Fig. 5.7. Fig. 5.7a shows the electrical resistivity of all samples up to 773 K.

It clearly shows that the electrical resistivity of the doped samples is much smaller than that of the undoped one, which indicates that Na is a very effective hole dopant. To see the difference more clearly, Fig. 5.7b displays the temperature dependence of electrical resistivity for only the doped samples. The measured electrical resistivity of $Mg_{3-x}Na_xSb_2$ are 96.9, 46.8, and 29.0 μΩ m for x = 0.006, 0.0125, and 0.025 at room temperature, respectively, which are almost four orders of magnitude lower than that of Mg_3Sb_2. With increasing temperature, the electrical resistivity decreases drastically for Mg_3Sb_2 (x = 0), corresponding to a strong semiconducting behavior. However, the electrical resistivity of Na doped samples decreases to a minimum around 473 K and then increases, which indicates that Na substitution for Mg changes the semiconducting behavior to metallic behavior. Increasing Na concentration in Mg_3Sb_2 leads to lower electrical resistivity due to the enhanced carrier concentration as listed in Table 5.2. The carrier concentration remarkably increases with x. The carrier concentration (n) and Hall mobility (μ) listed in Table 5.2 affect the electrical resistivity (ρ) by the relationship $1/\rho = ne\mu$. With increasing Na content, Hall mobility decreases due to stronger electron scattering by Na, which means the carrier concentration primarily dominates the electronic transport.

Fig. 5.7c represents the temperature-dependent Seebeck coefficient of all the Na doped samples. Doping of Na into Mg site dramatically decreases the Seebeck coefficient and a slight decrease in Seebeck coefficient with increasing Na content is also observed. We can use the relation $E_g = 2eT_{max}S_{max}$ for better understanding of the energy gaps where E_g, S_{max}, and T_{max} are the band gap, the maximum value of the Seebeck coefficient, and the temperature at the S_{max}, respectively. E_g of all the samples $Mg_{3-x}Na_xSb_2$ with x = 0, 0.006,

0.0125, and 0.025 were estimated to be 0.61, 0.35, 0.30, and 0.24 eV, respectively. Thus, E_g of Na doped composition was estimated to be more than 50% lower than that of Mg_3Sb_2, indicating Na is very effective in modifying the band gap.

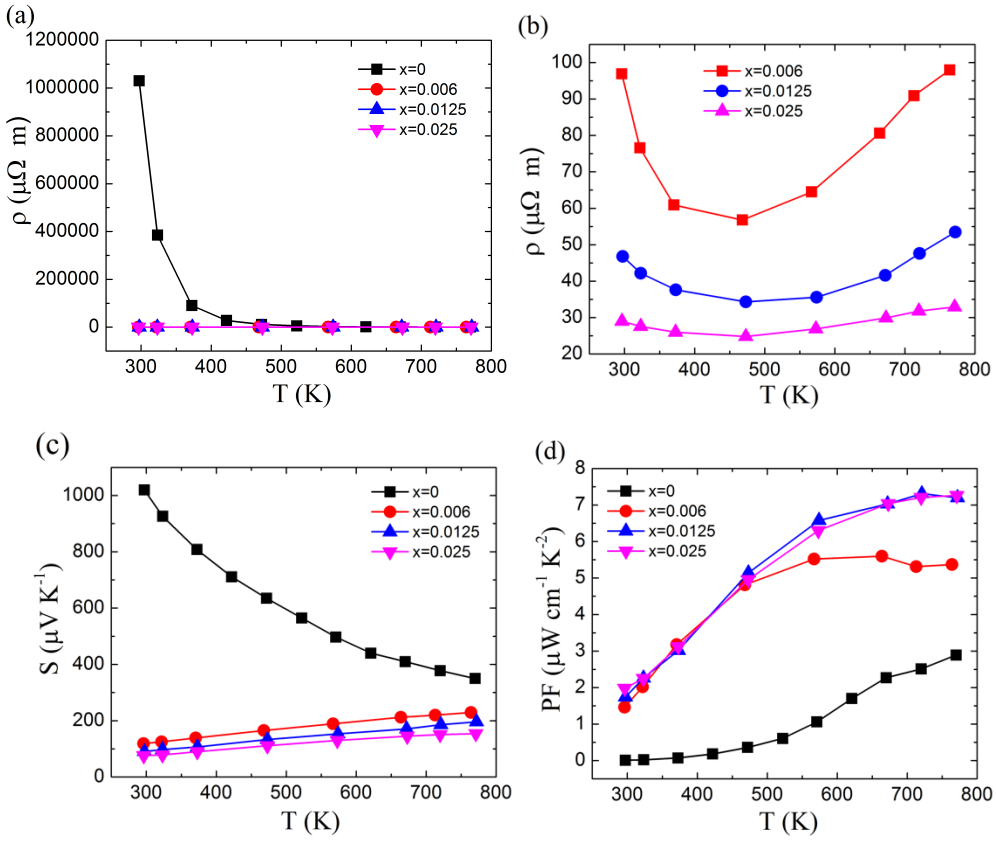

Figure 5.7 Temperature-dependent thermoelectric properties of $Mg_{3-x}Na_xSb_2$ (x = 0, 0.006, 0.0125, and 0.025): (a) electrical resistivity; (b) electrical resistivity of the doped samples; (c) Seebeck coefficient; and (d) power factor.

Table 5.2 Carrier concentration and Hall mobility at room temperature of $Mg_{3-x}Na_xSb_2$ (x = 0, 0.006, 0.0125, and 0.025).

$Mg_{3-x}Na_xSb_2$	x = 0	x = 0.006	x = 0.0125	x = 0.025
Carrier concentration (10^{19} cm^{-3})	0.00026	3.87	8.41	17.1
Hall mobility (cm^2 V^{-1} s^{-1})	23.2	16.7	15.9	12.6

Combining the electrical resistivity and Seebeck coefficient, the power factor of all Na doped samples are shown in Fig. 5.7d. Although the power factor of Na doped samples is much higher than that of the undoped Mg_3Sb_2, they are still very low as compared to other good materials. The power factor of all the Na doped samples shows no difference when temperature is below 473 K, while with increasing temperature, the power factors for x = 0.0125 and 0.025 continue to grow, but saturate at about 7.5 μW cm^{-1} K^{-2}.

Fig. 5.8 shows the temperature-dependent thermal transport behavior of $Mg_{3-x}Na_xSb_2$ with x = 0, 0.006, 0.0125, and 0.025. Specific heat (C_p) of $Mg_{2.975}Na_{0.025}Sb_2$, shown in Fig. 5.8a, is used for all samples since Na has a higher C_p than Mg. The C_p dependence of temperature shows a little bit increase towards 773 K, while at room temperature C_p is 0.4, almost the same as the calculated value based on Dulong-Petit Law. The diffusivity (D) of all samples $Mg_{3-x}Na_xSb_2$ is shown in Fig. 5.8b, clearly the higher the Na concentration the higher the diffusivity. C_p and D are used to calculate the total thermal conductivity (κ) of all the doped samples by using $\kappa = D\rho C_p$, where ρ is the measured

density of samples. The densities of all the samples $Mg_{3-x}Na_xSb_2$ with x = 0, 0.006, 0.0125, and 0.025 measured by Archimedes method are 4.007, 3.996, 3.997, 3.985 g cm^{-3}, respectively, ~98% of the theoretical density 4.088 g cm^{-3}. The temperature dependence of the total thermal conductivity (κ) of Na doped samples is plotted in Fig. 5.8c. The total thermal conductivity for Na doped Mg_3Sb_2 is higher than that of Mg_3Sb_2 due to the higher electrical conductivity. The thermal conductivity of all samples decreases with temperature.

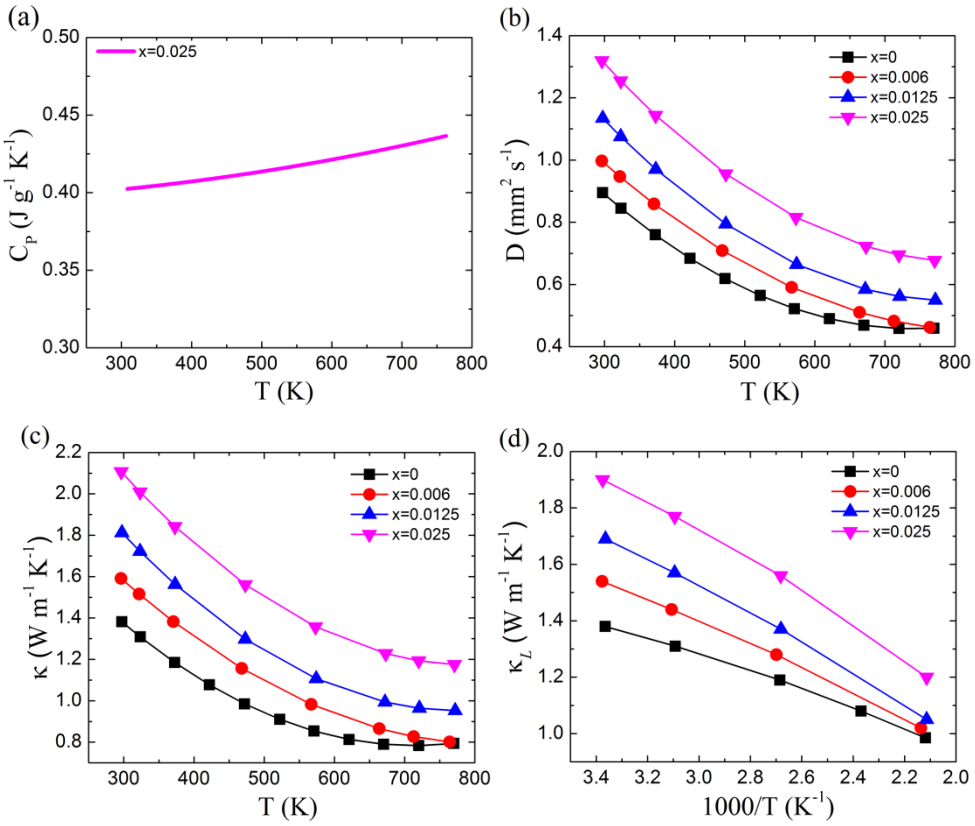

Figure 5.8 Temperature-dependent thermal transport properties of $Mg_{3-x}Na_xSb_2$ (x = 0, 0.006, 0.0125, and 0.025): (a) Specific heat; (b) thermal diffusivity; (c) total thermal conductivity; and (d) lattice thermal conductivity.

To better understand the phonon scattering, we calculated the lattice thermal conductivity by subtracting the electronic contribution from the total thermal conductivity. The electronic thermal conductivity (κ_e) can be calculated using the Wiedemann-Franz relation given by $\kappa_e = L\sigma T$, where L is Lorenz number, σ is the electrical conductivity, and T is the absolute temperature. For most thermoelectric materials, the Lorenz number depends on the reduced Fermi energy $\xi = E_f/k_BT$ and scattering parameter r as shown in the following,

$$L = \left(\frac{k_B}{e}\right)^2 \left(\frac{(r+7/2)F_{r+5/2}(\xi)}{(r+3/2)F_{r+1/2}(\xi)} - \left[\frac{(r+5/2)F_{r+3/2}(\xi)}{(r+3/2)F_{r+1/2}(\xi)}\right]^2 \right) \tag{5.2}$$

where F_n is the Fermi integral given by

$$F_n(\xi) = \int_0^\infty \frac{\chi^n}{1+e^{\chi-\xi}} d\chi \tag{5.3}$$

The reduced Fermi energy can be deduced from the Seebeck coefficient on the basis of single band approximation,

$$S = \pm \frac{k_B}{e} \left(\frac{(r+5/2)F_{r+3/2}(\xi)}{(r+3/2)F_{r+1/2}(\xi)} - \xi \right) \tag{5.4}$$

In this calculation, we assumed acoustic phonon scattering as the main carrier scattering mechanism using r = -0.5. By subtracting the electronic contribution from the total thermal conductivity, the inversely temperature dependence of lattice thermal conductivity (κ_L) is shown in Fig. 5.8d. It is noted that this method is not accurate enough to estimate κ_L, so only κ_L near low temperature is calculated. The relationship between κ_L and the reciprocal of temperature ($1/T$) is almost linear, which reveals the predominant phonon contribution to the thermal conductivity. Clearly, the lattice thermal conductivity is not reduced by

doping but increased, opposite to the normal trend. Typically, impurities produce point defect scattering and thereby reduce the lattice thermal conductivity. Thus, some other scattering mechanisms should be dominant instead of point defect scattering. In fact, the phenomenon of increasing lattice thermal conductivity has been observed in some other doped semiconductors, like $Mo_3Sb_{7-x}Te_x$ [23]. Here, we will also assume the lattice thermal conductivity is dominated by the Umklapp scattering and ignore the point defect influence. In addition, the lattice thermal conductivity of Mn doped Mg_3Sb_2 did not decrease either [21]. One possible reason is that Mn substitutes for Mg in the tetrahedral site rather than in the octahedral site of Mg^{2+} cation layer, and most phonon heat transfer occurs in the Mg^{2+} cation layer. The real reason why lattice thermal conductivity increase deserves further studies.

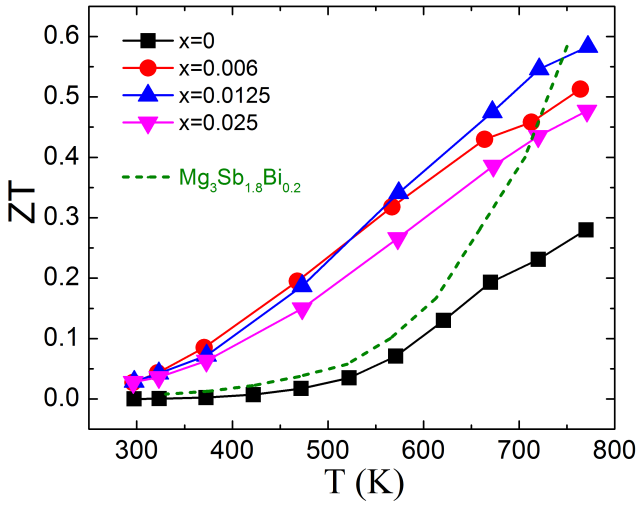

Figure 5.9 Temperature-dependent *ZT* for $Mg_{3-x}Na_xSb_2$ (x = 0, 0.006, 0.0125, and 0.025). The temperature-dependent *ZT* for $Mg_3Sb_{1.8}Bi_{0.2}$ is also plotted for comparison [17].

We have also calculated *ZT* from the measured electrical resistivity, thermal conductivity, as well as the Seebeck coefficient, and plotted the *ZT* results in Fig. 5.9. The maximum *ZT* for Mg_3Sb_2 was observed to be about 0.3 at 773 K which is higher than most of the reported data by other groups [16-18]. The optimum doping of Na with 1.25 at% in Mg_3Sb_2 drives the system to exhibit an increased *ZT* of ~0.6 at 773 K. For all the Na doped samples, *ZT* increases almost linearly with temperature and the average *ZT* is much better than prior work Bi doped Mg_3Sb_2 as shown in the figure. The enhanced *ZT* is resulted from the increase in power factor. From the peak *ZT* values shown in Fig. 5.9, it seems that 1.25 at% Na-doped Mg_3Sb_2 is the best material among the three compositions. However, *ZT* indicates the ratio of electrical to thermal characteristics only at each instantaneous temperature, so it cannot indicate the practical efficiency of a TE material at a large temperature gradient of its actual operations. Instead of using the peak *ZT*, Kim et al. proposed the engineering dimensionless figure of merit $(ZT)_{eng}$ as a function of thermal boundaries, *i.e.*, the temperatures of hot side T_h and cold side T_c, which is defined as [24],

$$(ZT)_{eng} = \frac{\left(\int_{T_c}^{T_h} S(T)\,dT\right)^2}{\int_{T_c}^{T_h} \rho(T)\,dT \int_{T_c}^{T_h} \kappa(T)\,dT}\left(T_h - T_c\right) = \frac{\left(PF\right)_{eng}}{\int_{T_c}^{T_h} \kappa(T)\,dT}\left(T_h - T_c\right) \qquad (5.5)$$

where $S(T)$, $\rho(T)$, and $\kappa(T)$ are temperature-dependent thermoelectric properties, and $(PF)_{eng}$ is the engineering power factor with respect to the boundary temperatures. $(ZT)_{eng}$ implies the cumulative effect of TE properties at a given thermal boundary. $(PF)_{eng}$ has unit of W m^{-1} K^{-1}, different from the conventional unit of W m^{-1} K^{-2} due to its cumulative effect associated with the temperature gradient. Fig. 5.10 shows the calculated $(ZT)_{eng}$ and $(PF)_{eng}$ dependence of the hot side temperature up to 773 K while the cold side temperature

is kept at 323 K. It is noted that this study improves the materials' performance by a factor of 40 in terms of $(ZT)_{eng}$ as compared with Mg_3Sb_2 and by a factor of 4 as compared with Bi doped Mg_3Sb_2 at the same conditions (Fig. 5.10a). Based on $(ZT)_{eng}$, 0.6 at% Na-doped Mg_3Sb_2 shows similar performance to 1.25 at% Na-doped Mg_3Sb_2 at T_h = 773 K even though the peak ZT of the latter at that temperature is 14% higher than the former. In addition, 0.6 at% Na-doped Mg_3Sb_2 shows higher $(ZT)_{eng}$ through whole temperature range below T_h = 723 K at T_c = 323 K. Thus, 0.6 at% Na-doped Mg_3Sb_2 is slightly better in terms of the efficiency when the temperature difference is limited below 400 K at T_c = 323 K while 1.25 at% Na-doped Mg_3Sb_2 should be selected if larger electric power generation is more concerned since power factor is dominant on power output (Fig. 5.10b).

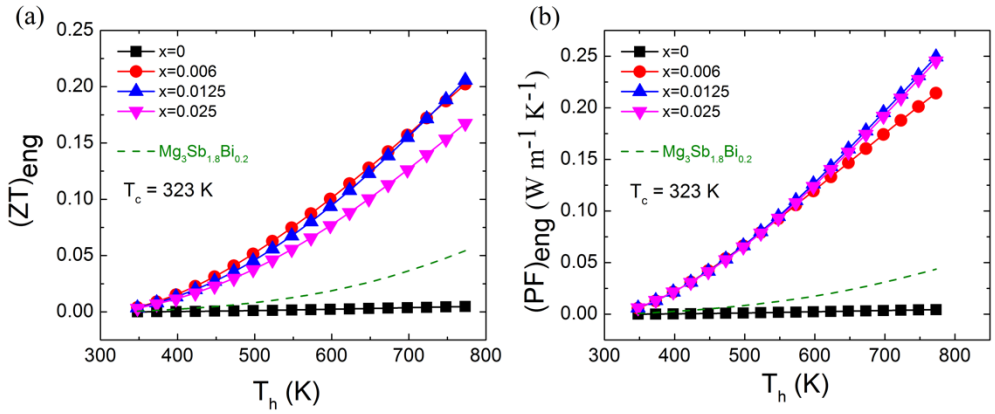

Figure 5.10 Calculated $(ZT)_{eng}$ and $(PF)_{eng}$ dependence of the hot side temperature up to 773 K while the cold side temperature is kept at 323 K for $Mg_{3-x}Na_xSb_2$ (x = 0, 0.006, 0.0125, and 0.025). The Calculated $(ZT)_{eng}$ and $(PF)_{eng}$ of $Mg_3Sb_{1.8}Bi_{0.2}$ are also plotted for comparison.

Nanostructured Zintl phase of Mg_3Sb_2 and Na doped $Mg_{3-x}Na_xSb_2$ were synthesized successfully by ball milling and hot pressing. Na doping into Mg enhances the power factor by increasing carrier concentration but not decreasing the carrier mobility much. A peak

ZT of ~0.6 at 773 K has been achieved for the optimum doping with $x = 0.0125$. Mg_3Sb_2 based Zintl compounds free of expensive rare earth elements have advantages of low cost, environmentally friendly, and non-toxicity.

5.4 Reference

[1] J. Yang, G. P. Meisner, L. Chen, *Appl. Phys. Lett.* **2004**, *85*, 1140–4.

[2] H. Xie, H. Wang, Y. Pei, C. Fu, X. Liu, G. J. Snyder, X. Zhao, T. Zhu, *Adv. Funct. Mater.* **2013**, *23*, 5123–5130.

[3] J. He, M. G. Kanatzidis, V. P. Dravid, *Materials Today* **2013**, *16*, 166–176.

[4] W. Liu, H. S. Kim, S. Chen, Q. Jie, B. Lv, M. Yao, Z. Ren, C. P. Opeil, S. Wilson, C.-W. Chu, et al., *Proc Natl Acad Sci USA* **2015**, *112*, 3269–3274.

[5] Y. Pei, H. Wang, G. J. Snyder, *Adv. Mater.* **2012**, *24*, 6125–6135.

[6] Z. Liu, Y. Wang, J. Mao, H. Geng, J. Shuai, Y. Wang, R. He, W. Cai, J. Sui, Z. Ren, *Adv. Energy Mater.* **2016**, *6*, 1502269.

[7] W. Liu, Q. Jie, H. S. Kim, Z. Ren, *Acta Materialia* **2015**, *87*, 357–376.

[8] B. Poudel, Q. Hao, Y. Ma, Y. Lan, A. Minnich, B. Yu, X. Yan, D. Wang, A. Muto, D. Vashaee, et al., *Science* **2008**, *320*, 634–638.

[9] X. Yan, B. Poudel, Y. Ma, W. S. Liu, G. Joshi, H. Wang, Y. Lan, D. Wang, G. Chen, Z. F. Ren, *Nano Lett.* **2010**, *10*, 3373–3378.

[10] Q. Zhang, F. Cao, W. Liu, K. Lukas, B. Yu, S. Chen, C. Opeil, D. Broido, G. Chen, Z. Ren, *J. Am. Chem. Soc.* **2012**, *134*, 10031–10038.

[11] E. S. Toberer, A. Zevalkink, N. Crisosto, G. J. Snyder, *Adv. Funct. Mater.* **2010**, *20*, 4375–4380.

[12] A. Zevalkink, E. S. Toberer, W. G. Zeier, E. Flage-Larsen, G. J. Snyder, *Energy & Environmental Science* **2011**, *4*, 510–518.

[13] A. F. May, M. A. McGuire, D. J. Singh, R. Custelcean, G. E. Jellison Jr., *Inorg.*

Chem. **2011**, *50*, 11127–11133.

[14] A. F. May, M. A. McGuire, D. J. Singh, J. Ma, O. Delaire, A. Huq, W. Cai, H. Wang, *Phys. Rev. B* **2012**, *85*, 035202–10.

[15] J. Shuai, Z. Liu, H. S. Kim, Y. Wang, J. Mao, R. He, J. Sui, Z. Ren, *J. Mater. Chem. A* **2016**, *4*, 4312–4320.

[16] C. L. Condron, S. M. Kauzlarich, F. Gascoin, G. J. Snyder, *Journal of Solid State Chemistry* **2006**, *179*, 2252–2257.

[17] A. Bhardwaj, A. Rajput, A. K. Shukla, J. J. Pulikkotil, A. K. Srivastava, A. Dhar, G. Gupta, S. Auluck, D. K. Misra, R. C. Budhani, *RSC Advances* **2013**, *3*, 8504–13.

[18] A. Bhardwaj, D. K. Misra, *RSC Advances* **2014**, *4*, 34552–34560.

[19] H. X. Xin, X. Y. Qin, J. H. Jia, C. J. Song, K. X. Zhang, J. Zhang, *J. Phys. D: Appl. Phys.* **2009**, *42*, 165403–10.

[20] K. X. Zhang, X. Y. Qin, H. X. Xin, H. J. Li, J. Zhang, *Journal of Alloys and Compounds* **2009**, *484*, 498–504.

[21] S. Kim, C. Kim, Y.-K. Hong, T. Onimaru, K. Suekuni, T. Takabatake, M.-H. Jung, *J. Mater. Chem. A* **2014**, *2*, 12311–6.

[22] J. Zhang, L. Song, K. F. F. Fischer, W. Zhang, X. Shi, G. K. H. Madsen, B. B. Iversen, *Nature Communications* **2016**, *7*, 1–7.

[23] X. Shi, Y. Pei, G. J. Snyder, L. Chen, *Energy Environ. Sci.* **2011**, *4*, 4086.

[24] H. S. Kim, W. Liu, G. Chen, C.-W. Chu, Z. Ren, *Proc Natl Acad Sci USA* **2015**, *112*, 8205–8210.

Chapter 6

N-type Mg_3Sb_2-based Zintl Phase

6.1 Introduction

Thermoelectric generators typically consist of both n- and p- type legs, which should ideally be made of same materials from thermal stress and device processing considerations [1]. However, through several decades' efforts, it still remains very difficult to make competitive n-type Zintl materials or convert the existed p-type Zintls into n-type. The good Zintl compounds are p-type only so far. The Zintl phases AB_2X_2 (A = Ca, Yb, Eu, Sr; B = Zn, Mn, Cd, Mg; *X* = Sb, Bi) [2-9] crystallizing in $CaAl_2Si_2$ structure are an extreme example with a high p-type carrier concentration of 10^{19} to10^{20} cm^{-3}. One possible explanation of the observed p-type conductivity could be vacancies on the electron-donating A cation sites, as might be expected in most Zintl phases [8,10,11]. The density function theory calculation has also predicated the A-site are most energetically favorable for point defects and the concentration of vacancies depends strongly on the electronegativity of A [10]. Presumably, alloying with electropositive trivalent impurities on A site would provide compensation or n-type carrier concentration if it can be achieved. This assumption has been only reported in Mn doped Mg_3Sb_2 with relative low carrier concentration (~10^{18} cm^{-3}) and less competitive TE performance (ZT < 0.1 at 500 K) [12], but never into n-type.

The A = B = Mg antimonide, Mg_3Sb_2 has been studied for several years as p-type thermoelectric material with moderate TE performance (ZT ~0.3 at 773 K) [13,14]. Although crystallizing in the same structure type, the extremely high resistivity (~ 1 Ω m at 300 K) and low carrier concentration (~10^{15} cm^{-3}) of the stoichiometric Mg_3Sb_2, significantly different from other ternary Zintls (*e.g.*, 10^{19} cm^{-3} for $YbZn_2Sb_2$) [8,11], make it possible toward the realization of n-type carrier conduction. Very recently, a report from Panasonic showed a surprisingly n-type thermoelectric performance with ZT of 1.5 in $Mg_{3.2}Sb_{1.5}Bi_{0.49}Te_{0.01}$ [15]. The extra Mg is the reason for n-type property, Te is for further carrier concentration increase, and Bi is for decreasing the lattice thermal conductivity. However, the electrical conductivity is low, especially at lower temperature, which motivates us to further improve it.

In this chapter, we report that Nb is effective on increasing the electrical conductivity. When partially substituting Mg with Nb, as $Mg_{3.2-x}Nb_xSb_{1.5}Bi_{0.49}Te_{0.01}$, we not only enhanced the electrical conductivity and Seebeck coefficient but also decreased the thermal conductivity, resulting in higher power factor with higher ZT values across all the temperature range. The calculated ideal device efficiency is 14 % operating between 500 °C and 50 °C, which is higher than any of the existing materials in this temperature range.

6.2 Sample Preparation and Computational Methods

Sample Preparation. Magnesium (Mg, Sigma Aldrich, 99.9%, pieces), niobium (Nb, Sigma Aldrich, 99.9%, powder), bismuth (Bi, Sigma Aldrich, 99.999%, chunks), tellurium (Te, Sigma Aldrich, 99.999%, chunks), and antimony (Sb, Sigma Aldrich, 99.999%, chunks) were weighed according to the stoichiometry of $Mg_{3.2-x}Nb_xSb_{1.5}Bi_{0.49}Te_{0.01}$ (x = 0, 0.05, 0.1, and 0.15), and sealed directly in the stainless steel jar with stainless steel balls inside an argon-filled glove box. Then the sealed jar was taken out for mechanical alloying by a high-energy ball mill (SPEX 8000D) for 10 h. The obtained final nanopowder was then loaded into a graphite die with an inner diameter of 12.7 mm, and consolidated by hot pressing at ~923 K for 2 min. The final hot pressed samples were cut and polished to the required dimensions for characterizations.

Computational Methods. Our first-principles calculations were carried out using the linearized augmented planewave (LAPW) method [16] as implemented in the WIEN2K code [17]. We used experimental lattice constants (a = 4.559 Å, c = 7.243 Å) [18] and the internal coordinates are relaxed within the energy minimization using generalized gradient approximation (GGA) of Perdew, Burke, and Ernzerhof (PBE) functional [19]. The electronic structures are obtained using modified Becke-Johnson (mBJ) potential including spin-orbit coupling [20]. The LAPW sphere radii were 2.4 bohr for Mg and 2.6 bohr for Sb. The transport functions and coefficients are obtained using Boltzmann transport theory based on first-principles electronic structure. This is within the constant scattering time approximation (CSTA) as implemented in the Bolt*z*TraP code [21]. For n-type Mg_3Sb_2, the

relaxation time τ and lattice thermal conductivity were derived by fitting experimental data on $Mg_{3.2}Bi_{0.49}Sb_{1.5}Te_{0.01}$ sample at high temperature (771 K). The experimental conductivity shows non-monotonic behavior that might be because of the effective carrier concentration changes.

6.3 Effect of Interstitial Mg in Mg_3Sb_2-based Zintls and Comparison between P- and N-type

Fig. 6.1a shows the measured Seebeck coefficient of $Mg_{3+x}Sb_2$. As can be seen, the extra Mg is crucial to realize the n-type conduction before further optimizing the doping level. When the extra Mg content x in $Mg_{3+x}Sb_2$ increases from 0.1 to 0.2, the Seebeck coefficient becomes negative over the entire temperature range (Fig. 6.1a). Further increasing x content to 0.3 leads to a little decreasing in the absolute Seebeck coefficient, indicating the maximum amount of extra Mg in the lattice is less than 0.3. Specifically, near room temperature, the highest Seebeck coefficient reaches -500 $\mu V\ K^{-1}$ in $Mg_{3.2}Sb_2$ sample with very low carrier concentration (~10^{14} cm^{-3}). In order to optimize the properties, Tamaki *et al*. reported that Bi substitution on Sb site can lead to a significant reduction in the lattice thermal conductivity but with almost unchanged carrier concentration and carrier mobility. Besides, Te was chosen to be an effective electron donor for better electronic transport properties. Highest *ZT* ~1.5 was observed in $Mg_{3.2}Sb_{1.5}Bi_{0.49}Te_{0.01}$, in a very good agreement with what was reported even though the individual properties are slightly diferent[33], much better than the corresponding optimized p-type cases (*e.g.*, *ZT* ~0.9 in Pd-doped Mg_3Sb_2, *ZT* ~0.6 in Na-doped Mg_3Sb_2) [14,22].

The decreasing Seebeck coefficient with increasing temperature is a typical sign of bipolar effect, which is much stronger in the p-type. The calculated transport coefficients are depicted in Fig. 6.1b-c, and constant energy surfaces are shown in Fig. 6.2. The better performance in n-type partially comes from the multi-pocket character of the bands near conduction band minimum, as shown in Fig. 6.2. This feature leads to larger density of states effective mass, larger Seebeck coefficient, and higher power factor for n-type materials.

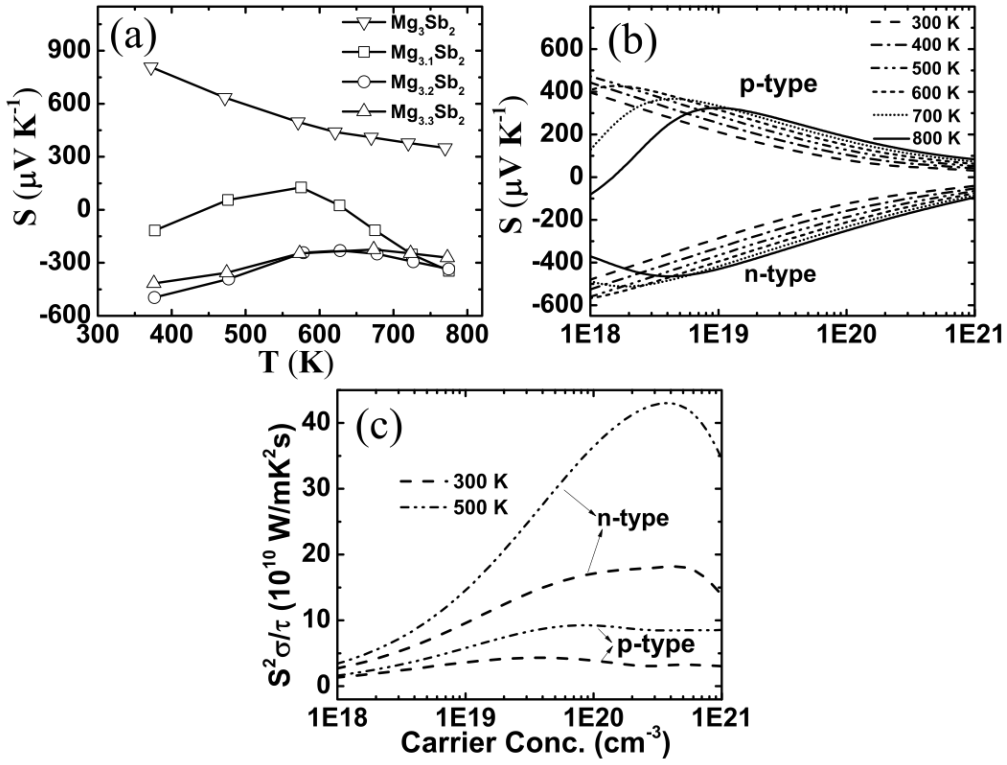

Figure 6.1 (a) Experimentally measured temperature-dependent Seebeck coefficient for $Mg_{3+x}Sb_2$ (x = 0, 0.1, 0.2, and 0.3). Calculated direction averaged thermoelectric properties for both p- (solid lines) and n-type (dashed lines) Mg_3Sb_2 with (b) showing the Seebeck coefficient with respect to carrier concentrations at different temperatures, and (c) the carrier concentrations dependent power factor (relaxation-time-related) at different temperatures.

Typically, good bulk thermoelectric materials have Seebeck coefficient in the range from 200 μV K^{-1} to 300 μV K^{-1} at the doping level and temperature where their performance is best. As shown in Fig. 1b for n-type case, one can reasonably anticipate that the optimized performance could be approached with appropriate doping levels in the 10^{19} to 10^{20} cm^{-3} range. Although the carrier concentration around 1.5×10^{19} cm^{-3} with good performance has been observed in the previous reported $Mg_{3.2}Sb_{1.5}Bi_{0.49}Te_{0.01}$, the electric transport properties near room temperature is still relatively low, which degrades the overall conversion efficiency. Therefore, further improvement could be expected for higher power factor if higher carrier concentration and electrical conductivity can be achieved. In this regard, we studied doping of Nb on the Mg site to optimize the electrical properties, stimulated by Nb's strong electron donation nature making half-Heusler compound NbCoSb into n-type [23].

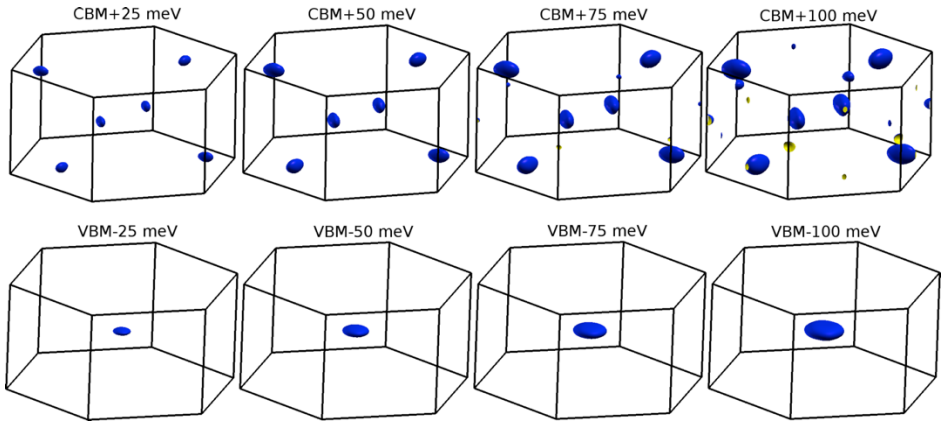

Figure 6.2 Calculated constant energy surfaces at 25, 50, 75, and 100 meV above conduction band minimum (CBM) and below valence band maximum (VBM), respectively.

6.4 Nb-Doped N-type Mg_3Sb_2-based Compounds

Following ball milling and hot pressing, the polycrystalline Nb-doped $Mg_{3.2-x}Nb_xSb_{1.5}Bi_{0.49}Te_{0.01}$ (x = 0, 0.05, 0.1, and 0.15) samples were fabricated and their XRD patterns are shown in Fig. 3. Major diffraction peaks are indexed with the reported structure of inverse a-La_2O_3 structure-type. However, the small amount of Nb_3Sb indicated by the arrow were detected in samples with x = 0.1 and 0.15. Although it seems the solubility limit of Nb is exceeded, this impurity also plays an important role by optimizing the properties (*e.g.*, decreasing the lattice thermal conductivity by phonon scattering).

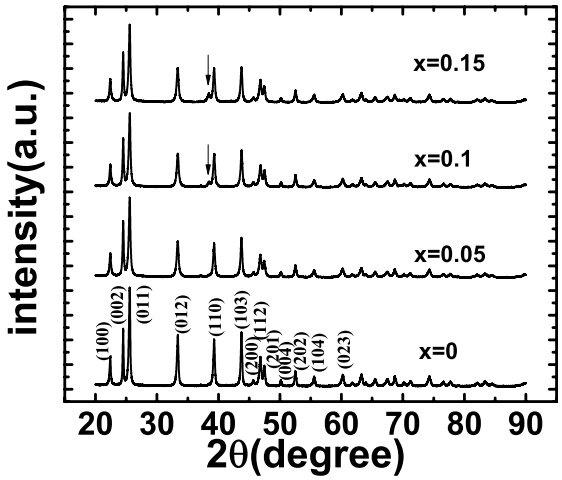

Figure 6.3 XRD patterns for $Mg_{3.2-x}Nb_xSb_{1.5}Bi_{0.49}Te_{0.01}$ (x = 0, 0.05, 0.1, and 0.15).

The microstructure of the optimized $Mg_{3.1}Nb_{0.1}Sb_{1.5}Bi_{0.49}Te_{0.01}$ sample is investigated by SEM and TEM. Both of them clearly indicate the sample is densely packed. The SEM image of Fig. 6.4a shows the grain size is between several hundred nm to a few

μm. Meanwhile, when observed in high-resolution transmission electron microscopy, it is evident that some nanoscale grains ranging from 5 to 10 nm can be found. The wide distribution of the grain size may be ascribed to the non-uniform grinding during ball-milling and short hot-pressing time for which the nanoparticles grow rapidly. Moreover, as also shown in Fig. 6.4b, clean grain boundaries can be easily observed, as well as semicoherent strain caused by misfit dislocation near the grain boundary. Those distortions in the lattices may be originated from mass and strain field fluctuations caused by the mass and size differences between host ion Mg^{2+} and doping ion Nb^{3+}. Besides, Fig. 6.4c shows one crystal grain with the inter plane spacing of 0.27 nm for planes (102), which proves again it belongs to the hexagonal crystal structure of space group $P\bar{3}m1$.

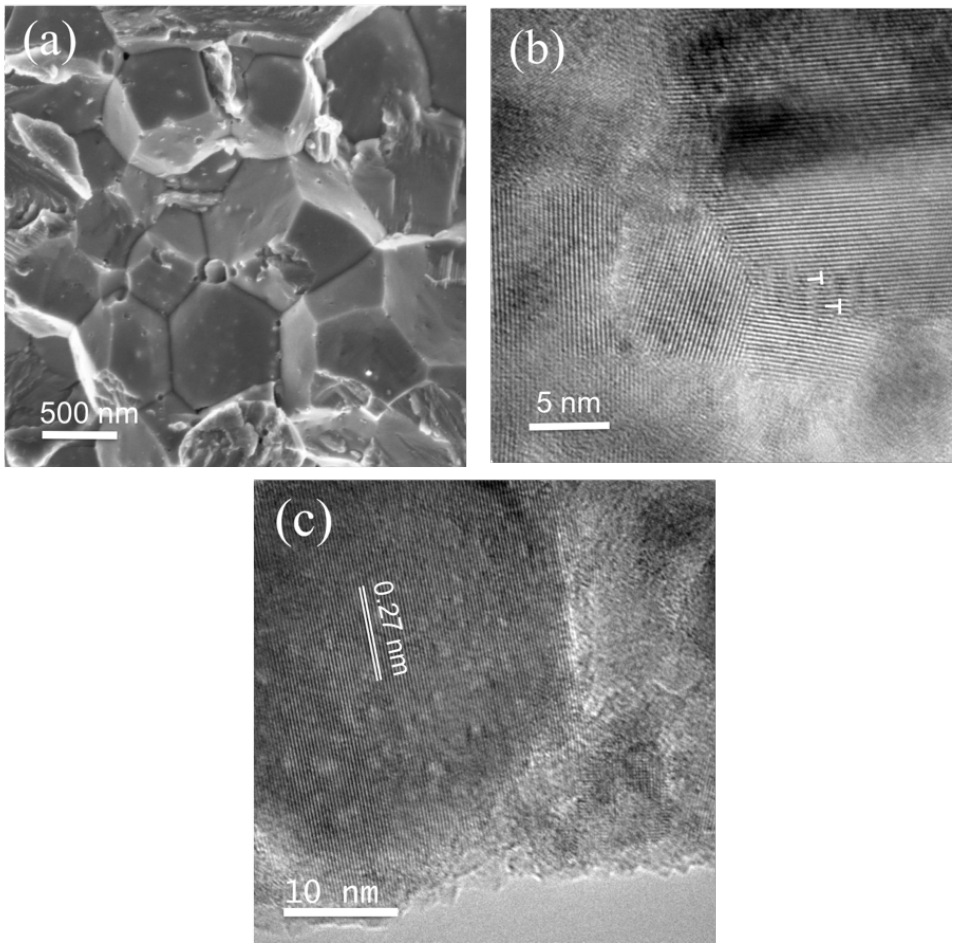

Figure 6.4 Typical microstructure for $Mg_{3.1}Nb_{0.1}Sb_{1.5}Bi_{0.49}Te_{0.01}$. (a) SEM image, (b) high magnification TEM showing the clear grain boundary and semicoherent strain by misfit dislocation around the grain boundary, and (c) high magnification showing one grain with inter planer spacing marked.

With each substitution of Nb^{3+} on a Mg^{2+} site we expect to introduce one additional free electron (e^-), due to the difference in valence states. This simple assumption works well for predicting carrier concentration of doped samples (*i.e.*, Nb doped $(Hf_{0.25}Zr_{0.75})_{1-x}Nb_xNiSn$ [24]), indicating that dopant primarily substitutes on the intended crystallographic sites [24]. However, in the current case, doping with Nb results in only a

fraction of the predicted electron concentration, mainly because the remainder forms secondary phases (Table 6.1). For example, when $x \geq 0.1$, the impurity Nb_3Sb was clearly identified in XRD pattern and the carrier concentration will no longer increase when $x \geq 0.1$. The Hall mobility decreases with Nb concentration, which may arise from increased secondary phases. When comparing with the p-type case, the Hall mobility for n-type samples is more than four times higher at the similar doping level (70 vs. 15 $cm^2\ V^{-1}\ s^{-1}$).

Table 6.1 Room-temperature thermoelectric transport properties of $Mg_{3.2-x}Nb_xSb_{1.5}Bi_{0.49}Te_{0.01}$ (x = 0, 0.05, 0.1, and 0.15).

$Mg_{3.2-x}Nb_xSb_{1.5}Bi_{0.49}Te_{0.01}$	$x = 0$	$x = 0.05$	$x = 0.1$	$x = 0.15$
Carrier concentration (10^{19} cm^{-3})	1.5	3.0	3.5	3.2
Hall mobility ($cm^2\ V^{-1}\ s^{-1}$)	70.2	69.8	69.2	60.5

Fig. 6.5a illustrates the electrical resistivity as a function of temperature up to 773 K. The resistivity of Nb-free sample is very high at room temperature. With temperature increase, the resistivity of samples of $x = 0$ first decreases and then increases. In contrast, Nb doped samples behave more like typical degenerate semiconductor: resistivity increases with temperature. Specifically, at room temperature, the resistivity of the sample with $x = 0.1$ is around 25 μΩ m, less than half of that in the sample with $x = 0$, and less than one-third of electrical resistivity in $x = 0$ sample (dotted curve) reported by Tamaki et al.

The Seebeck coefficients of the Nb-doped samples shown in Fig. 6.5b, are negative, consistent with the n-type carrier. The Seebeck coefficients increases with increasing Nb

concentration with the similar values in $x = 0.1$ and $x = 0.15$. The Seebeck coefficient of $x = 0$ sample in the reference is higher than that of our Nb-free sample, consistent with the higher electrical resistivity shown above. It is worth noting that further increasing Nb-doping concentration up to $x = 0.175$ results in positive Seebeck coefficient, probably due to the decreased extra Mg in the interstitial site or too much impurity Nb_3Sb phase. Detailed studies in this aspect is being carried out.

Calculated from the measured electrical resistivity and Seebeck coefficient, the power factors of all samples, are shown in Fig. 6.5c. By increasing Nb concentration, the power factor increases until $x = 0.1$ and then decreases. Near room temperature, the power factor for 0.1 Nb-doped sample is more than three times than that of Nb-free sample (14.7 vs. 4.5 $\mu W\ cm^{-1}\ K^{-2}$). Moreover, the peak power factor ~ 22 $\mu W\ cm^{-1}\ K^{-2}$ achieved in the optimized sample with $x = 0.1$ is much higher than the highest power factor (~8 $\mu W\ cm^{-1}\ K^{-2}$) reported in the corresponding p-type Mg_3Sb_2 [14]. When comparing with other closely related Zintl compounds (*e.g.*, 18 $\mu W\ cm^{-1}\ K^{-2}$ for $YbCd_{1.6}Zn_{0.4}Sb_2$, 16 $\mu W\ cm^{-1}\ K^{-2}$ for $Yb_{0.2}Eu_{0.2}Ca_{0.6}Mg_2Bi_2$), sample with $x = 0.1$ here also exhibits highly competitive power factor.

Thermal conductivity (κ), shown in Fig. 6.5d, is calculated as the product of density, specific heat (Cp) (Fig. S1a), and thermal diffusivity (D)($\kappa = D\rho_D C_P$). The electronic contribution (κ_e) to the total thermal conductivity was estimated using the Wiedemann Franz relationship ($\kappa_e = LT/\rho$), where the Lorenz number, L, was determined from experimental Seebeck coefficients using a single parabolic band model. Subtracting κ_e

from κ leaves the combined lattice κ_L and bipolar κ_{bipol} contribution shown in Fig. 6.5e. The samples with x = 0.1 and x = 0.15 here exhibit an obvious bipolar contribution, evidenced by the increase in $\kappa_L + \kappa_{bipol}$ at high temperature. At lower temperature, the total thermal conductivity decreases with increasing Nb concentration, primarily resulting from the suppressed lattice thermal conductivity. Such reduction can be ascribed to the mass and strain field fluctuation caused by the mass and size differences between the host ion Mg2+ and doping ion Nb3+ as the evidence shown in TEM images, as well as the enhanced interface scattering induced by increased impurities. However, Tamaki et al. reported much lower thermal conductivity and lattice thermal conductivity for the sample with x = 0. The big difference between the samples with x = 0 could come from the different fabrication methods, including ball-milling time and details, hot-press time and temperature, whether to add stearic acid or not and so on. In addition, different instruments (*e.g.,* LFA 447 in reference vs. LFA 457 here) could also cause different errors.

Through rationally selecting Nb dopant, simultaneous optimization of electrical power factor *PF* and significant reduction in thermal conductivity *κ* were achieved. The figure of merit of all samples is shown in Fig. 6.5f as a function of temperature. Nb-doped samples exhibit a higher figure of merit across the entire measured temperature, compared with the data reported by Tamaki *et al*. who reported extremely low thermal conductivity, especially at close to 300 K. The optimized composition is x = 0.1, which possesses the highest thermoelectric performance with $ZT \sim 0.4$ at 300 K and $ZT \sim 1.55$ at 773 K.

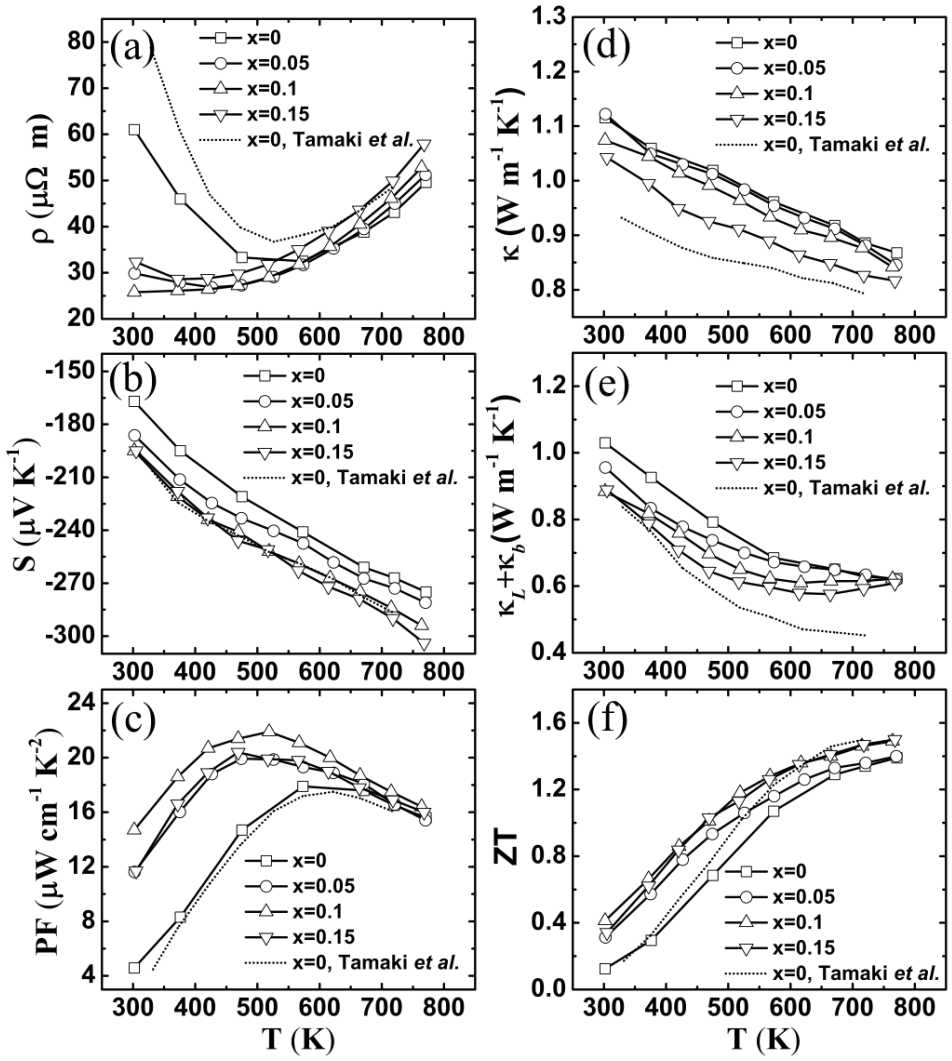

Figure 6.5 Temperature-dependent thermoelectric properties of $Mg_{3.2-x}Nb_xSb_{1.5}Bi_{0.49}Te_{0.01}$ (x = 0, 0.05, 0.1, and 0.15): (a) electrical resistivity, (b) Seebeck coefficient, (c) power factor, (a) total thermal conductivity, (b) lattice thermal conductivity, and (c) figure of merit *ZT*. The data reported by Tamaki *et al*. are included for comparison.

Although peak *ZT* and *PF* have often been used to evaluate thermoelectric materials, for thermoelectric devices that work at a large temperature difference, average *ZT* and *PF* over the whole temperature range are more important in determining the efficiency. As

reported, engineering figure of merit $(ZT)_{eng}$ and engineering power factor $(PF)_{eng}$ considering the Thomson effect are the best to accurately predict the conversion efficiency and output energy density for any giving hot side temperature T_h and cold side temperature T_c. $(PF)_{eng}$, $(ZT)_{eng}$, and efficiency are calculated, assuming T_c = 323 K, and T_h = 773 K and results are shown in Fig. 6.6. The data reported by Tamaki *et al*. are included in (a), (b) and (c) for comparison. It is clear that both $(PF)_{eng}$ and $(ZT)_{eng}$ increase around 40% at 773 K with Nb doping concentration x = 0.1. Specifically, the Nb-free sample exhibits a $(PF)_{eng}$, ~0.62 W m^{-1} K^{-1} and $(ZT)_{eng}$ ~0.64 but the 0.1 Nb-doped sample exhibits a $(PF)_{eng}$ ~0.80 W m^{-1} K^{-1} and $(ZT)_{eng}$ ~0.82 at 773 K. Fig. 6.6c shows that the sample with x = 0.1 improves the materials' performance by 28 % in terms of the calculated conversion efficiency over Nb-free case. Fig. 6.6d shows the maximum efficiency prediction of other advanced thermoelectric materials (*e.g.*, $Pb_{0.995}Cr_{0.005}Se$ (n-PbSe), $Ba_{0.3}In_{0.3}Co_4Sb_{12}$ (n-SKU), $(Hf_{0.25}Zr_{0.75})_{0.995}Nb_{0.005}NiSn$ (n-HH), $Bi_2Te_{2.7}Se$ (n-Bi_2Te_3)) based on the same evaluation methods (assuming T_c = 323 K and leg length 2 mm) [24-27]. It is clear that the optimized Nb-doped sample has the higher conversion efficiency among all the best materials. Specifically, at T_h = 773 K, the efficiency of the Nb-doped sample with x = 0.1 is above 14%, 25% higher than that of n-PbSe, 32% higher than that of n-SKU, and even 62% higher than that of n-HH. Therefore, it is reasonable to expect the future application of this promising n-type Nb-doped Zintl for pairing with the existing suitable p-type materials.

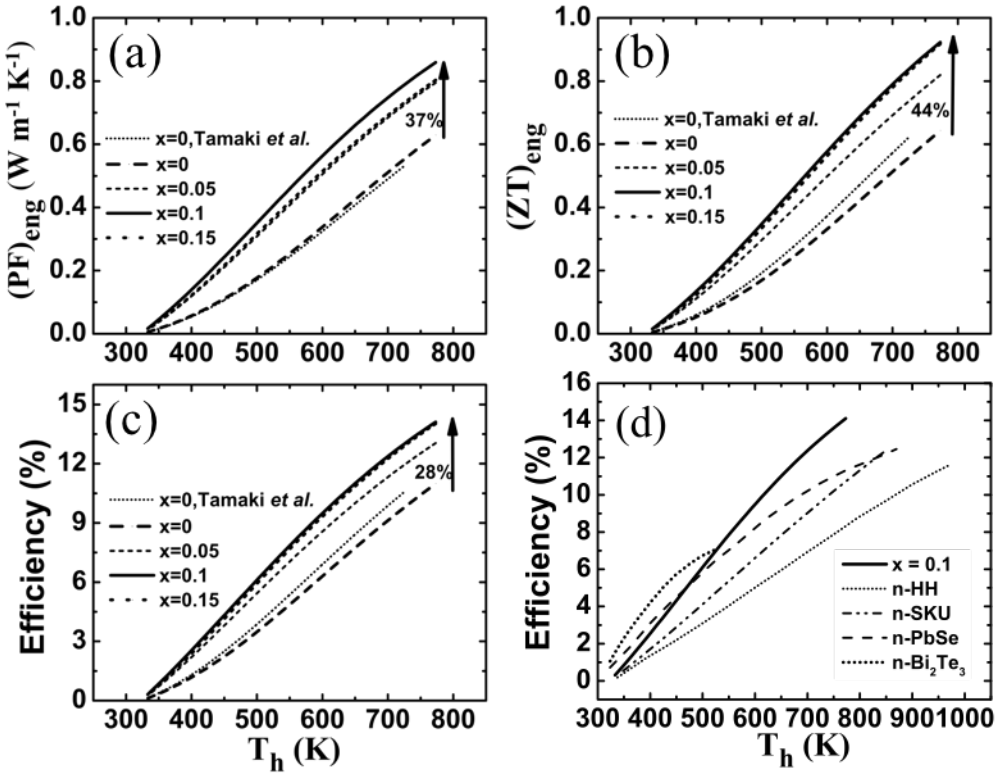

Figure 6.6 Calculated $(ZT)_{eng}$ (a) and $(PF)_{eng}$ (b) dependence of T_h up to 773 K with T_c at 323 K for $Mg_{3.2-x}Nb_xSb_{1.5}Bi_{0.49}Te_{0.01}$ (x = 0, 0.05, 0.1, and 0.15), efficiency (c) as a function of hot side temperature, and (d) comparison of calculated efficiency with other typical advanced n-type thermoelectric materials ($Pb_{0.995}Cr_{0.005}Se$: n-PbSe; $Ba_{0.3}In_{0.3}Co_4Sb_{12}$: n-SKU; $(Hf_{0.25}Zr_{0.75})_{0.995}Nb_{0.005}NiSn$: n-HH; $Bi_2Te_{2.7}Se_{0.3}$: n-Bi_2Te_3). The data reported by Tamaki *et al*. are included in (a), (b) and (c) for comparison.

It is worth pointing out that the power factor can be further improved by eliminating the impurity phase Nb_3Sb, and also choosing different doping elements and concentrations considering the still low electrical conductivity and high thermal conductivity. We adopted the reported Sb and Bi ratio, but this ratio may not be the optimal any more with Nb doping. It is possible some other elements in the Sb site may be more effective to reduce the thermal conductivity.

In summary, Nb-doped n-type $Mg_{3.2-x}Nb_xSb_{1.5}Bi_{0.49}Te_{0.01}$ Zintls is demonstrated to show much higher thermoelectric performance than any of the best n-type materials in the same temperature range. Through Nb doping, the simultaneous optimization of electrical power factor and the reduction in thermal conductivity were achieved, contributing to enhanced engineering $(PF)_{eng}$, and engineering $(ZT)_{eng}$. A conversion efficiency above 14 % is predicted with T_c = 323 K and T_h = 773 K, highest among all the advanced existing n-type materials in this temperature range.

6.5 Reference

[1] W. Liu, Q. Jie, H. S. Kim, Z. Ren, *Acta Materialia* **2015**, *87*, 357–376.

[2] F. Gascoin, S. Ottensmann, D. Stark, S. M. Haïle, G. J. Snyder, *Adv. Funct. Mater.* **2005**, *15*, 1860–1864.

[3] H. Zhang, J.-T. Zhao, Y. Grin, X.-J. Wang, M.-B. Tang, Z.-Y. Man, H.-H. Chen, X.-X. Yang, *J. Chem. Phys.* **2008**, *129*, 164713–6.

[4] X.-J. Wang, M.-B. Tang, H.-H. Chen, X.-X. Yang, J.-T. Zhao, U. Burkhardt, Y. Grin, *Appl. Phys. Lett.* **2009**, *94*, 092106–4.

[5] H. Zhang, L. Fang, M. B. Tang, Z. Y. Man, H. H. Chen, X. X. Yang, M. Baitinger, Y. Grin, J. T. Zhao, *J. Chem. Phys.* **2010**, *133*, 194701–6.

[6] E. S. Toberer, A. F. May, B. C. Melot, E. Flage-Larsen, G. J. Snyder, *Dalton Trans.* **2010**, *39*, 1046–1054.

[7] J. Shuai, Z. Liu, H. S. Kim, Y. Wang, J. Mao, R. He, J. Sui, Z. Ren, *J. Mater. Chem. A* **2016**, *4*, 4312–4320.

[8] J. Shuai, Y. Wang, Z. Liu, H. S. Kim, J. Mao, J. Sui, Z. Ren, *Nano Energy* **2016**, *25*, 136–144.

[9] J. Shuai, H. S. Kim, Z. Liu, R. He, J. Sui, Z. Ren, *Appl. Phys. Lett.* **2016**, *108*,

183901–5.

[10] G. S. Pomrehn, A. Zevalkink, W. G. Zeier, A. van de Walle, G. J. Snyder, *Angew. Chem.* **2014**, *53*, 3422–3426.

[11] A. Zevalkink, W. G. Zeier, E. Cheng, J. Snyder, J.-P. Fleurial, S. Bux, *Chem. Mater.* **2014**, *26*, 5710–5717.

[12] S. Kim, C. Kim, Y.-K. Hong, T. Onimaru, K. Suekuni, T. Takabatake, M.-H. Jung, *J. Mater. Chem. A* **2014**, *2*, 12311–6.

[13] C. L. Condron, S. M. Kauzlarich, F. Gascoin, G. J. Snyder, *Journal of Solid State Chemistry* **2006**, *179*, 2252–2257.

[14] J. Shuai, Y. Wang, H. S. Kim, Z. Liu, J. Sun, S. Chen, J. Sui, Z. Ren, *Acta Materialia* **2015**, *93*, 187–193.

[15] H. Tamaki, H. K. Sato, T. Kanno, *Adv. Mater.* **2016**, 1–6.

[16] D. J. Singh, L. Nordstrom, *Planewaves, Pseudopotentials, and the LAPW Method*, Springer, Berlin, **2006**.

[17] K. Schwarz, P. Blaha, G. K. H. Madsen, *Computer Physics Communications* **2002**, *147*, 71–76.

[18] A. K. Ganguli, Y. U. Kwon, J. D. Corbett, *Inorg. Chem.* **1993**, *32*, 4354–4359.

[19] J. P. Perdew, K. Burke, M. Ernzerhof, *Phys. Rev. Lett.* **1996**, *77*, 3865–3868.

[20] F. Tran, P. Blaha, *Phys. Rev. Lett.* **2009**, *102*, 226401–4.

[21] G. K. H. Madsen, D. J. Singh, *Computer Physics Communications* **2006**, *175*, 67–71.

[22] A. Bhardwaj, D. K. Misra, *RSC Advances* **2014**, *4*, 34552–34560.

[23] L. Huang, R. He, S. Chen, H. Zhang, K. Dahal, H. Zhou, H. Wang, Q. Zhang, Z. Ren, *Materials Research Bulletin* **2015**, *70*, 773–778.

[24] H. Zhang, Y. Wang, K. Dahal, J. Mao, L. Huang, Q. Zhang, Z. Ren, *Acta Materialia* **2016**, *113*, 41–47.

[25] Q. Zhang, E. K. Chere, K. McEnaney, M. Yao, F. Cao, Y. Ni, S. Chen, C. Opeil, G. Chen, Z. Ren, *Adv. Energy Mater.* **2015**, *5*, 1401977–8.

[26] W. Zhao, P. Wei, Q. Zhang, C. Dong, L. Liu, X. Tang, *J. Am. Chem. Soc.* **2009**, *131*, 3713–3720.

[27] X. Yan, B. Poudel, Y. Ma, W. S. Liu, G. Joshi, H. Wang, Y. Lan, D. Wang, G. Chen, Z. F. Ren, *Nano Lett.* **2010**, *10*, 3373–3378.

Chapter 7

MgAgSb with Na Doping

Reproduced with permission from *Nano Energy*, 11, 640-646 (2015).

7.1 Introduction

In the previous chapters, we mainly focus on the Zintl Phases, which are normally suitable for application in the intermediate temperature range (300-600 °C). For power-generation applications with hot side below 473 K, BiSbTe alloys have been the only p-type thermoelectric material for over half a century [1-3] with *ZT* around 1 at room temperature for commercial ingot. Nevertheless, due to the fact that Tellurium (Te) is a rare element, Earth abundance around 0.001 ppm, only about one-quarter of gold (Au) ~0.004 ppm [4], new promising alternatives without Te should be studied and optimized for potential large-scale applications.

Recently, p-type MgAgSb and its modified composition $MgAg_{0.97}Sb_{0.99}$ were reported by our group and found to exhibit a *ZT* as high as ~1.2 at 200 °C [5]. A small amount of Ni has been used to alloy the Ag site and has resulted in enhancement of *ZT* to ~1 at 50 °C and ~1.4 at 180 °C. However, the electrical resistivities of $MgAg_{0.97}Sb_{0.99}$ and Ni doped samples are relatively high, originated from the relative low carrier concentration.

If it is to be paired with the existed n-type advanced thermoelectric materials, such as Bi_2Te_3 [6], decreasing the resistivity would be the next challenge.

As we talked in Chapter 5, Na has been proved to be an ideal hole dopant for increasing thermoelectric performance in Zintl phases $Ca_{1-x}Na_xMg_2Bi_{1.98}$ and $Mg_{3-x}Na_xSb_2$ [7,8]. In this Chapter, we report our effort, once again, for Na doping on Mg site of $MgAg_{0.97}Sb_{0.99}$. Upon Na doping, carrier concentration has increased, contributing to reduced resistivity and higher power factor. Moreover, higher *ZT* value, better self-compatibility factors and output power have been achieved.

7.2 Synthesis Process and Thermoelectric Properties

Synthesis process. Based on the undoped phase-pure composition $MgAg_{0.97}Sb_{0.99}$, we studied substitution of Mg by Na by the two-step process. First, elemental magnesium metal pieces (Mg, Sigma Aldrich, 99.9% metal basis), silver metal pieces (Ag, Sigma Aldrich, 99.9% metal basis), and sodium (Na, Sigma Aldrich, 99.9% metal basis) were weighed according to the stoichiometry of $Mg_{1-x}Na_xAg_{0.97}Sb_{0.99}$ with x = 0, 0.005, 0.0075, and 0.01 and loaded in a stainless steel jar with stainless steel balls for mechanical alloying by a high energy ball mill (SPEX 8000D) for 10 h. After this step, we added antimony chunks (Sb, Sigma Aldrich, 99.8% metal basis) into the jar to further milling for 8 h. The final nanopowders were then loaded into a graphite die with an inner diameter of 12.7 mm, and consolidated by direct current (DC) hot pressing at ~300 °C for 5 min.

Results and Discussion. Fig. 7.1 shows the XRD patterns of all samples. By comparing with the undoped pure phase $MgAg_{0.97}Sb_{0.99}$, no detectable impurity phases were found in $Mg_{1-x}Na_xAg_{0.97}Sb_{0.99}$ (x = 0.005, 0.0075, and 0.01).

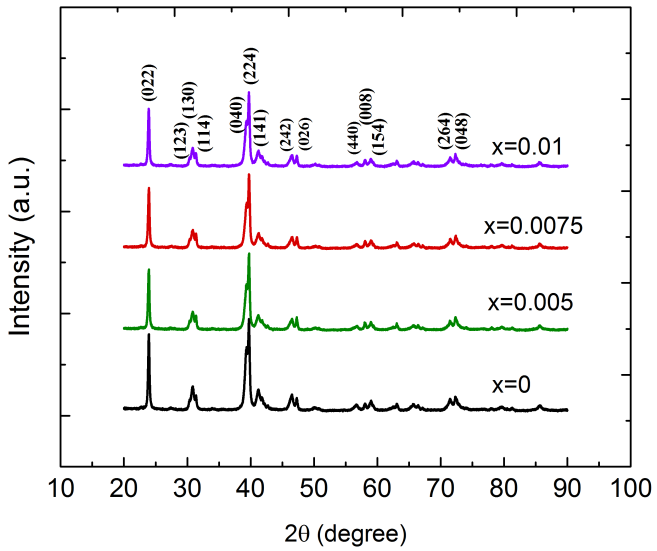

Figure 7.1 XRD patterns of $Mg_{1-x}Na_xAg_{0.97}Sb_{0.99}$ (x = 0, 0.005, 0.0075, and 0.01).

To study the influence of Na doping on the thermoelectric properties of the materials, samples with compositions $Mg_{1-x}Na_xAg_{0.97}Sb_{0.99}$ (x = 0, 0.005, 0.0075, and 0.01) were prepared. As shown in Fig. 7.2a, the electrical resistivity decreases with increasing Na content till x = 0.0075, and the electrical resistivity of all the samples increases with temperature first to the maximum around 75-100 °C and then decrease. When the temperature is above 100 °C, the electrical resistivity decreases, which is consistent with the turning point in the Seebeck coefficient due to bipolar effect in Fig. 7.2b. Higher Na content leads to lower electrical resistivity due to the enhanced carrier concentration shown in Table 7.1. We compared the undoped sample with Na-doped samples of x = 0.005, 0.0075, and 0.01, and found carrier concentration increases by 32.5%, 44.6% and 43.2%,

respectively. The carrier concentration (n_H) and Hall mobility (u_H), which is also shown in Table 7.1, affect the electrical resistivity (ρ) by the relationship $1/\rho = n_H e u_H$. Fig. 7.2b shows the temperature-dependent Seebeck coefficient of all the Na doped samples. The Seebeck coefficient decreases with increasing Na content till $x = 0.0075$, and increases with temperature from room temperature to 75-100 °C before decreases up to 275 °C. Combing the electrical resistivity and Seebeck coefficient, the power factors of all Na doped samples are obtained as shown in Fig. 7.2c. The increase in power factor with temperature, especially below 100 °C, is pronounced as Na content increases. The highest power factor among all the samples was found for $x = 0.0075$. Na doping effectively optimizes carrier concentration and mobility, leading to lower electrical resistivity, yielding improvement of power factor over the whole temperature range.

Table 7.1 Carrier concentration and Hall mobility at room temperature of $Mg_{1-x}Na_xAg_{0.97}Sb_{0.99}$ (x = 0, 0.005, 0.0075, and 0.01).

$Mg_{1-x}Na_xAg_{0.97}Sb_{0.99}$	x=0	x=0.005	x=0.0075	x=0.01
Carrier concentration (10^{19} cm^{-3})	2.413	3.198	3.49	3.455
Hall mobility (cm^2 V^{-1} s^{-1})	70.2	70.3	74.9	70.1

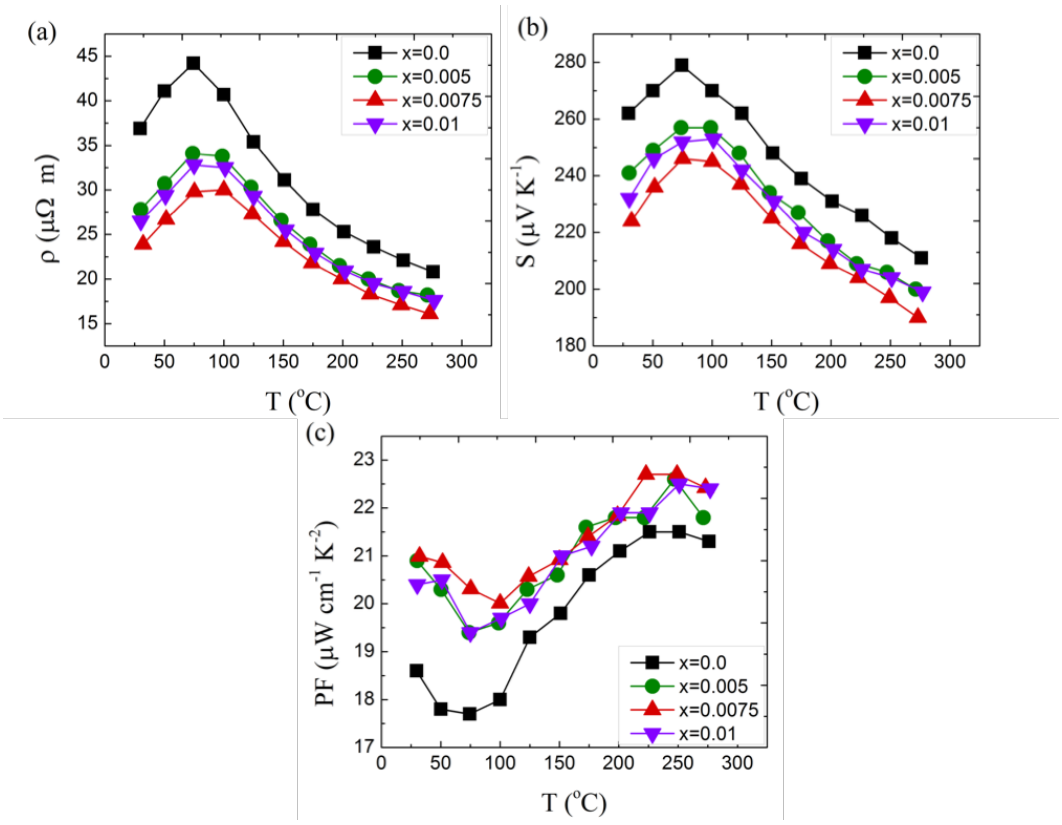

Figure 7.2 Temperature-dependent thermoelectric properties of $Mg_{1-x}Na_xAg_{0.97}Sb_{0.99}$ (x = 0, 0.005, 0.0075, and 0.01): (a) Electrical resistivity; (b) Seebeck coefficient; and (c) power factor.

Fig. 7.3 shows the thermal transport properties of $Mg_{1-x}Na_xAg_{0.97}Sb_{0.99}$ with x = 0, 0.005, 0.0075, and 0.01. Specific heat (C_p) of $MgAg_{0.97}Sb_{0.99}$, shown in Fig. 7.3a, is used for all compositions since replacing a tiny amount of Mg by Na will not increase the C_p at all due to the fact that Na is next to Mg, and diffusivity (D) of all samples $Mg_{1-x}Na_xAg_{0.97}Sb_{0.99}$ is shown in Fig. 7.3b. C_p and D are used to calculate the total thermal conductivity (κ) of a series of doped samples using $\kappa = D\rho C_p$, where ρ is the measured density of the samples. The densities of all the samples $Mg_{1-x}Na_xAg_{0.97}Sb_{0.99}$ with x = 0, 0.005, 0.0075, and 0.01 measured by Archimedes method are 6.17, 6.168, 6.165, 6.185

cm^{-3}, respectively, ~98% of the theoretical density 6.31 g cm^{-3}. The C_p dependence of temperature shows that there are two phase transitions with increasing temperature, from α phase to β phase at ~333 °C and from β phase to γ phase at ~360 °C. The temperature dependence of the total thermal conductivity (κ) of Na doped samples, along with the lattice contributions (κ_L), are plotted in Fig. 7.3c and d, respectively. The thermal conductivity decreases with temperature first, reaching a minimum κ at around 75-100 °C, and then increases from 100 °C to 275 °C due to the bipolar effect, which is consistent with electrical resistivity curves. As Na content increases, the thermal conductivity κ increases and lattice thermal conductivity (κ_L) decreases. The lattice thermal conductivity κ_L was determined by subtracting the electronic contribution κ_e, $\kappa_L = \kappa - \kappa_e$, κ_e is calculated using the Wiedemann-Franz relation $\kappa_e = L\sigma T$, where L is the Lorenz number, which can be obtained from fitting the respective Seebeck coefficient values with an estimate of the reduced chemical potential.

For the undoped sample $MgAg_{0.97}Sb_{0.99,}$ the low thermal conductivity over the whole temperature range from 25 to 275 °C, shown in Fig. 7.3c, can be ascribed to the distorted structure, large unit cell and the strong phonon scattering due to the deficiencies at both the Ag and Sb sites, and small grain size. The Na-doped samples with fairly good uniform grains in the range of 50-200 nm are very similar to the undoped $MgAg_{0.97}Sb_{0.99}$ sample.

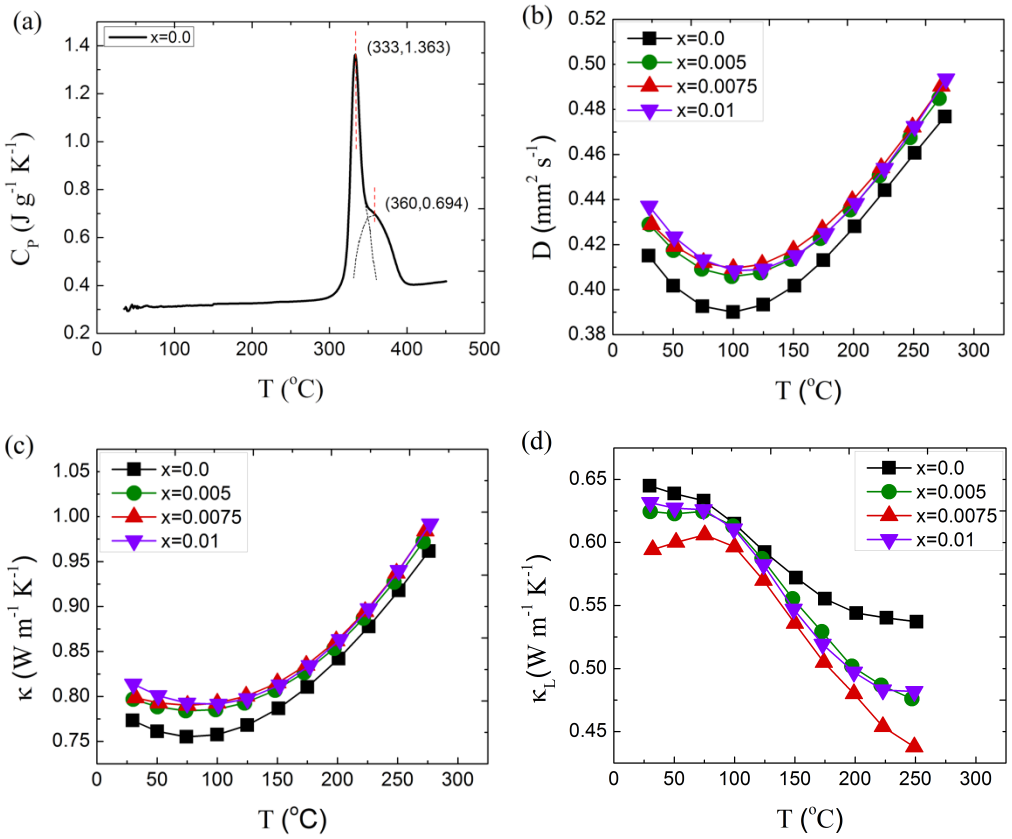

Figure 7.3 Temperature-dependent thermal transport properties of $Mg_{1-x}Na_xAg_{0.97}Sb_{0.99}$ (x = 0, 0.005, 0.0075, and 0.01): (a) Specific heat; (b) thermal diffusivity; (c) total thermal conductivity; and (d) lattice thermal conductivity.

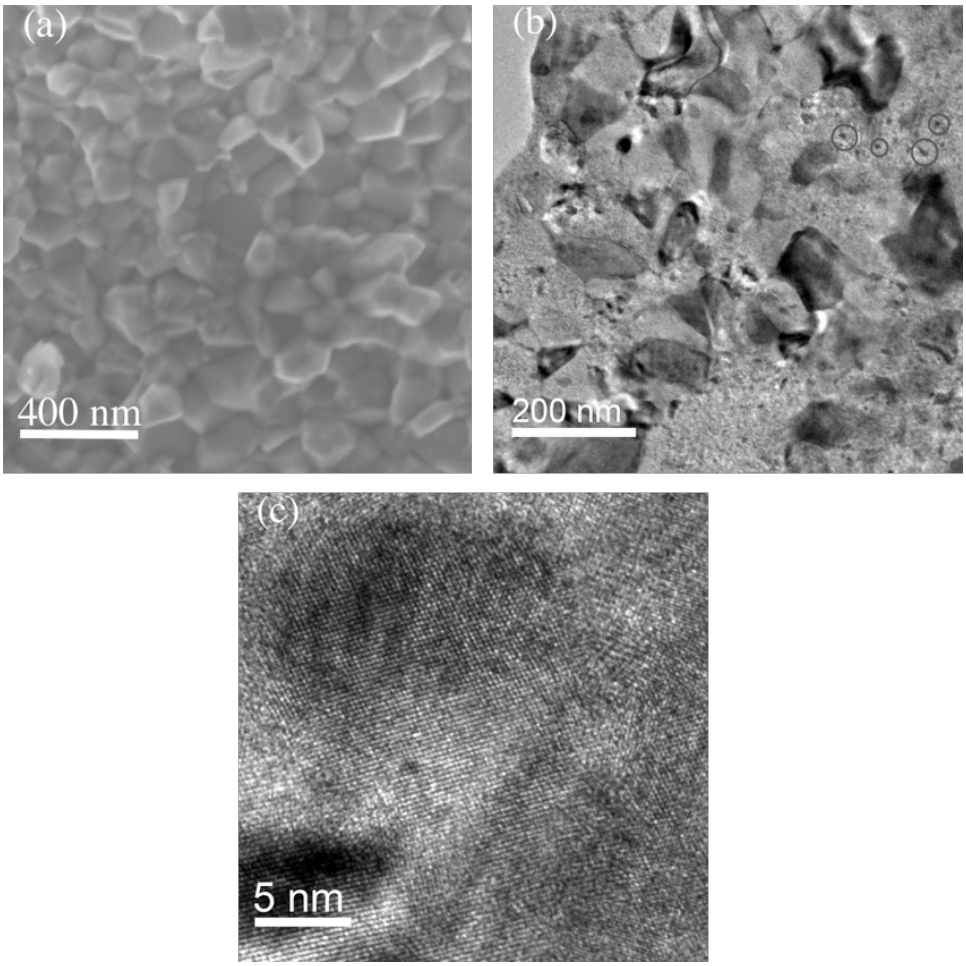

Figure 7.4 SEM and TEM images of sample $Mg_{0.9925}Na_{0.0075}Ag_{0.97}Sb_{0.99}$: (a) SEM image; (b) medium magnification TEM image with selected area electron diffraction pattern as the inset; and (c) high resolution TEM image.

SEM investigation was carried out on the freshly fractured surface of the bulk samples $Mg_{0.9925}Na_{0.0075}Ag_{0.97}Sb_{0.99}$ to examine the homogeneities of the grains and is shown in Fig. 7.4a. In order to further understand the grain structure, TEM images were taken and are shown in Fig. 7.4b and c. For sample $Mg_{0.9925}Na_{0.0075}Ag_{0.97}Sb_{0.99}$, the medium magnification TEM image shows the grains are in the range of 10-20 nm and confirmed by the SAED patterns, shown in the inset of Fig. 7.4b. The relatively small grains of 10-20 nm are further confirmed by the high-resolution TEM image, shown in Fig. 7.4c, indicating

the grains observed in SEM images are composed of much smaller grains, which yields the low thermal conductivity. For samples $Mg_{0.9925}Na_{0.0075}Ag_{0.97}Sb_{0.99}$, the low magnification TEM image, Fig. 7.4b, shows the same results as SEM images, confirming the grains are in the range of 50-200nm. The black dots, which are circled in Fig. 7.4b, might be the nano precipitates. High-resolution TEM image, shown in Fig. 7.4c, indicates the grains are crystallized.

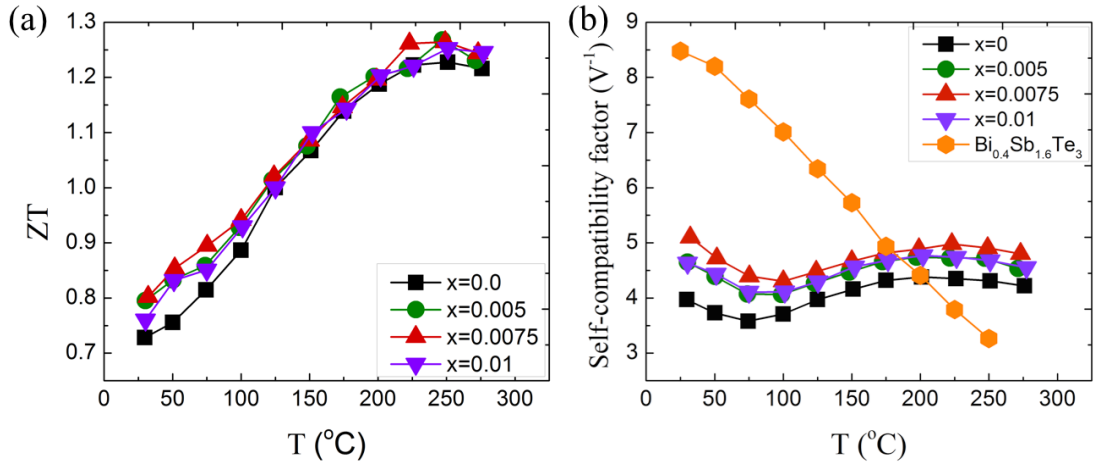

Figure 7.5 (a)Temperature-dependent *ZT* for $Mg_{1-x}Na_xAg_{0.97}Sb_{0.99}$ (x = 0, 0.005, 0.0075, and 0.01). (b)Thermoelectric self-compatibility factors of $Mg_{1-x}Na_xAg_{0.97}Sb_{0.99}$ (x = 0, 0.005, 0.0075, and 0.01), the self-compatibility factor of $Bi_{0.4}Sb_{1.6}Te_3$ is also plotted for comparison.

The temperature-dependent *ZT* for $Mg_{1-x}Na_xAg_{0.97}Sb_{0.99}$ (x = 0, 0.005, 0.0075, and 0.01) is presented in Fig. 7.5a. With increasing temperature, the *ZT* value increases, reaching a peak *ZT* ~1.26 at about 250 °C for $Mg_{0.9925}Na_{0.0075}Ag_{0.97}Sb_{0.99}$. Na-doped samples show generally a little better performance. At 30 °C, we achieved *ZT* of ~0.8 in samples $Mg_{1-x}Na_xAg_{0.97}Sb_{0.99}$ with x = 0.005 and 0.0075.

Compatibility factor $c = (\sqrt{1+ZT}-1)/ST$, calculated from the temperature-dependent Seebeck Coefficient and *ZT*, is regarded as a thermoelectric property essential for designing an efficient segmented thermoelectric device [9]. For a single material, it is called self-compatibility factor [10]. The physics of compatibility is about the matching of the physical properties over the whole length of the thermoelectric leg. The change in compatibility factor will have an effect on device performance since it is temperature dependent. A large difference of each individual property for the cold and hot side will cause incompatibility. Fig. 7.5b shows the self-compatibility factors of all samples $Mg_{1-x}Na_xAg_{0.97}Sb_{0.99}$ (x = 0, 0.005, 0.0075, and 0.01). The self-compatibility factors of most Na doped samples vary less than 15%. Compared to other materials, such as $Bi_{0.4}Sb_{1.6}Te_3$, the self-compatibility of MgAgSb-based materials shows much less temperature dependent, which will contribute to a relatively higher efficiency.

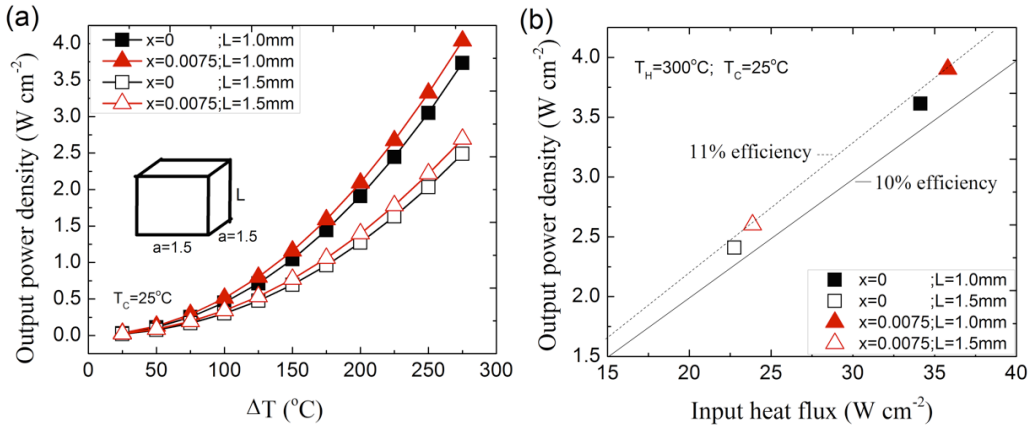

Figure 7.6 Output power of different dimensions. (a) Output power generation at the maximum power generation mode of $R_L/R_{leg} \sim 1$ (R_L: load resistance and R_{leg}: leg resistance) according to the temperature difference and leg length at the fixed cross section area, a = 1.5 mm, and (b) output power density according to its input heat flux at the maximum efficiency mode of $R_L/R_{leg} \sim 1.4$ at $\Delta T = 275$ °C.

To predict the thermoelectric performance under a certain temperature difference, a numerically iterative calculation was carried out based on a finite difference model [11] [12]in which the temperature dependence of thermoelectric properties was taken into account. The governing equation of 1-D energy balance in a differential element of thermoelectric leg is,

$$\frac{d}{dx}\left(\kappa(T(x))\frac{dT(x)}{dx}\right)+J^2\rho(T(x))-JT(x)\frac{dS(T(x))}{dx}=0 \qquad (7.1)$$

where, $T(x)$ is temperature distribution through a thermoelectric leg as a function of position x (x = 0 for T_H), and J is electric current density, $\kappa(T(x))$, $\rho(T(x))$ and $S(T(x))$ are temperature-dependent thermal conductivity, electric resistivity, and Seebeck coefficient, repectively. The left-hand-side three terms represent conduction heat, Joule heat, and Thomson heat, respectively. By applying Eq. 7.1 into each differential element, numerically converged temperature profile and current density followed by output power and conversion efficiency can be obtained. In this model, an adiabatic condition is assumed and only thermoelectric leg is considered by ignoring electrical contact resistances. Two sets of the leg dimensions are examined: 1.0 mm and 1.5 mm of leg lengths with a fixed cross section of 1.5 mm x 1.5 mm. Fig. 7.6a shows the generated output power density, W cm^{-2}, at various temperature differences. As compared with the undoped $MgAg_{0.97}Sb_{0.99}$, the output power of Na-doped $Mg_{0.9925}Na_{0.0075}Ag_{0.97}Sb_{0.99}$ increases by 8.1% at ΔT = 275 °C in both L = 1.0 and 1.5 mm mainly due to the enhancement of the power factor by lowering electric resistivity while the conversion efficiency is only improved by 3.0%. The reason why the improvement of the leg efficiency is smaller than that of the output power

because the improved output power is offset by the larger required input heat flux as shown in Fig. 7.6b to maintain the constant temperature difference, which is caused by the increased thermal conductivity. The leg with L = 1.0 mm gives a larger power output by 50% at ΔT = 275 °C as compared to the leg with L = 1.5 mm since the shorter leg reduces the electrical resistance resulting in more electric current flow under the constant load voltage based on the fixed ΔTs. Thus, a shorter thermoelectric leg is desired to boost up the output power generation once the boundary temperature T_H and T_C are constantly maintained, which can improve volumetric power density (W m^{-3}), mass power density (W kg^{-1}), and cost-effectiveness (W $\$^{-1}$) as well. However, one also needs to consider that a shorter leg requires more heat flux to generate the same temperature gradient through the reduced length, where the conversion efficiency in this ideal model has no benefit as shown in Fig. 7.6b. In addition, electric contact resistance, thermal resistance of electrodes and insulation materials, and thermal shear stress at bonding interfaces of dissimilar materials are also taken into account to figure out proper geometry of a leg.

In conclusion, Na alloying to Mg of the samples $Mg_{1-x}Na_xAg_{0.97}Sb_{0.99}$ (x = 0.005, 0.0075, 0.01) enhances the power factor by increasing carrier concentration. Higher power factor results in higher output power but not too much higher ZTs due to higher thermal conductivity caused by the higher electrical conductivity. Further optimization of alloying in each site and carrier concentration could lead to even higher power factor, higher ZT, and ultimately higher output power.

7.3 Reference

[1] H. J. Goldsmid, R. W. Douglas, *British Journal of Applied Physics* **1954**, *5*, 386.

[2] G. E. Smith, *Appl. Phys* **1962**, *33*, 841.

[3] G. Zheng, X. Su, X. Li, T. Liang, H. Xie, X. She, Y. Yan, C. Uher, M. G. Kanatzidis, X. Tang, *Adv. Energy Mater.* **2016**, DOI: 10.1002/aenm.201600595.

[4] B. Poudel, Q. Hao, Y. Ma, Y. Lan, A. Minnich, B. Yu, X. Yan, D. Wang, A. Muto, D. Vashaee, et al., *Science* **2008**, *320*, 634–638.

[5] H. Zhao, J. Sui, Z. Tang, Y. Lan, Q. Jie, D. Kraemer, K. McEnaney, A. Guloy, G. Chen, Z. Ren, *Nano Energy* **2014**, *7*, 97–103.

[6] X. Yan, B. Poudel, Y. Ma, W. S. Liu, G. Joshi, H. Wang, Y. Lan, D. Wang, G. Chen, Z. F. Ren, *Nano Lett.* **2010**, *10*, 3373–3378.

[7] J. Shuai, Y. Wang, H. S. Kim, Z. Liu, J. Sun, S. Chen, J. Sui, Z. Ren, *Acta Materialia* **2015**, *93*, 187–193.

[8] J. Shuai, H. S. Kim, Z. Liu, R. He, J. Sui, Z. Ren, *Appl. Phys. Lett.* **2016**, *108*, 183901–5.

[9] G. J. Snyder, T. S. Ursell, *Phys. Rev. Lett.* **2003**, *91*, 148301–4.

[10] W. Seifert, G. J. Snyder, E. S. Toberer, C. Goupil, K. Zabrocki, E. Müller, *Phys. Status Solidi A* **2013**, *210*, 1407–1417.

[11] G. D. Mahan, *J. Appl. Phys.* **1991**, *70*, 4551–4554.

[12] T. P. Hogan, T. Shih, *Thermoelectrics Handbook: Macro to Nano* **2006**.

Appendix

List of Publications

[1] **Jing Shuai**, Shaowei Song, Jifeng Sun, Yumei Wang, Ran He, Jiawei Zhou, David J. Singh, Gang Chen, and Zhifeng Ren, "Enhancing thermoelectric properties of n-type Mg_3Sb_2-based Zintl phase through partial substitution of Mg by Nb", Submitted, 2016.

[2] **Jing Shuai**, Huiyuan Geng, Yucheng Lan, Zhuan Zhu, Chao Wang, Zihang Liu, Jiming Bao, Ching-Wu Chu, Jiehe Sui, and Zhifeng Ren, "Higher thermoelectric performance of Zintl phases $(Eu_{0.5}Yb_{0.5})_{1-x}Ca_xMg_2Bi_2$ by band engineering and strain fluctuation", ***Proceedings of the National Academy of Science***, 113, E4125, 2016.

[3] **Jing Shuai**, Hyun Deog Yoo, Yanliang Liang, Yifei Li, Yan Yao, Lars Grabow, "Density functional theory study of Li, Na, and Mg intercalation and diffusion in MoS_2 with controlled interlayer spacing", ***Materials Research Express*** *3*, 064001, 2016.

[4] **Jing Shuai**, Zihang Liu, Hee Seok Kim, Yumei Wang, Jun Mao, Ran He, Jiehe Sui and Zhifeng Ren, "Thermoelectric properties of Bi-based Zintl compounds $Ca_{1-x}Yb_xMg_2Bi_2$" ***Journal of Materials Chemistry A*** *4*, 4312-4320, 2016.

[5] **Jing Shuai**, Yumei Wang, Zihang Liu, Hee Seok Kim, Jun Mao, Jiehe Sui, and Zhifeng Ren, "Enhancement of thermoelectric performance of phase pure Zintl compounds $Ca_{1-x}Yb_xZn_2Sb_2$, $Ca_{1-x}Eu_xZn_2Sb_2$, and $Eu_{1-x}Yb_xZn_2Sb_2$ by mechanical alloying and hot pressing", ***Nano Energy*** *25*, 136-144, 2016.

[6] **Jing Shuai,** Hee Seok Kim, Zihang Liu, Ran He, Jiehe Sui, and Zhifeng Ren, "Thermoelectric Properties of Zintl Compound $Ca_{1-x}Na_xMg_2Bi_{1.98}$", ***Applied***

Physics Letters *108*, 183901, 2016.

[7] **Jing Shuai**, Hee Seok Kim, Yucheng Lan, Yuan Liu, Huaizhou Zhao, Jiehe Sui, and Zhifeng Ren, "Study on thermoelectric performance by Na doping in nanostructured $Mg_{1-x}Na_xAg_{0.97}Sb_{0.99}$", ***Nano Energy*** *11*, 640-646, 2015.

[8] **Jing Shuai**, Yumei Wang, Hee Seok Kim, Zihang Liu, Jingying Sun, Shuo Chen, Jiehe Sui, and Zhifeng Ren, "Thermoelectric properties of Na-doped Zintl compound: $Mg_{3-x}Na_xSb_2$". ***Acta Materialia*** *93*, 187-193, 2015.

[9] Yanliang Liang, Hyun Deog Yoo, Yifei Li, **Jing Shuai**, Hector A. Calderon, Francisco Carlos Robles Hernandez, Lars C. Grabow, and Yan Yao, "Interlayer-Expanded Molybdenum Disulfide Nanocomposites for Electrochemical Magnesium Storage", ***Nano Letters*** *15*, 2194-2202, 2015.

[10] Dandan Li, Shanming Li, Beipei Wei, **Jing Shuai**, Chenglong Shi, Xuekui Xi, Peijie Sun, Sheng Meng, Lin Gu, Zhifeng Ren, Xiaolong Chen and Huaizhou Zhao, "Atomic disorders induced by Silver and Magnesium Ion Migrations Favor High Thermoelectric Performance in MgAgSb-Based Materials", ***Advanced Functional Materials*** *25*, 6478-6488. 2015.

[11] Zihang Liu, Yumei Wang, Jun Mao, Huiyuan Geng, **Jing Shuai**, Yuanxu Wang, Ran He, Wei Cai, Jiehe Sui, Zhifeng Ren, "Lithium Doping to Enhance Thermoelectric Performance of MgAgSb with Weak Electron-Phonon Coupling", ***Advanced Energy Materials***, DOL:10.1002/aenm.201502269, 2016.

[12] Zihang Liu, **Jing Shuai**, Jun Mao, Yumei Wang, Zhengyun Wang, Jiehe Sui, and Zhifeng Ren, "Effects of antimony content in $MgAg_{0.97}Sb_x$ on output power and energy conversion efficiency", ***Acta Materialia*** *102*, 17-23, 2016.

[13] Jijun Gong, Anjun Hong, **Jing Shuai**, Lin Li, Zhibo Yan, Zhifeng Ren, Junming Liu, "Investigation of the bipolar effect in the thermoelectric material CaMg2Bi2 using a first-principles study", ***Physical Chemistry Chemical Physics***, DOI:

10.1039/c6cp02057g, 2016.

[14] Zihang Liu, **Jing Shuai**, Huiyuan Geng, Jun Mao, Yan Feng, Xu Zhao, Xianfu Meng, Ran He, Wei Cai, and Jiehe Sui, "Contrasting the role of Mg and Ba doping on the microstructure and thermoelectric properties of p-type $AgSbSe_2$", ***ACS Apply Materials & Interfaces*** 7, 23047-23055, 2015.

[15] Jiehe Sui, **Jing Shuai**, Yucheng Lan, Yuan Liu, Ran He, Qing Jie, and Zhifeng Ren, "Effect of Cu concentration on thermoelectric properties of nanostructured p-type $MgAg_{0.97-x}Cu_xSb_{0.99}$", ***Acta Materialia*** *87*, 266-272, 2015.

[16] Jun Mao, Hee Seok Kim, **Jing Shuai**, Zihang Liu, Ran He, Udara Saparamadu, Fei Tian, Weishu Liu, and Zhifeng Ren, "Thermoelectric property studies on $Mg_2(Sn_{0.765}Ge_{0.22}Sb_{0.015})_{1-x}(Sn_{0.685}Si_{0.3}Sb_{0.015})_x$ materials in Mg_2Sn-Mg_2Ge-Mg_2Si system", ***Acta Materialia*** *103*, 633-642, 2015.

[17] Zihang Liu, Huiyuan Geng, **Jing Shuai**, Zhengyun Wang, Jun Mao, Dezhi Wang, Qing Jie, Wei Cai, Jiehe Sui, and Zhifeng Ren, "The effect of nickel doping on electron and phonon transport in the n-type nanostructured thermoelectric materials CoSbS", ***Journal of Materials Chemistry C*** *3*, 10442-10450, 2015.

[18] Lihong Huang, Yumei Wang, **Jing Shuai**, Hao Zhang, Siqi Yang, Qinyong Zhang and Zhifeng Ren, "Thermal conductivity reduction by isoelectronic elements V and Ta for partical substitution of Nb in half-Heusler $Nb_{(1-x)/2}V_{(1-x)/2}Ta_xCoSb$", ***RSC Advances*** *5*, 102469-102476, 2015.